Volume 16
Number 11
November 2023
Pages 4697–5536

Energy & Environmental Science

rsc.li/ees

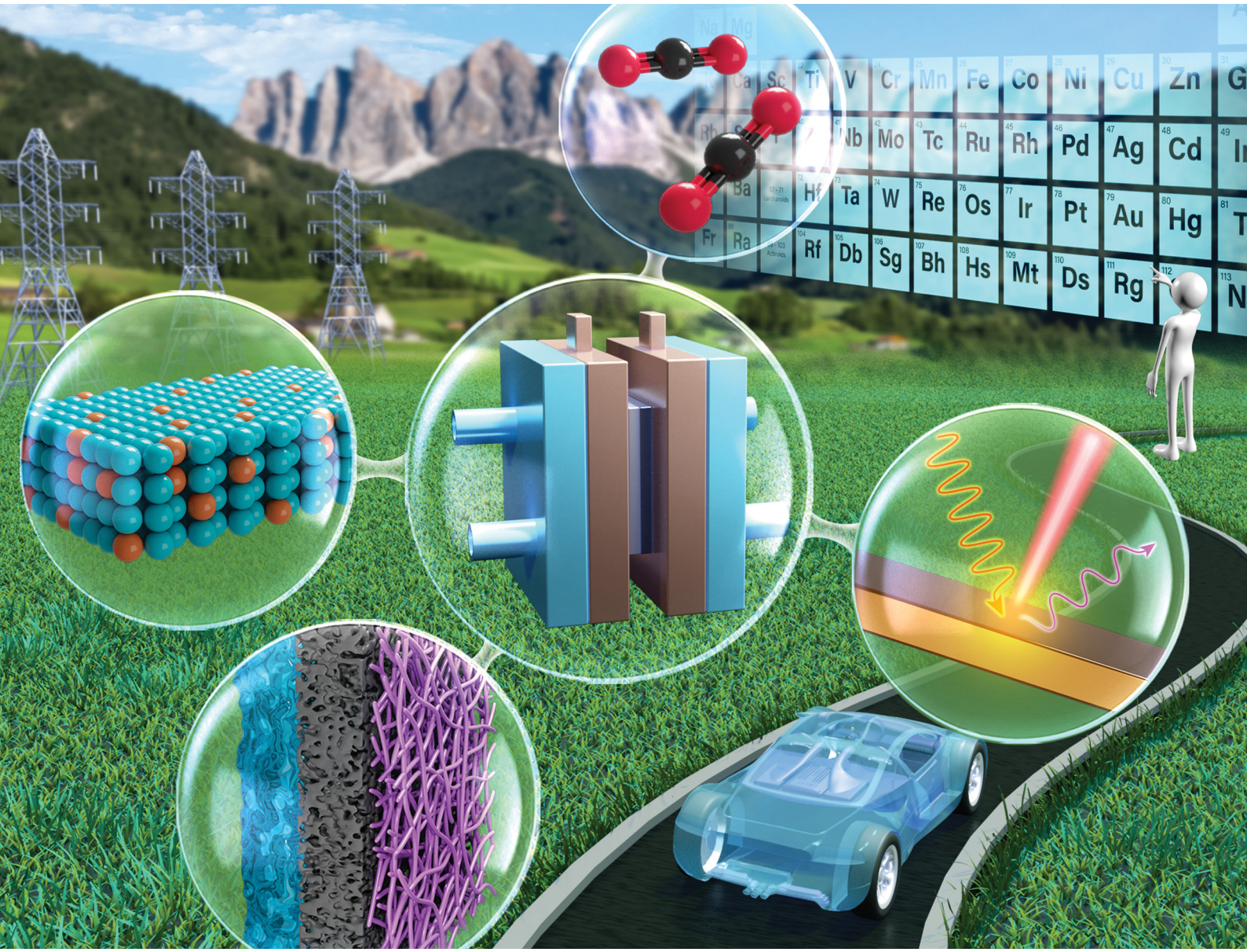

ISSN 1754-5706

ROYAL SOCIETY OF CHEMISTRY

REVIEW ARTICLE

Bin Chang, Huabin Zhang *et al.*

Electrochemical reduction of carbon dioxide to multicarbon (C_{2+}) products: challenges and perspectives

Energy & Environmental Science

ROYAL SOCIETY OF CHEMISTRY

REVIEW

View Article Online
View Journal | View Issue

Cite this: *Energy Environ. Sci.*, 2023, **16**, 4714

Electrochemical reduction of carbon dioxide to multicarbon (C_{2+}) products: challenges and perspectives

Bin Chang,[ab] Hong Pang,[c] Fazal Raziq,[ab] Sibo Wang,[d] Kuo-Wei Huang,[ab] Jinhua Ye *[c] and Huabin Zhang *[ab]

Electrocatalytic CO_2 reduction has been developed as a promising and attractive strategy to achieve carbon neutrality for sustainable chemical production. Among various reduction products, multi-carbon (C_{2+}) compounds with higher energy density are desirable value-added products. Herein, we review and discuss the recent progress and challenges in preparing C_{2+} products. We start with the elaboration of the most recent advancement of carbon–carbon coupling results and the newly proposed mechanisms, which are much more complicated than that of single-carbon products. The complex scenarios involved in the initial CO_2 activation process, the catalyst micro/nanostructure design, and mass transfer conditions optimization have been thoroughly discussed. In addition, we also propose the synergistic realization of high C_{2+} product selectivity through the rational design of the catalyst and elaborate on the influence of electrolytes (anion/cation/pH/ionic liquid) using theoretical calculation analysis and machine learning prediction. Several *in situ*/*operando* techniques have been elaborated for tracking the structural evolution and recording the reaction intermediates during electrocatalysis. Additional insights into the triphasic interfacial reaction systems with improved C_{2+} selectivity are also provided. By presenting these advances and future challenges with potential solutions related to the integral development of electrochemical reduction of carbon dioxide to C_{2+} products, we hope to shed some light on the forthcoming research on electrochemical carbon dioxide recycling.

Received 27th March 2023,
Accepted 16th June 2023

DOI: 10.1039/d3ee00964e

rsc.li/ees

Broader context

The electrochemical CO_2 reduction reaction (CO_2RR) holds promise to revolutionize the chemical industry by producing value-added chemicals and fuels from CO_2 and water while storing renewable energy and reducing anthropogenic CO_2 emissions. However, electrocatalytic C–C coupling in aqueous electrolytes is still challenging due to low selectivity, activity, and stability. The optimization of catalysts, the reaction system including the electrolyte and reactors holds the key to addressing these challenges. We summarize the recent progress in achieving efficient C–C coupling for C_{2+} products, with emphasis on design strategies in electrocatalysts and electrocatalytic reactors, the influence of electrolytes and the theoretical investigations of corresponding mechanisms integrating with *in situ*/*operando* techniques. Moreover, the current challenges and future opportunities for C_{2+} product synthesis are discussed. We aim to provide a detailed review of the novel C–C coupling strategies for further development and inspiration in both fundamental understanding and technological applications of electrochemical carbon dioxide recycling.

1. Introduction

Over the last century, energy has mainly been obtained through the combustion of fossil fuels, in the form of coal, oil, and gas, and the associated CO_2 emissions have significantly increased the atmospheric CO_2 level, resulting in drastic climate change, sea level rise, ocean acidification, and other problems. The concerns over the increase in CO_2 emission and the demand for carbon-containing raw materials have accelerated the development of a variety of technologies for CO_2 reduction conversion.[1–5] The conversion of CO_2 to chemicals and liquid fuels with low-carbon energy sources,

[a] *Chemistry Program, Physical Science and Engineering Division, King Abdullah University of Science and Technology (KAUST), Thuwal 23955-6900, Kingdom of Saudi Arabia. E-mail: huabin.zhang@kaust.edu.sa*
[b] *KAUST Catalysis Center (KCC), King Abdullah University of Science and Technology (KAUST), Thuwal, Kingdom of Saudi Arabia*
[c] *International Center for Materials Nanoarchitectonics (WPI-MANA) National Institute for Materials Science (NIMS)1-1 Namiki, Tsukuba, Ibaraki 305-0044, Japan. E-mail: jinhua.ye@nims.go.jp*
[d] *State Key Laboratory of Photocatalysis on Energy and Environment, College of Chemistry, Fuzhou University, Fuzhou 350002, P. R. China*

particularly multicarbon (C_{2+}) hydrocarbons and oxygenates, has emerged as a fundamental approach to alleviate extreme climate change and the increased energy demand.[6–9] However, CO_2 activation under mild conditions and the precise regulation of C–C coupling are the grand challenges in artificial carbon fixation and C_{2+} product synthesis. Electrocatalytic CO_2 reduction reaction (eCO_2RR) is considered a promising strategy from the perspectives of technical difficulty, maturity, and economy, and thus has attracted extensive research attention from both academia and industry.[10–12]

The electrochemical reduction of carbon dioxide to highly selective C_{2+} products is the holy grail of electrochemical synthesis. Compared to C_1 products (*e.g.*, carbon monoxide, methane, formic acid, and methanol), C_{2+} products (*e.g.*, ethylene, ethanol, acetic acid, and *n*-propanol) possess higher energy densities and economic value and can be further utilized as feedstocks for the synthesis of long-chain hydrocarbon fuels.[13–17] Currently, *CO dimerization and *CO hydrogenation are believed to be the main C–C coupling pathways to realize the evolution of C_{2+} products, while the rate-determining steps of C_{2+} product synthesis can be attributed to the initial activation of CO_2 molecules.[18] Optimizing the *CO binding strength and the subsequent proton transfer-based formation of hydrogenated groups (*e.g.*, *CHO, *COH, *OCCO, and *OCCOH) are pretty sensitive to the material structure and electrolyte composition. Focusing on the synthesis of the C_{2+} products, this review elaborates on the recent progress in eCO_2RR and discusses the present challenges in promoting selectivity and efficiency (Fig. 1). Notably, we have summarized the fundamental principles for novel catalyst discovery and provided a comprehensive overview of the catalytic mechanisms, encompassing nearly all aspects for designing catalysts for C_{2+} synthesis. Various theoretical approaches and models for simulating the complicated C_{2+} synthesis process are systematically summarized. Moreover, we provide several strategies to construct more realistic models for theoretical simulation by considering the electrode–electrolyte interface, charge transfer, solvent effect, and kinetic factors. In addition, *in situ*/*operando* characterization-based research has been emphasized to clarify the structural evolution and the mutual interactions within the reaction interface. Meanwhile, we also summarize the current representative optimization strategies of electrolytes and electrolytic cells for the C_{2+} product system. Based on the triphasic interfacial reaction model, the corresponding design strategy has been put forward to overcome the diffusion and mass transfer limitations of traditional two-phase systems, thus improving eCO_2RR efficiency at industrial current densities. It is highly expected that this review will deliver some new insights toward the understanding and engineering of eCO_2RR and further accelerate the development of this important emerging research field.

1.1. History and reality of electrochemical CO_2 reduction

The first examples of electrochemical reduction of carbon dioxide are from the 19th century when carbon dioxide was

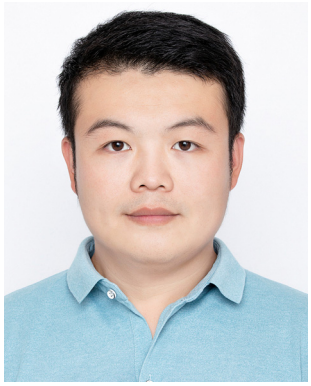

Bin Chang

Bin Chang received his PhD degree from Shandong University in 2020. Then, he worked as a postdoc under the supervision of Prof. Weijia Zhou at the University of Jinan (UJN) and Prof. Shuhui Sun at the Institut National de la Recherche Scientifique (INRS). He is currently a Postdoctoral Fellow in Huabin Zhang's group at KAUST Catalysis Center, King Abdullah University of Science and Technology (KAUST). His research interests focus on advanced catalysts for electrochemical energy conversion.

Jinhua Ye

Jinhua Ye received her PhD from the University of Tokyo in 1990. She is presently a Principal Investigator at the National Institute of Materials Science (NIMS) and a Professor of the Joint Doctoral Program at Hokkaido University, Japan. Her research interests focus on the research and development of photofunctional materials and their applications in the fields of environmental remediation and new energy production. She has published more than 600 high impact research papers with over 60 000 total citations (h index: 133). She is currently serving as the Associate Editor of RSC Catalysis Science & Technology, and Science Advances.

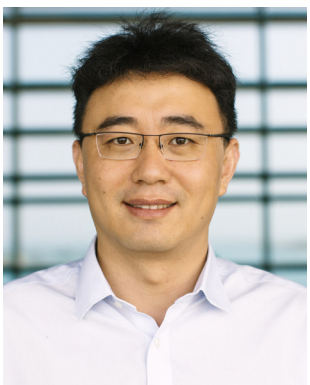

Huabin Zhang

Huabin Zhang received his PhD degree in chemistry from Fujian Institute of Research on the Structure of Matter, Chinese Academy of Sciences (FJIRSM-CAS). After finishing his postdoc research in Japan (Supervisor: Jinhua Ye) at the National Institute of Materials Science (NIMS) and Singapore (supervisor: Xiong Wen Lou) at Nanyang Technological University, Singapore, he joined KAUST serving as an Assistant Professor in January 2021. His research interests focus on advanced catalysis for sustainable energy.

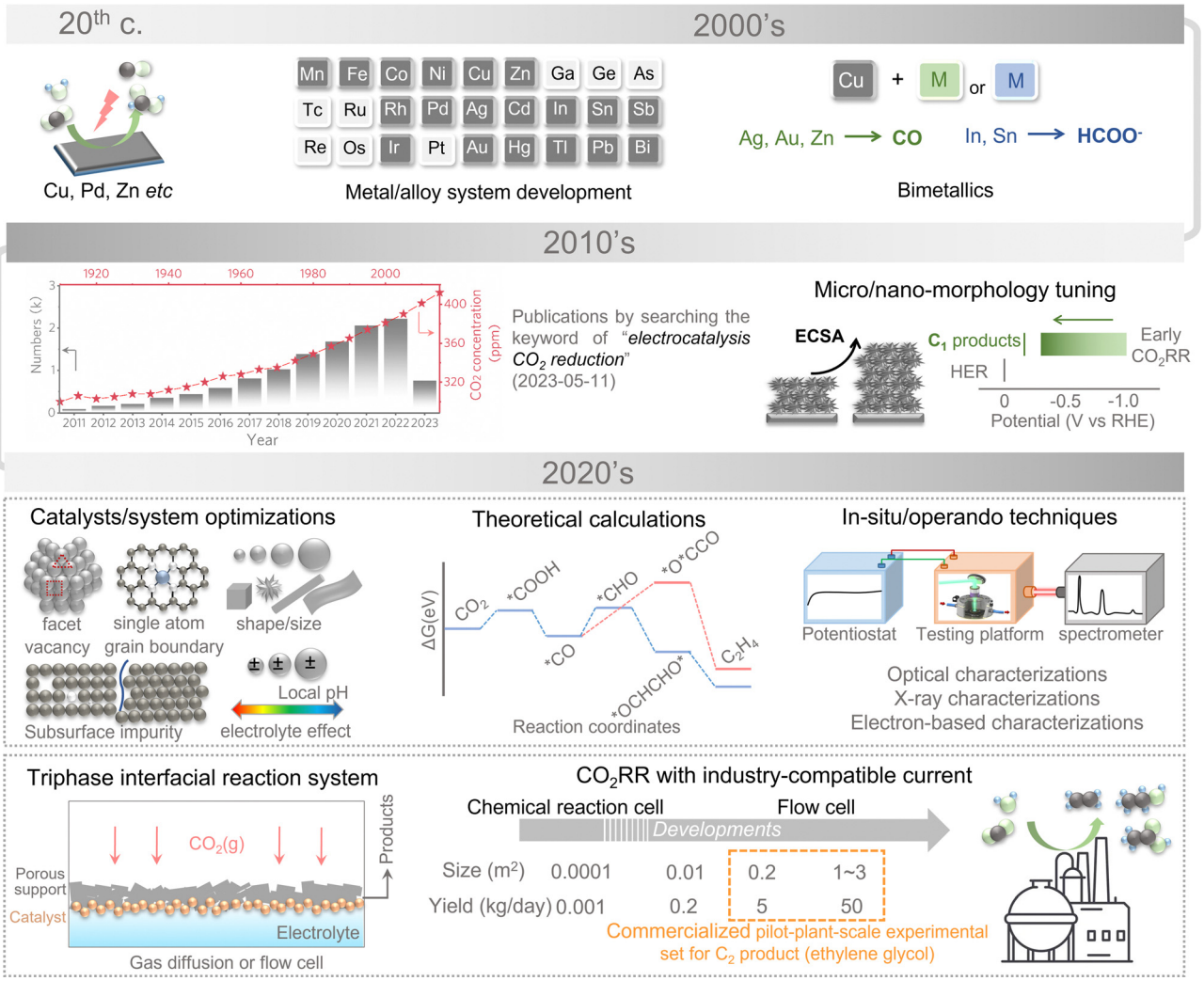

Fig. 1 Recent development of electrochemical CO_2 reduction.

reduced to carbon monoxide using a zinc cathode. Research in this field has been intensified in the 1980s following the oil embargoes of the 1970s, in which the electrocatalytic conversion of CO_2 has been realized over copper, zinc, and lead electrodes with the main product being formate. Methanol has been further synthesized by resorting to ruthenium- and molybdenum-based catalysts and certain semiconductors, such as *p*-GaP and *n*-/*p*-GaAs.[19–22] After entering the first decade of the 21st century, various metal/alloy systems have been developed to be capable of electrochemically reducing CO_2 into hydrocarbons with decent efficiencies stimulating the explosive growth of subsequent studies on metallic electrodes with tuned micro/nano-morphology for eCO_2RR. During this period, most of the research works focused on improving the product selectivity and efficiency of C_1 products. Based on past experimental and theoretical studies, C_{2+} synthesis by CO_2 electrolysis has become the focus of future research in recent years (the 2020s). In the first two years of the 2020s, the C_{2+} product conversion efficiency and selectivity have been greatly enhanced. The mechanisms are gradually revealed by optimized electrocatalysts, sophisticated theoretical considerations, novel reaction devices, and advanced *in situ*/*operando* characterization techniques.[23–29]

eCO_2RR exhibits very slow thermodynamic kinetics owing to the net zero dipole moment and the highly chemically inert linear CO_2 molecule with short polar C=O bonds (0.116 nm). The first step of eCO_2RR is always believed to be CO_2 activation, corresponding to the reduction of chemical bonds.[30,31] The C–C coupling can be realized over the varied pathways, resulting in the emergence of the competing reaction and relatively low selectivity for particular products. Of course, the hydrogen evolution reaction (HER) may be accomplished and even be evolved into the primary reaction simultaneously, especially at high negative potentials, which bring additional barriers to promoting its selectivity for C_{2+} products. In such a scenario, realizing the efficient electrochemical reduction of CO_2 into specific C_{2+} products with high selectivity is challenging.

It should also be noted that C_{2+} selectivity and activity are highly sensitive to multiple electron transfers during C_{2+} product formation. Unlike C_1 synthesis, the *CO intermediate is

considered the starting point for further C–C coupling. The subsequent complex reaction pathway and HER competition directly lead to the low Faraday efficiency (FE) of C_{2+} product formation.[32,33] Presently, the FE of C_{2+} product formation can exceed 60%.[34–36] However, the poor selectivity limits the synthesis and subsequent applications of C_{2+} products. Zheng and colleagues have designed defect-site-rich nanocatalysts with peak FE values of ethanol and *n*-propanol at 53% and 18%, respectively.[37] The control sample with flat surfaces formed without *CO adsorbates produced C_2H_4 with a maximum FE of 60% at −1.23 V (*vs.* RHE), whereas the FEs of other C_1 and C_{2+} products range from 5% to 15%. A similar phenomenon occurs in the gas-diffusion-electrode-based flow-cell system. The overall current densities of defect-site-rich nanocatalysts reached ~200 mA cm^{-2} with the highest FE values of 52% and 15% for ethanol and *n*-propanol at −0.95 V (*vs.* RHE). Herein, the design of nanocatalyst structures and reaction systems is subject to stringent requirements, and C–C bond formation is still a fundamental chemical challenge for further C_{2+} synthesis.

1.2. Mechanism of C_{2+} product formation

1.2.1. Thermodynamics of C_{2+} products. The raw and derived thermochemical data and calculated equilibrium potentials of C_{2+} product formation *via* eCO_2RR are provided in Table 1.[38] The critical parameters for calculating chemical equilibria are the free energy of formation of the reactants and products ($\Delta_f G^\circ$). The free energy formation is related to the standard formation enthalpy ($\Delta_f H^\circ$) and the standard formation entropy ($\Delta_f S^\circ$) according to

$$\Delta_f G^\circ = \Delta_f H^\circ - T^\circ \Delta_f S^\circ$$

where T = 298.15 K is the standard thermodynamic temperature. The standard formation entropy is not tabulated but can be calculated from the tabulated absolute standard entropies (S°) according to

$$\Delta_f S^\circ = \sum v_i S_i^\circ$$

where i is the stoichiometric coefficient for species in the formation reactions, and the theoretical reactions form the compound from the constituent elements in the standard states. Liquid CO_2 reduction products are also considered. The most reliable approach for obtaining the free energy of formation for aqueous products is tuning the solvation-free energy of the gas products ($\Delta_{g\to aq}G^\circ$), which is related to Henry's law constant (K_H) by

$$\Delta_{g\to aq}G^\circ = RT^\circ \ln(K_H)$$

Note that Henry's law constant in this equation must be dimensionless. The normal state of gas and solvated compounds is 1 bar and 1 M, respectively.

In general, the electrochemical reduction of CO_2 is described by the equation

$$x\mathrm{CO_2} + n\mathrm{H^+} + ne^- \rightarrow \text{products} + y\mathrm{H_2O}$$

The free energy change of eCO_2RR with CO_2, H_2O, and different products in the standard states is

$$\Delta_{\mathrm{CO_2R}}G^\circ = \sum v_i\left(\Delta_f G_i^\circ\right) = \Delta_f G^\circ_{\text{product}} + y\Delta_f G^\circ_{\mathrm{H_2O}} - x\Delta_f G^\circ_{\mathrm{CO_2}} - n\Delta_f G_{(\mathrm{H^+ + e^-})}$$

The free energy formation of a proton–electron pair is

$$\Delta_f G_{(\mathrm{H^+ + e^-})} = -FU_{\mathrm{RHE}}$$

where F is Faraday's constant and U_{RHE} is the potential *versus* RHE. At the standard equilibrium potential, $U_{RHE} = U^\circ_{CO_2R}$, and the free energy ($\Delta_{CO_2R}G^\circ$) is zero. Herein, U_{CO_2R} can be solved by

$$U^\circ_{\mathrm{CO_2R}} = \frac{1}{nF}\left(x\Delta_f G^\circ_{\mathrm{CO_2}} - \Delta_f G^\circ_{\text{product}} - y\Delta_f G^\circ_{\mathrm{H_2O}}\right)$$

All standard equilibrium potentials are calculated from the free energy formation of the reactants and products. As detailed in Table 1, except the equilibrium potentials of solid oxalic acid which are negative (−0.47 V *vs.* RHE), all other equilibrium potentials of gas or liquid products range from 0.06 V to 0.11 V *vs.* RHE. Regardless of the type of C_{2+} products formed at the cathode, the electron and proton stoichiometry coefficients of the eCO_2RR and the oxygen evolution reaction (OER) must be equal in a continuous eCO_2RR system. Theoretically, the difference between the equilibrium potentials of eCO_2RR and OER, which is the

Table 1 Thermochemistry data for C_{2+} products

Reaction	C_{2+} products		E° (V *vs.* RHE)	$\Delta_f G^\circ$ (kJ mol^{-1})	$\Delta_f H^\circ$ (kJ mol^{-1})	$\Delta_f S^\circ$ (kJ mol^{-1})	K_H (bar M^{-1})
$2CO_2 + 2H^+ + 2e^- \rightarrow (COOH)_2$ (s)	Oxalic acid	s	−0.47	−698.9[a]	−829[c]	116[c]	—
$2CO_2 + 8H^+ + 8e^- \rightarrow CH_3COOH$ (aq) + $2H_2O$	Acetic acid	g	0.11	−374.9[a]	−433[c]	282.8[c]	—
		aq		−396.3[a]	—	—	1.8210–4[c]
$2CO_2 + 10H^+ + 10e^- \rightarrow CH_3CHO$ (aq) + $3H_2O$	Acetaldehyde	g	0.06	−133.0[b]	−166.1[b]	263.8[b]	—
		aq		−139.7[a]	—	—	6.6710–2[c]
$2CO_2 + 12H^+ + 12e^- \rightarrow C_2H_5OH$ (aq) + $3H_2O$	Ethanol	g	0.09	−167.9[b]	−234.8[b]	281.6[b]	—
		aq		−181.3[a]	—	—	4.5510–3[c]
$2CO_2 + 12H^+ + 12e^- \rightarrow C_2H_4$ (g) + $4H_2O$	Ethylene	g	0.08	68.3[a]	52.4[c]	219.3[c]	—
$3CO_2 + 16H^+ + 16e^- \rightarrow C_2H_5CHO$ (aq) + $5H_2O$	Propionaldehyde	g	0.09	−127.0[a]	−188.7[c]	−304.4[c]	—
		aq		−133.3[a]	—	—	7.6910–2[c]
$3CO_2 + 18H^+ + 18e^- \rightarrow C_3H_7CHO$ (aq) + $5H_2O$	1-Propanol	g	0.10	−160.7[a]	−256[c]	322.5[c]	
		aq		−173.0	—	—	7.1410–3[c]

[a] Calculated data from *Chem. Rev.*, 2019, **119**, 7610. [b] John A. Dean, *Langes Handbook of Chemistry*, 15th edn, McGraw-Hill Inc, 1999. [c] NIST Chemistry Webbook, https://webbook.nist.gov/chemistry/.

minimum potential for driving the entire reaction, is above 1 V.[39] The thermodynamics of eCO_2RR pathways is affected by the different chemical potentials of electrons. The surface structure of electrocatalysts influences the reaction kinetics at low current densities or overpotentials. Meanwhile, mass transfer plays a significant role at high overpotentials or current densities.[40] Beyond the above limit, further increased overpotential enhances HER side reactions and decreases the selectivity of C_{2+} synthesis. Therefore, eCO_2RR currently requires a relatively large overpotential exceeding the thermodynamic potential. It is also urgent to achieve higher current densities and overpotentials for eCO_2RR.

1.2.2. Mechanisms of C_{2+} product formation. C–C coupling imposes stringent requirements on the affinity of the catalyst for *CO. However, overly strong interactions between *CO and metal electrocatalysts result in the poisoning of eCO_2RR active sites and the dominance of the competitive HER. Excessively weak interactions favor *CO desorption (which ensures the formation of C_1 products) over further C–C coupling (which provides the construction of C_{2+} products). Numerous experimental and theoretical studies have revealed that the surface reaction involves initial CO_2 activation and *CO intermediate adsorption through *COOH for further C_{2+} synthesis.[41] The deep understanding and rational tuning of C–C coupling are essential for preparing advanced electrocatalysts with elevated C_{2+} activity and selectivity. To date, three main mechanisms have been proposed for C–C coupling in the direct eCO_2RR to obtain C_{2+} products.

Recently, the *CO dimerization mechanism has been well accepted by the catalytic community, in which the production of OC*–*CO is followed by subsequent hydrogenation reaction (Fig. 2, purple line highlighted pathway).[11,15,16,42,43] Theoretical simulations of *CO dimerization on several copper facets have confirmed the lowest energy barrier on the (100) facet.[44] *CO dimerization is exothermic on the Cu(100) facet but endothermic on the Cu(111) facet. The energy barrier of subsequent hydrogenation on the Cu(100) facet is 0.3–0.4 eV lower than that on the control Cu(111) facet. In addition, *OC–CO is adsorbed on the quadruple site of the Cu(100) facet *via* two carbon ends and is more strongly bound than in the case of the Cu(111) facet, where the carbon atoms are confined to a triple site. *In situ* spectroscopy has detected the characteristic absorption bands of *OC–CO species.[45,46] The possibility of subsequent hydrogen assisted C–C coupling increases at a more negative potential.[47] This mechanism involves the formation of *CHO *via* hydrogenation and its subsequent reaction with *CO to form *COCHO. Bell and colleagues have confirmed the presence of *CHO species on the fluoro-modified catalyst by *in situ* spectroscopy.[48] The fluorine in the modified catalyst enhanced the hydrogenation of *CO to CHO intermediates, which are efficiently coupled to obtain *COCHO and thus improve the selectivity of C_{2-4} products. $*HOCHCH_2$ derived from the hydrogenation of *COCHO is also a critical intermediate, which can directly desorb from the reactive centers to generate acetaldehyde and further converted to ethanol under hydrogenation. Qiao and colleagues have reported a novel silver-modified copper oxide catalyst with a significant FE of

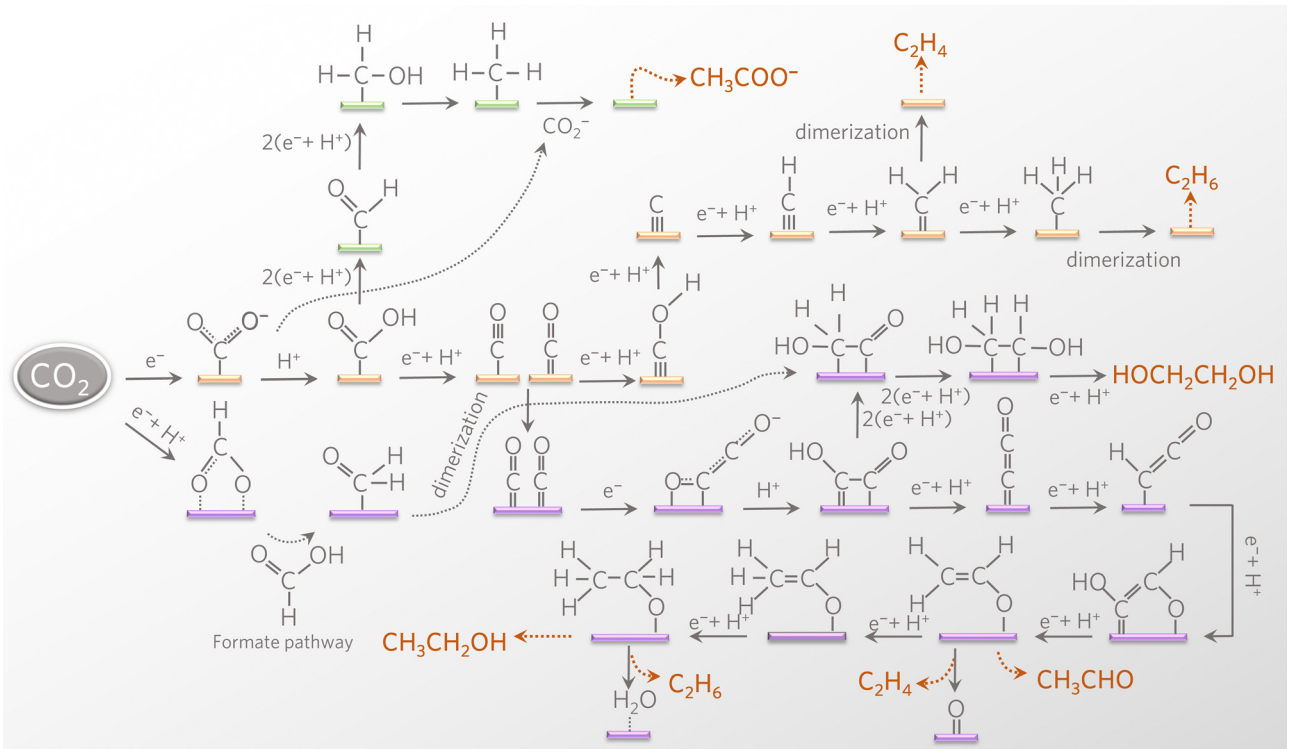

Fig. 2 Overview of reaction pathways for eCO_2RR towards different C_{2+} products.

40.8% for ethanol production.[49] Both top and bridge configurations of *CO adsorption on the catalyst surface trigger asymmetric C–C coupling to ethanol intermediates *$HOCHCH_2$. In addition to the above hydrogenation path, *$HOCHCH_2$ dehydration is another kinetically more favorable path to forming acetaldehyde under neutral conditions. Sun and colleagues have developed ferromagnetic hexagonal-close-packed (hcp) Co nanosheets for selective CO_2RR to acetaldehyde with an FE of 60% in 0.5 M $KHCO_3$ solution.[50] On the hcp Co surface, the C_2 pathway toward acetaldehyde shows a lower overall energy barrier than other competitive pathways to form C_2H_4, CH_3OH, and CH_3CH_2OH. The above reactions follow the path of *CO–CO coupling before hydrogenation/dehydration. Another C–C coupling path is based on the coupling of hydrocarbon groups. Dismukes and colleagues have introduced iron phosphide for the C_2 product (ethylene glycol) synthesis by (H_2CO)* coupling.[51] In this reaction system, formate is more likely to undergo protonation to form the (O–CHO)* intermediate rather than desorb to produce C_1 formic acid. Moreover, hydride transfer to the carbon of (O–CHO)* and the resulting *H_2CO–OH_2 release a water molecule to form (H_2CO)*, which easily undergoes carbon–carbon coupling to form C_{2+} products.

Carbene (CH_2) dimerization (yellow line highlighted pathway) and *CO dimerization under hydrogenation (purple line highlighted pathway) are the two main mechanisms for ethylene synthesis (Fig. 2).[5,6,52] The adsorbed *CO is hydrogenated to form *COH intermediates, which further produce *C and *CH_2 carbene intermediates.[53] Ethylene (or ethane) is generated from *CH_2 (or *CH_3) dimerization under acidic conditions.[54,55] Buonsanti and colleagues have confirmed the carbene coupling mechanism of ethylene synthesis *via* the tunable tandem catalysts comprising iron porphyrin and Cu nanocubes.[56] Furthermore, another procedure for ethylene synthesis is *CO/CO dimerization and hydrogenation. Jaramillo and colleagues have directly converted vapor-fed CO_2 to ethylene on a tandem electrocatalyst.[57] The enhancements of ethylene yield are attributed to the increased *CO/CO concentration near the copper surface *via* effective CO_2 to CO conversion on neighboring nickel-coordinated nitrogen-doped carbon, in which the as-produced *CO–CO intermediate is further hydrogenated to ethylene.

Theoretically, it is also feasible to synthesize acetate with the coexistence of *CO intermediates and hydrocarbon intermediates. However, the acetate selectivity on traditional inorganic catalysts is generally limited by the competitive reaction of ethylene and ethanol. Schöfberger and colleagues have developed a molecular Mn^{III}-corrole complex with an acetate selectivity of 63%.[58] Such a high acetate selectivity originates from the Lewis acidity of the Mn^{III} center, which tends to bind with the Lewis basic O-site of the carboxyl group, hence facilitating the C–C dimerization leading to an oxalate-type intermediate. To significantly increase the coverage of carboxyl intermediates, Liao and colleagues have developed a stable and conductive phthalocyanine-based covalent-organic framework (COF) for acetate synthesis with an FE of 90.3%.[59] The isolated copper-phthalocyanine active sites with elevated electron density are conducive to the critical C–C coupling step of *CH_3 with carboxyl intermediates to produce acetate (Fig. 2, green line highlighted pathway). Herein, the construction of molecular catalysts sheds light on the rational design of highly efficient electrocatalysts for highly valuable C_{2+} products.

2. Electrocatalyst design for C_{2+} product synthesis

The structure and composition of the catalyst play a decisive role in determining the substrate activation and reduction process and thus significantly influence the final product selectivity. The desired high-value C_{2+} products can be obtained by optimizing the surface electronic structure and the geometric environment by regulating the morphology, surface structure, supports, and active sites (Fig. 3).[11,60,61]

2.1. Single-atom catalyst design

Single-atom electrocatalysts are widely investigated owing to the merits of efficient atomic utilization and excellent activity.[62–65] The type of central metal species, electron configuration, and the surrounding coordination environment affect their geometric and electronic structure for tuning the reaction pathways and product distribution of eCO_2RR.[66–68] Appropriate central metal atoms with low Gibbs free energy of eCO_2RR are selected to enhance the electrocatalytic performance, which include Fe, Co, Ni, Cu, Zn, Sn, and Sb. Xu and colleagues have prepared a copper single-atom catalyst anchored on a carbon support by a copper-lithium hybrid method. The as-synthesized catalyst has achieved a single-product FE of 91% at −0.7 V *vs.* RHE and an onset potential as low as −0.4 V *vs.* RHE for electrocatalytic CO_2-to-ethanol conversion.[41] The FE of ethanol formation is highly sensitive to the dispersion of copper atoms. The dynamic reversible conversion between copper single atoms and nanoparticles/clusters has been observed using *operando* X-ray absorption spectroscopy (XAS), which promotes an understanding of real catalytically active sites. Similarly, single-atom electrocatalysts have attracted tremendous attention.[69] Chen and colleagues have achieved CO_2 reduction on single-atom copper with acetic acid, ethanol, and acetone production at low overpotential (Fig. 4A).[70] Adjusting the cooperative structure of single copper atoms and exploring reversible reconstruction under negative reduction voltages is a promising research direction to achieve effective C_{2+} formation.

Currently, specific coordination configurations can be induced by representative strategies of single-atom alloys and tandem catalysts. The doped atoms in single-atom alloys are diluted to avoid bond formation between neighboring atoms, which appropriately tunes the surface structure to achieve moderate binding with the reaction intermediates. The introduction of the atom with low binding energy to CO may provide enough free CO molecules for further C_{2+} synthesis. Grätzel and colleagues have prepared CuZn single-atom alloys for eCO_2RR with 41% FE for C_{2+} liquids.[71] Based on the strong CO adsorption on Cu sites, the incorporated heteroatom Zn enhances the CO production and favors the release of free CO molecules to

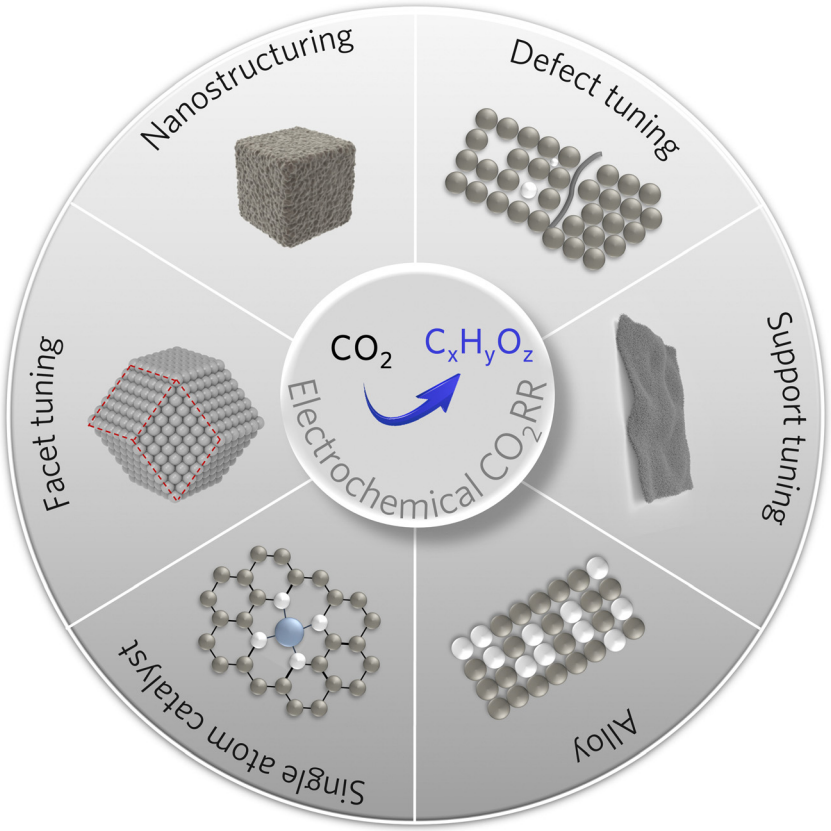

Fig. 3 Scheme of various strategies for designing copper-based electrocatalysts for C_{2+} products.

Cu sites. The as-formed *CH_3 intermediates with the free CO further form C_2H_5OH with high selectivity. Furthermore, the tandem catalysts also significantly expand the applications of single-atom electrocatalysts in multi-electron eCO_2RR.

Strasser and colleagues have investigated the mechanistic aspects of the eCO_2RR reactivity of CO_2/CO co-feeds on Cu/Ni single-atom N-doped carbon tandem catalysts.[72] They have confirmed the *CO (from CO_2)–*CO (from CO) cross-coupling pathway, implying the existence of separate CO_2/CO adsorption sites. In this tandem catalyst, the Ni single-atom acts as an efficient CO producer, and CuO_x nanoparticles work for further C–C coupling. The ethylene yield rate of this tandem catalyst is much higher than that of the sole component catalyst. The results verify the efficient tandem system for local CO co-feeding, which can enhance the ethylene yield and provide a basis for subsequent extended research in eCO_2RR. Integration of copper and other adjacent active sites provides the opportunity for efficient C_{2+} synthesis, such as tuning the adjacent active site spacing, single atom loading density, coordination of the electronic environment around single atoms, *etc.* Despite the above research progress, there is still a big gap and challenge in developing single-atom CO_2RR catalysts for further industrial applications.

2.2. Morphology regulation

The particular morphology of nanostructured catalysts and distinct electronic and chemical surface properties usually confer improved eCO_2RR activity and selectivity compared to bulk materials.[73,74] In this sense, the reactivity of nanocatalysts can be rationally tuned by modifying the fundamental parameters: size, shape, surface composition, or loading on the support.[4,5,10,75]

As for the 0D nanoparticles, the direct influence of particle size on catalyst reactivity is mainly related to the significant increase in the ratio of the surface atoms to the volume atoms. With the decrease in the particle size, the surface curvature increases, and the corresponding average coordination number decreases.[76] In addition, owing to the minimal size of nanoparticles, their surface atoms experience significant strain, which changes the d-band position, thus affecting the reactivity of intermediate groups. Copper nanoparticles exhibit a larger effective area for the further reduction of *CO and favor the formation of C_{2+} products. The increased CO coverage on cuboid copper nanoparticles provides more C–C coupling opportunities, enabling C_{2+} selectivity at low overpotential.[77,78] Moreover, the *COOH and *OCHO intermediates also play a decisive role in determining the C_{2+} selectivity. Amal and colleagues have achieved the controllable generation of crystal defects, vacancies, and coordinatively unsaturated metal sites by regulating the voltage of the reduction–reoxidation–reduction pretreatment method. Thus, high formic acid selectivity has been achieved with *COOH as the intermediate on as-synthesized copper nanoparticles.[79,80] The oxidation–reduction/amorphous–recrystallization process has been observed using

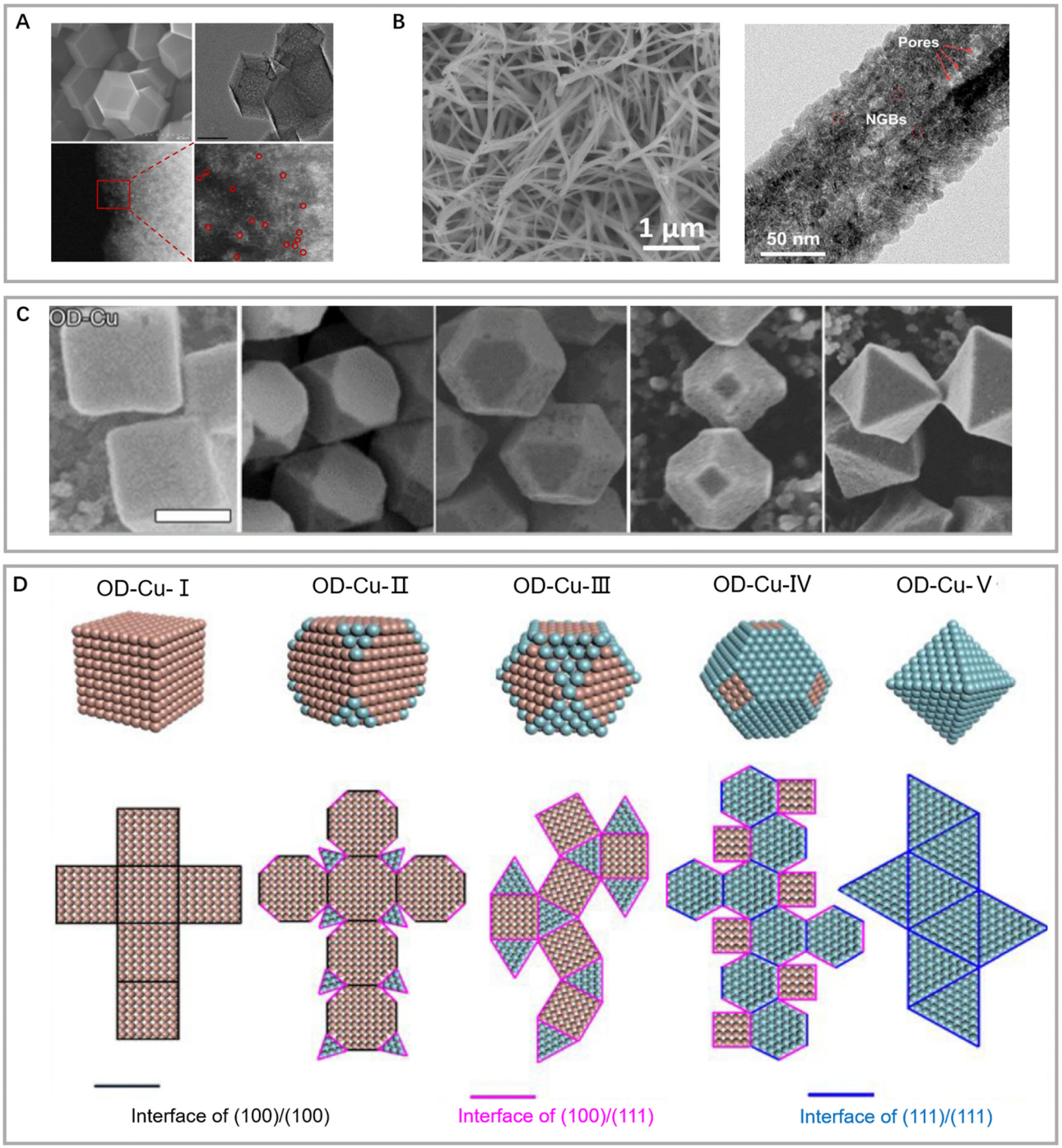

Fig. 4 (A) Morphological characterization of single copper atom electrocatalysts. Reproduced with permission from Chen *et al.*[70] Copyright 2020 Springer Nature. (B) Scanning electron microscopy (SEM) and transmission electron microscopy (TEM) images of CuO micropore nanowires. Reproduced with permission from Yu *et al.*[85] Copyright 2020 American Chemical Society. (C) SEM images and (D) corresponding structure of OD-Cu derived from Cu_2O crystals. Reproduced with permission from Gao *et al.*[82] Copyright 2022 American Chemical Society.

operando XAS, which has revealed dynamic changes in the oxidation state and grain boundary formation during catalyst reconstruction.

Nanostructured materials with various morphologies also present unprecedented catalytic activity, namely, lower onset potentials and enhanced selectivity toward C_{2+} products.[81] Such trends have been assigned to their rough morphology and exposed active facets, as well as to possible changes in the chemical state of the active species. Gao and colleagues have proved that cubic copper nanocrystals with major exposed (100) facets tend to reduce CO_2 to ethylene, whereas octahedral copper nanocrystals with predominantly (111) facets convert

CO_2 into CO and CH_4 (Fig. 4C and D).[82–84] Hexagonal polyhedral copper enhances ethanol synthesis owing to the regulated binding energy of surface-adsorbed *O on numerous edge sites. Furthermore, the catalyst morphology also affects the surface strain, thus influencing the adsorption of key intermediates (Fig. 4B).[85] This relationship has inspired the development of suitable 3D nanostructures to further improve the C_{2+} activity and selectivity by maximizing the number of active sites and controlling proton transfer/reaction pathways.

Hollow nanostructures play a critical role in the eCO_2RR process, exhibiting the following advantages: affluent surface areas, an excellent interface, a strong synergistic effect between different components, and protection of metal active sites. Zhang and colleagues have prepared hollow Cu/CeO_2 nanotubes with a high ethylene FE of 78.3% in the flow cell at a low applied potential of −0.7 V *vs.* RHE.[86] The high reduction efficiency can be attributed to the synergistic effects of the inseparable interface structure between Cu and CeO_2, which promote the effective adsorption of intermediates. Furthermore, Wang and colleagues have chosen hollow mesoporous carbon spheres for protecting copper clusters to achieve high C_{2+} selectivity.[87] The projected active sites promoted eCO_2RR performance with the enhanced formation of *CHO, thus facilitating the C–C bond coupling to form C_2H_4 and C_2H_5OH. We propose that the unique hollow structure plays a significant role in the future development of electrochemical C_{2+} synthesis.

2.3. Surface structure tuning

The engineering of surface defects or surface ligand structure has achieved electronic structure regulation and surface/interface optimization, which provide suitable adsorption sites for reaction intermediates and favorable conditions for further C–C coupling.[88,89] Meanwhile, defect engineering achieves the optimization of catalytic surface activity by precisely tuning the defects, including type, concentration, and spatial distribution.[90] In carbon-based metal-free materials, the defects are divided into intrinsic and externally induced defects. Intrinsic defects can be purposely introduced to enhance CO_2 adsorption by regulating the edge sites, holes, or topological defects. Unlike the intrinsic defects, the defects induced by the covalent bonding of heteroatom doping can break the original sp^2 carbon lattice. Defect configurations (such as pyridine nitrogen, pyrrole nitrogen, heteroatom coordination, *etc.*) can perturb the electron symmetry in the aromatic ring and change the local charge distributions, thus leading to acceleration of the CO_2RR process and suppression of the HER activity.

As a typical defect existing in metal-based catalysts, vacancies can effectively regulate the electronic structure and mass transfer performance of the active sites, thus optimizing the electrochemical reaction kinetics of C–C coupling (Fig. 5). Oxygen vacancies can be easily introduced and controlled in

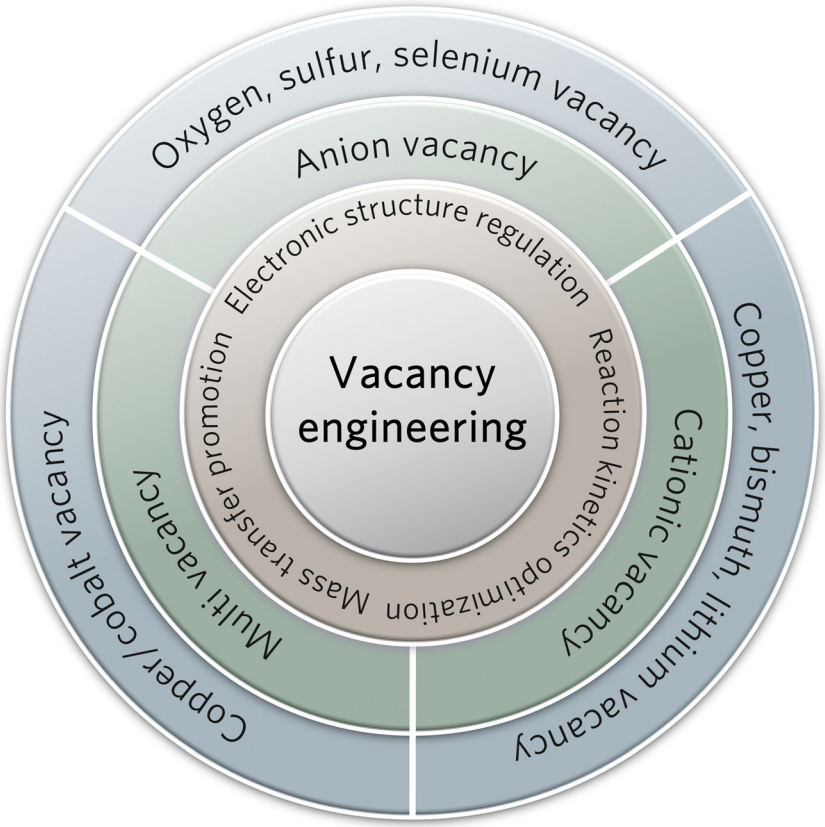

Fig. 5 Scheme of vacancy engineering with properties and classifications.

the form of anionic vacancies. Zheng and colleagues have reported an oxygen vacancy-containing copper-based electrocatalyst with high eCO_2RR activity. The number of oxygen vacancies directly affected the selectivity to ethylene and eCO_2RR current density.[91] The CuO_x catalyst with abundant oxygen vacancies exhibited a high ethylene yield at −1.4 V *vs.* RHE, while the corresponding FE has been confirmed as 63%. As demonstrated by the authors, the ethylene yield is consistent with the change in oxygen vacancies. The oxygen vacancy-rich CuO_x surfaces provide strong binding affinity to the intermediates of *CO and *COH, but weak affinity to $*CH_2$, thus leading to efficient formation of ethylene. Moreover, the positive effects of sulfur and selenium vacancies over metal chalcogenide electrocatalysts for eCO_2RR have also been well investigated and explored.[92–94] In another study by Zheng and colleagues, a copper-based electrocatalyst with disulfide vacancies has been designed and synthesized *via* lithium regulation. Both theoretical calculations and experiments have confirmed that these disulfide vacancies act as catalytically active sites for enhanced performance of *n*-propanol synthesis (Fig. 6A and B).[92] Previous studies have successfully constructed disulfide vacancies. These defects exert synergistic effects *via* negative charge enrichment by the adsorption of three *CO intermediates, the provision of a closer Cu−Cu distance for *CO–*CO coupling, and the provision of suitable space for charge repulsion caused by OCCOCO* formation. The adsorption of *CO cannot be completed without vacancies. Although the dimerization of *CO can be achieved on single sulfur vacancies, further OCCO–CO coupling is not feasible. Lastly, CuS_x containing double sulfur vacancies has demonstrated an FE of 15.4% for

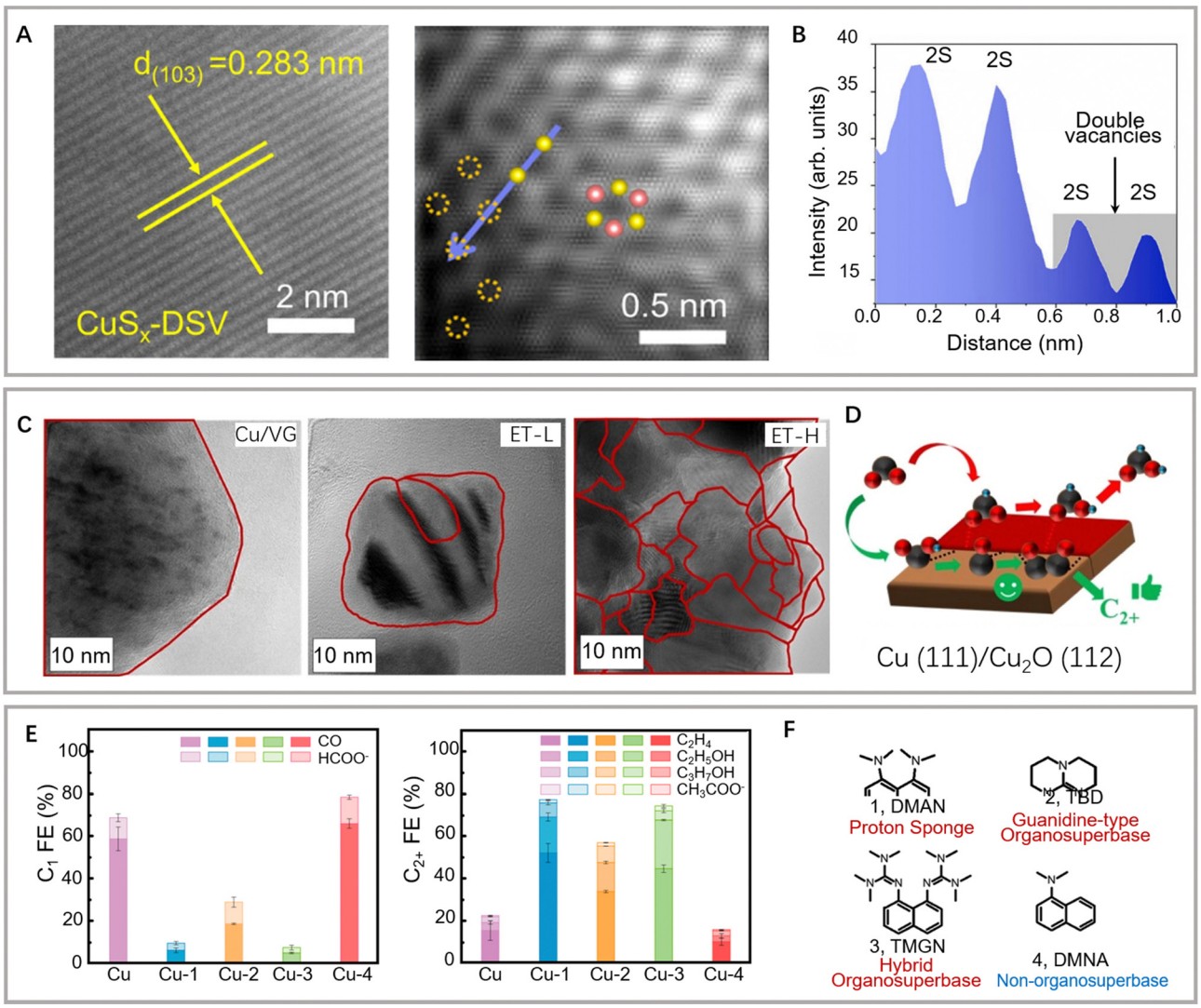

Fig. 6 (A and B) Structural characterization of the double sulfur vacancy-rich CuS_x catalyst. (C) Intensity profiles extracted from the blue line in (B). Reproduced with permission from Zheng *et al.*[92] Copyright 2021 Springer Nature. (C) HR-TEM images of Cu/VG, ET-L, and ET-H (grain boundaries are highlighted in red spline). (D) Schematic of the preferred CO_2RR pathway on the Cu(111)/Cu_2O (112) interface. Reproduced with permission from Rose Amal *et al.*[98] Copyright 2022 American Chemical Society. (E) eCO_2RR performance of C_1 products and C_{2+} products on different catalysts. (F) Different organic/non-organosuperbases. Reproduced with permission from Wang *et al.*[18] Copyright 2022 Elsevier.

forming *n*-propanol. Although tremendous efforts have been made to design anionic vacancies, the C_{2+} selectivity is still unsatisfactory.[95] The design of multi-vacancies or coupling of multiple type vacancies (anionic and cationic vacancies) to optimize the migration pathway of reaction intermediates (*COH, *CHO, *COOH) represents a promising research direction for enhanced performance toward C_{2+} synthesis.

Furthermore, as there is no preferred facet orientation on nanostructured materials, high-density defects, grain boundaries, and surface roughness are considered to determine the final catalytic behavior.[93,96,97] As mentioned previously, the residence time of intermediates is critical for the selectivity of C_{2+} products. Although adsorbed *CO is the crucial intermediate for C_{2+} synthesis, the correlation between the grain boundaries and the low overpotential does not guarantee similar eCO_2RR mechanisms. Rose and colleagues explored a reduction–oxidation–reduction (ROR) electrochemical treatment to advisedly reconstruct copper nanoparticles. Rich grain boundaries were observed, which were attributed to different phases of Cu or Cu_xO (Fig. 6C).[98] In particular, rich grain boundaries formed on the ROR catalyst with Cu(0)/Cu(I) interfaces promoted *COOH/*OCCO adsorption, thus facilitating C–C coupling and leading to *COOH-derived products (Fig. 6D). Most copper-based catalysts inevitably undergo structural reconstruction processes at reaction potentials. The structure and chemical state of the original catalyst (pre-catalyst) may undergo significant changes under the action of the applied potential and reaction intermediates, such as fragmentation, aggregation, and morphology reshaping.[99–101] On the one hand, structural reconstruction may lead to the deactivation of copper-based catalysts. On the other hand, it may also induce the formation of active sites that promote C–C coupling to produce C_{2+} products. The uncertainty brought by this structural reconstruction constrains the development and application of copper-based catalysts. Therefore, it is crucial to design and select pre-catalysts and study their structural evolution under electroreduction conditions. Superparticles have complex assembly structures and undergo unique structural reconstruction processes under electroreduction conditions, which may play a positive role in C_{2+} product synthesis. Xiong and colleagues have explored the assembly structure of Cu_2O superparticles that underwent complex structural evolution during eCO_2RR.[102] The high C_{2+} selectivity has been confirmed by *in situ* spectroscopic tests and electron microscopy characterization. The internal building blocks of these superparticles have produced many grain boundaries, whereas the outer building blocks are separated to form nanostructures. The above structural evolution effectively limits OH^- and induces a high local pH around the active sites. The synergy of these extraordinary structural characteristics and the reaction environment on the catalyst surface provides important favorable factors for promoting C–C coupling. Although lattice strain effects in electrocatalysis have been widely investigated,[103] the exact relationship between grain boundary-related micro strains and the binding energy of reaction intermediates remains unclear.

Generally, surface ligands are considered harmful to catalysis during surface structure optimization as they occupy other active surface sites.[104,105] However, several studies have revealed that surface ligands can help improve the catalytic environment and performance through various mechanisms.[104,105] Ligands can perform functions similar to those of protein structures surrounding the active site of enzymes (*e.g.*, by acting as selective permeation membranes, regulating interface solvation structures, regulating the microenvironment on the electrode surface, and participating in chemical activation and the selection of template active sites).[106,107] Agapie and colleagues have optimized the surface of nanostructured copper to significantly promote C–C coupling and attenuate H_2 and CH_4 generation based on the combination of an organic halide additive and a polycrystalline copper structure.[108] Mechanistic studies have revealed several effects of organic additives, including the formation of a specific cubic nanostructure by copper surface corrosion, the stabilization of nanostructures *via* the formation of protective organic layers, and the promotion of C_{2+} formation. Wang and colleagues have regulated the interfacial microenvironment by modifying the surface of the copper catalyst using a water-insoluble organic super naphthene proton sponge (Fig. 6E and F).[18] The adsorbed *CO intermediate has been stabilized by the locally enhanced electrostatic field and the protonated organic superbase. However, the chemical activation mechanism of the surface ligands is yet to be unified. Further experimental/theoretical works should investigate the interaction between surface functionalized ligands and the key intermediates. Moreover, the dynamic structural evolution analysis over surface strain, surface defects, and surface functional groups provides a new opportunity to realize the precise structure regulation for achieving higher eCO_2RR activity and selectivity.

2.4. Support modification

Typically, supports effectively inhibit the agglomeration of nanomaterials, increase the surface area, and optimize the electrochemical properties. The introduction of appropriate supports can not only be conducive to achieving a high nanocatalyst dispersion but can also change the electronic structure.[109–111] The rational utilization of suitable supports also promotes chemical coupling with the supported catalysts, changes the electronic interface structure, and improves C_{2+} selectivity.

Carbon-based metal-free materials have been widely utilized as carriers for eCO_2RR catalysts due to their high conductivity and stability. Carbon supports with a high specific surface area and porosity can be realized through morphology regulation, providing more catalyst anchor sites and accelerating mass transfer.[112–115] Nanostructured carbon supports with various morphology are commonly used to support active substances and prevent the aggregation of nanostructures during reactions.[116,117] Moreover, the intrinsic physicochemical properties of carbon supports can be regulated using doping and surface functionalization, thus improving the total charge and increasing CO_2 concentration on the electrode surface.[118]

Zhou and colleagues have theoretically investigated the activity and selectivity of metal trimer clusters anchored on N-doped carbon supports to form C_2–C_3 hydrocarbons and alcohols (Fig. 7A).[119] The space-constrained triatomic metal centers have been observed to synchronously immobilize multiple CO_2, thus providing electrons and reaction channels for promoting C–C coupling (Fig. 7B). In addition, the mediated cluster–substrate interactions are known to regulate C_{2+} selectivity. Xu and colleagues have prepared a carbon-supported copper catalyst using the copper–lithium mixed synthesis method and achieved the exclusive formation of ethanol with an FE of 91%.[90]

In summary, the beneficial effect of carbon supports on eCO_2RR activity and selectivity is attributed to the following aspects. Firstly, surface functional groups can affect the surrounding electron density. Secondly, optimizing interactions between catalysts and carbon supports is beneficial for forming various products at different overpotentials. Thirdly, the micropores of carbon supports affect the proton transport and CO_2 concentration on the catalyst surface, thus affecting the eCO_2RR activity. Porous carbon supports optimized by doping, functionalization, or defects have been demonstrated to be ideal substrates for improving the C_{2+} selectivity.

Due to the electrocatalytic stability and conductivity, metal-based inorganic materials have collectively been widely explored with carbon-based materials as supports for eCO_2RR in the past two decades.[120] Compared with carbon, metal-based inorganic materials and metal active sites exert a more significant synergistic effect during eCO_2RR. For example, theoretical studies have confirmed that the active centers of metal oxides adsorb and activate CO_2 at the interface between the metal oxides and metal active centers. Owing to the high affinity of transition metals to reaction intermediates, intermediates can be optimized *via* oxygen binding. Goddard and colleagues have constructed a copper-embedded oxide matrix model.[121] The thermodynamics and kinetics of CO_2 activation and *CO dimerization have been significantly improved by the synergistic interaction between surface Cu_+ and surface Cu^0, thus increasing the selectivity and efficiency of C_{2+} product formation. Moreover, they have identified the crystallinity of metal oxides and the interaction between active substances and supports as crucial factors for improving activity and selectivity.

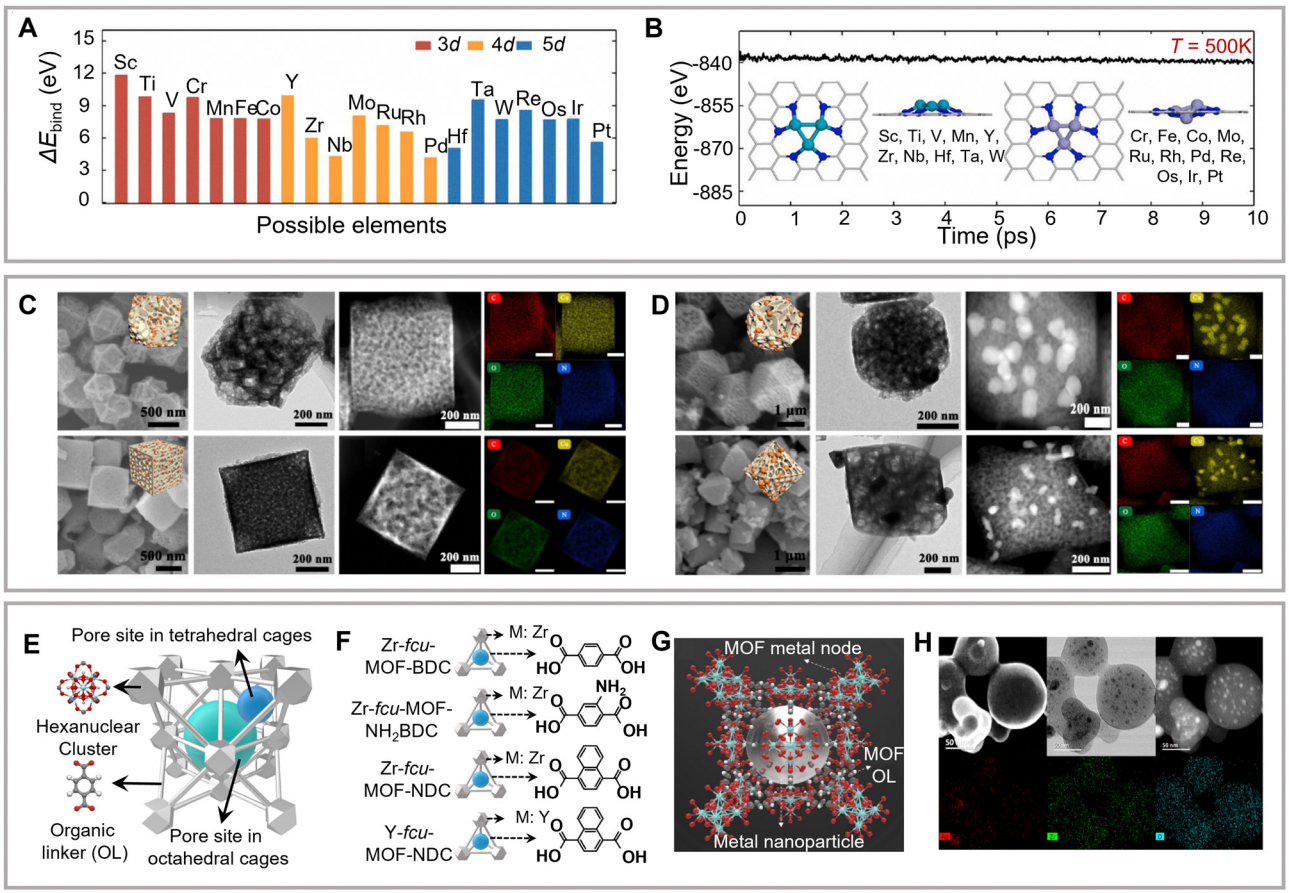

Fig. 7 (A) Binding energies between the metal trimer and carbon supports. (B) The corresponding *ab initio* molecular dynamics (AIMD) simulations and the equilibrium structures. Reproduced with permission from Dou *et al.*[119] Copyright 2020 Elsevier. (C–D) Morphological characterization of shape-tuned MOF support copper catalysts. Reproduced with permission from Cao *et al.*[127] Copyright 2022 Elsevier. (E–G) Schematic of the metal nanoparticle incorporated MOF structure. (H) Morphological characterization of the above MOF structure. Reproduced with permission from Sargent *et al.*[128] Copyright 2020 American Chemical Society.

Suominen and colleagues have successfully achieved efficient CO_2 electroreduction to value-added products on Cu/metal oxide heterostructure.[122,123] Modified metal oxides can stabilize the key intermediates and decrease the Gibbs free energy of the C–C coupling step. To confirm the surface adsorbed intermediates, Wu and colleagues have conducted *in situ* characterization based on Cu/ZrO_2 electrodes with a high FE of 85% for C_{2+} products. Experimental results have confirmed the enhanced adsorption of CO* on the Cu/ZrO_2 electrode, while theoretical calculations reveal the decreased energy barriers of the C–C coupling process at the Cu/ZrO_2 interface. The C–C coupling process is kinetically favored over the Cu/ZrO_2 interfacial boundaries, while the competing C_1 pathway reactions are significantly suppressed. Current studies tend to utilize MXene materials as carriers for tuning surface functional groups or loading active components in electrocatalysis.[124–126] Theoretical calculations have proved that appropriate removal of hydroxyl groups (OH) from MXene-T_x (T = OH, O) can promote surface adsorption capacity for CO_2, making activation of CO_2 on its interfacial sites easier. The stable existence of $CO_2^{\delta-}$, the reduction of the free energy of *CO, *CHO or *COH intermediate formation and the improvement of adsorption stability are more conducive to promoting the C–C coupling process on the above MXene-T_x. Such simple functional group modifications on MXene systems cannot achieve satisfactory C_{2+} product selectivity in practical experiments. Herein, loading CO_2RR active groups (heterojunction, functional group, cluster, single atom, *etc.*) to prepare MXene-based composite catalysts is an effective way to reduce the reaction barrier and promote the C–C coupling reaction in the future.

Metal–organic frameworks (MOFs) and COFs are commonly used as porous supports in heterogeneous molecular complexes. Compared to traditional carbon-based materials, these species provide highly ordered porous networks, which may enhance electrolyte permeability. Meanwhile, organic frameworks with redox-active components as linkages provide a high specific surface area and tunable porosity (Fig. 7C and D).[127,128] MOFs and COFs with optimized structures have been reported to facilitate charge transfer. Chang and colleagues have achieved a breakthrough in the modularized optimization of COF construction using a cobalt porphyrin catalyst organically supported and connected by imine bonds as the construction unit.[129] The eCO_2RR activity of the synthesized catalyst was 26-fold higher than that of the corresponding control compounds. In addition, XAS data further revealed surface environments' influence on the electronic structure of the metal center in the COF catalysts. Subsequently, several studies have confirmed the feasibility of using the metal–organic framework structure as a fixed active center and possible support for efficient eCO_2RR in aqueous solutions.[82,130–132] However, the proposed systems mainly afford the formation of C_1 products. To promote the C_{2+} selectivity, both inorganic substrate (carbon or metal oxide/carbide) and organometallic materials (MOF or COF) should provide well-defined active sites with precise tunability of steric and electronic properties and prevent the active sites from aggregation and demetallation. Moreover, changing the electronic environment of the support around active sites is also effective in promoting CO_2RR selectivity.

2.5. Multi-metal cooperation

The formation of bimetallic alloys is commonly applied to alter eCO_2RR activity and selectivity. The catalytic performance of bimetallic catalysts varies due to their surface composition and structure.[133–136] It is generally assumed that the distinct activity and selectivity of bimetallic alloy catalysts might be attributed to changes in their electronic and geometric structure. The incorporation of a different atom in the lattice modifies the interatomic distance of surface atoms and the lattice strain. The synergy between the two metals can be exploited to regulate the binding (adsorption) strength and configuration of specific intermediates on the catalyst surface, thus promoting C–C coupling and C_{2+} product formation. Theoretical calculations have revealed that the Pd atom promotes *CO desorption by optimizing the electronic structure of the neighboring copper sites. Sargent and colleagues have introduced palladium into copper catalysts to enhance local *CO coverage and C–C coupling.[137] The high affinity of the *CO intermediate enables its competition with H* on active sites. The Pd–Cu bimetallic catalysts achieved high selectivity for C_{2+} products (FE = 89 $\pm$ 4%) by maximizing *CO and CO_2 adsorption to weaken H* binding and inhibit HER.

The atomic order of metal components in bimetallic catalysts is also an essential factor in determining their selectivity. Kenis and colleagues have prepared Cu–Pd bimetallic nanocatalysts with equal atomic ratios but different atomic arrangements and examined their electrocatalytic eCO_2RR performances.[138] Compared to ordered and disordered Cu–Pd particles, the FE for ethylene and ethanol formation is significantly higher, whereas the FE for methane formation is significantly lower. In phase-separated Cu–Pd nanoparticles, adjacent copper atoms promoted *CO dimerization. In the case of alloy nanoparticles, *CO adsorbed on copper atoms may combine with oxygen atoms adsorbed on adjacent palladium atoms to form *CHO, which is further hydrogenated and reduced to methane. The utilization of co-catalysts is another approach for promoting pathways involving *CO by contributing or optimizing *CO formation sites, thus enhancing the production of C_{2+} products. Accordingly, Qiao and colleagues have demonstrated that the redispersion of silver in copper significantly optimizes the coordination environment and oxidation state of copper.[139] The *CO binding strength is changed to form a hybrid adsorption structure, which induces asymmetric C–C coupling and stabilizes the ethanol intermediate to increase ethanol yield. The reactivity and selectivity of bimetallic eCO_2RR catalysts are easily affected by various factors. Herein, the modification of the intra-particle atomic arrangement and spillover effects must be considered in the rational design of advanced catalysts to achieve the effective synthesis of specific C_{2+} products. The multi-metal catalysts should be designed with a donor of the spillover species and a corresponding acceptor of reactive adsorbates (CO_2). The spillover effects promote the *CO intermediate coverage and diffusion at the interface of C_{2+} favored

catalysts (copper) and CO-favored catalysts (Ag, Au). This conclusion has been further confirmed by Jaramillo and colleagues, who decorated gold nanoparticles onto polycrystalline copper foil for efficient alcohol synthesis under alkaline conditions.[140] CO_2 reduction on gold generates a high *CO concentration on nearby copper, where *CO is further coupled to alcohols. The bimetallic electrocatalyst exhibits synergistic activity and selectivity and opens new possibilities for developing CO_2RR electrodes exploiting tandem catalysis mechanisms.

Cu-based catalysts with moderate bonding strength for *CO and *H currently only exhibit satisfactory FE and current density in preparing C_2 products such as ethylene and ethanol. The development of catalysts for long-chain products is still limited, and nickel has shown specific potential among the materials that have already demonstrated certain effects. For example, nickel phosphide exhibits CO_2RR selectivity for C_3 and C_4 hydroxyalkanes (methylglyoxal and 2,3-furandiol) under an extremely low overpotential and current density.[141] However, its stability and selectivity are not satisfactory, which is attributed to nickel susceptibility to CO poisoning and promotion of HER side reactions.[142,143] Yeo and colleagues have reported that catalysts derived from inorganic nickel oxide exhibit unexpected activity and stability for the preparation of multi-carbon products, with a total FE of approximately 30% for carbonaceous products.[144] The FE of C_3 to C_6 hydrocarbon products reached 6.5%, with a partial current density of 0.91 mA cm^{-2}. This excellent activity and stability are attributed to the presence of $Ni^{\delta+}$ with stable Ni–O bonds during the CO_2RR reaction. Unlike Ni^0, $Ni^{\delta+}$ sites have moderate binding energy with CO, which prevents CO poisoning of the catalyst. Meanwhile, the CH/CH_2 insertion mechanism facilitated by $Ni^{\delta+}$ leads to the generation of long-chain hydrocarbons. This mechanism of long-chain hydrocarbon synthesis is different from copper-based catalytic systems, providing more options and possibilities for C_{2+} synthesis.

The strategy for designing highly active catalysts for C_{2+} products should focus on enhancing the activation of CO_2 and stabilizing some key intermediates, in which surface structure engineering plays a crucial role. In this regard, organic molecular functionalization-based surface modification has been achieved by different additives, such as N-containing compounds (amino acids, phenanthroline and the corresponding derivatives), S-containing compounds (alkanethiols) or P-containing compounds.[145–147] All the above-mentioned organic molecules can dramatically change the electronic structure of active metal sites, resulting in the optimization of *CO/*H coverage, hydrogen bond interactions and hydrophobic effects. Another effective approach is heteroatom doping for tailoring the spin state and electronic structure of active sites. For metal-based catalysts, the introduction of electron-withdrawing doping sites enables effective bonding with CO_2 and regulation of surface metal valence states, thereby improving the kinetics process of CO_2 activation and *CO dimerization. For carbon-based metal-free catalysts, the polarization of Lewis basic doping sites can optimize the electronic distribution of adjacent carbon active centers and the bonding ability with reaction intermediates.

Electrochemical CO_2RR activity and selectivity are significantly dependent on the size, exposed active facets and morphology of electrocatalysts. The size of nanoparticles determines the density of low coordination atoms on the surface, which directly affects the binding strength of different reaction intermediates. Reducing the size of nanoparticles is conducive to increasing the number of surface-active sites. However, when the nanoparticle size is reduced to below 15 nm, the binding strength between the catalyst surface and H* gradually becomes stronger, which directly induces a weaker binding strength of reaction intermediates (*e.g.*, *CO, *CHO, *COH).[141] Therefore, the size of nanoparticles and C_{2+} synthesis activity follows a volcano-like relationship, suggesting a recommended nanoparticle size of approximately 25 nm. This can provide enough active sites and atoms with different coordination numbers and chemical interaction energy on the corners, edges, and crystal facets. On this basis, the surface binding energy of adsorbed intermediates can be regulated, thereby optimizing the reaction pathways towards different products and improving the selective synthesis of C_{2+} products. Moreover, considering the different Lewis acidity and polarization abilities of different active facets, optimizing the active facets with the lowest activation barrier and high adsorption energy is beneficial for enhancing CO_2 adsorption and activation. The relationship between the facet structure and reaction pathways can be achieved by regulating the single active facet. Accordingly, control over selectivity can be achieved by maximizing the exposure of potential active facets, such as Cu(100) and high-index facets of other transition metals. To maximize the C_{2+} activity and selectivity on an active crystal facet, ultrathin 2D nanosheets can be prepared as a new form of the CO_2RR catalyst. The surface structure sensitivity of CO_2RR implies the benefits of utilizing nanoparticles with controlled morphologies to investigate the facet effects and fabricate customized materials with optimized key parameters for improving C_{2+} selectivity, such as high-density defects (strain, step edge, and grain boundary) and surface roughness.

3. Computational simulation of the formation of C_{2+} products during eCO_2RR

The development of *ab initio* methods for simulating electrochemical reactions has enabled the investigation of theoretical mechanisms and guided the design of catalysts. Generally, a computational hydrogen electrode model has been used to probe the thermodynamics of electrochemical CO_2 reactions.[148,149] When a proton/electron is transferred to the *CO intermediate to construct the *CHO intermediate, the free energy change is calculated as

$$\Delta G = \mu(\mathrm{CHO}^*) - \mu(\mathrm{CO}^*) - [1/2\mu(\mathrm{H_2}) - eU] + \Delta G_{\mathrm{solv}} + \Delta G_{\mathrm{field}}$$

The potential of the reaction step to release energy corresponds to the thermodynamic limit potential (U_L), which can be used as a critical indicator and a necessary but insufficient criterion

of activity. In a vacuum, the surface hydrogenation barriers for adsorbed *H can be easily determined, but the estimation of electrochemical barriers is more challenging. Ion and solvent effects are also important factors that influence the activity and selectivity of eCO_2RR.[150,151] Presently, theoretical studies on electrochemical activation energy and the corresponding kinetic models and selectivity analyses have demonstrated the influence of potential, solvent, and ions on the catalytic reaction. However, although theoretical calculations enable the *in situ* studies of reactions at the atomic/electron scale, their ability to reproduce actual working conditions is quite limited, such as the complex reaction path, activation energy, and ion effect.

3.1. Mechanism prediction

Among all metal cathode catalysts, copper exhibits high selectivity for hydrocarbons. The theoretical mechanism for forming C_{2+} products on copper is one of the most thoroughly investigated topics in the eCO_2RR field. Recently developed theoretical research models for eCO_2RR mainly include the implicit solvent model, explicit solvent model, and H-shuttling model.[152] These physical models enable the calculation of the pathways of surface eCO_2RR. The obtained surface physicochemical properties (such as the electrode–electrolyte interface structure, adsorption energy of active groups, the position of the band edge, heterogeneous reduction potential, and acidity/hydrogenation of chemical substances in solution or adsorbed on the surface) lay the foundation for the further understanding of reaction mechanisms and reaction rate estimation (Fig. 8A and B).[153]

3.1.1. Theoretical basis of models. In general, CO_2RR energetics can be theoretically described by implicit solvent models, explicit solvent models, and H-shuttling models.[154] The implicit solvent models include a continuum description of the ions. Water and ions are automatically considered in explicit solvent models. The water molecule shuttles protons from the surface and back for the H-shuttling approach. Compared with vacuum metal calculations, introducing solvent molecules and ions increases extra degrees of freedom, which is used to determine the activation barrier. The implicit solvent model assumes a continuous electrolyte medium and enables the successive change in the interface charge, thus enabling the easy realization of real-time potential tuning. This model utilizes the simple linearized Poisson–Boltzmann distribution of ions, which neglects the influence of finite ion size and induces the unphysical interface capacitance in the classical model. The zero-charge potential, the benchmark of the above methods, is related to the metal work function.[155] The consistency between experimental and theoretical zero-charge potentials reflects the generalized gradient approximation function in determining the metal work function. One of the fundamental challenges of the implicit solvent model is the adiabatic shift of ions following the dipole during the reaction. However, these two events occur at very different time scales.[156,157]

Compared to the implicit model, the explicit solvent model is used to investigate electrolyte effects at the atomic level. As ions are explicitly modeled in a finite unit cell, the potentials are not variable. In addition, the simulated proton–electron transfer process induces significant changes in the pathway potential. The generalized gradient approximation level functionals predict the poor band alignment of the solvent's highest occupied molecular orbital (HOMO) and lowest unoccupied molecular orbital (LUMO) and the metal's Fermi energy levels, which induces artificial charge transfer across the interface and the corresponding effects on the reaction energetics.[158] Thus, the artificial interface charge transfer further impacts the reaction energy.[159] On the Helmholtz plane, the partial charge generated by the overlap of the solvent and metal charges is independent of the band arrangement (Fig. 8C).[160] The nudged elastic band, meta-dynamics, and average force potential determine the transition state.[161–164]

In the H-shuttling model, H_2O and adsorbed *H molecules are shuttled from the surface to the adsorbent. The proton–electron transfer during the shuttle process provides a potential barrier to the hydrogenation of eCO_2RR intermediate groups. Meanwhile, compared to the explicit solvent model, potential transfer resulting from charge transfer along the pathway is not taken into consideration. Although the simplicity of the H-shuttling model is convincing, more detailed models are urgently required to evaluate the feasibility and accuracy of these assumptions. The explicit solvent model combines the central molecule and its surrounding solvent molecules as a system for processing. Similar to general cluster models, accurate theoretical calculation results can be obtained by using more solvent molecules. Due to a large number of solvent molecules, it is often necessary to first construct a cluster structure and perform molecular dynamics simulations to obtain a satisfactory initial structure before carrying out quantum chemical calculations. Relying entirely on the introduction of explicit solvents to reflect solvent effects will inevitably result in an extensive calculation system. Moreover, the conformation of explicit solvents is extremely complicated, which cannot achieve correct handling by separately studying the static potential energy surface.

The implicit solvation model allows for the consideration of solvation effects without directly studying a large number of solvent molecules, but instead focusing on the target molecules. The current popular implicit solvent models based on the polarizable-continuum model ignore the structure and distribution of solvent molecules. The solvent is abstracted as an infinitely extended continuum dielectric, surrounding the hole occupied by the solute molecule. By treating solvation as a polar interaction between the surface of the solute molecule and the solvent background, the solvation effect can be approximately described by the dielectric constant. However, the disadvantage of implicit solvent models is that they cannot handle systems in which the solvent participates in the reaction or systems with strong interactions between the solute and solvent (such as hydrogen bonds). The influence of implicit solvent models on the geometric structure and vibration frequency is minimal for neutral molecules or local non-ionic conditions. For cases with significant local charges, the optimized structure without

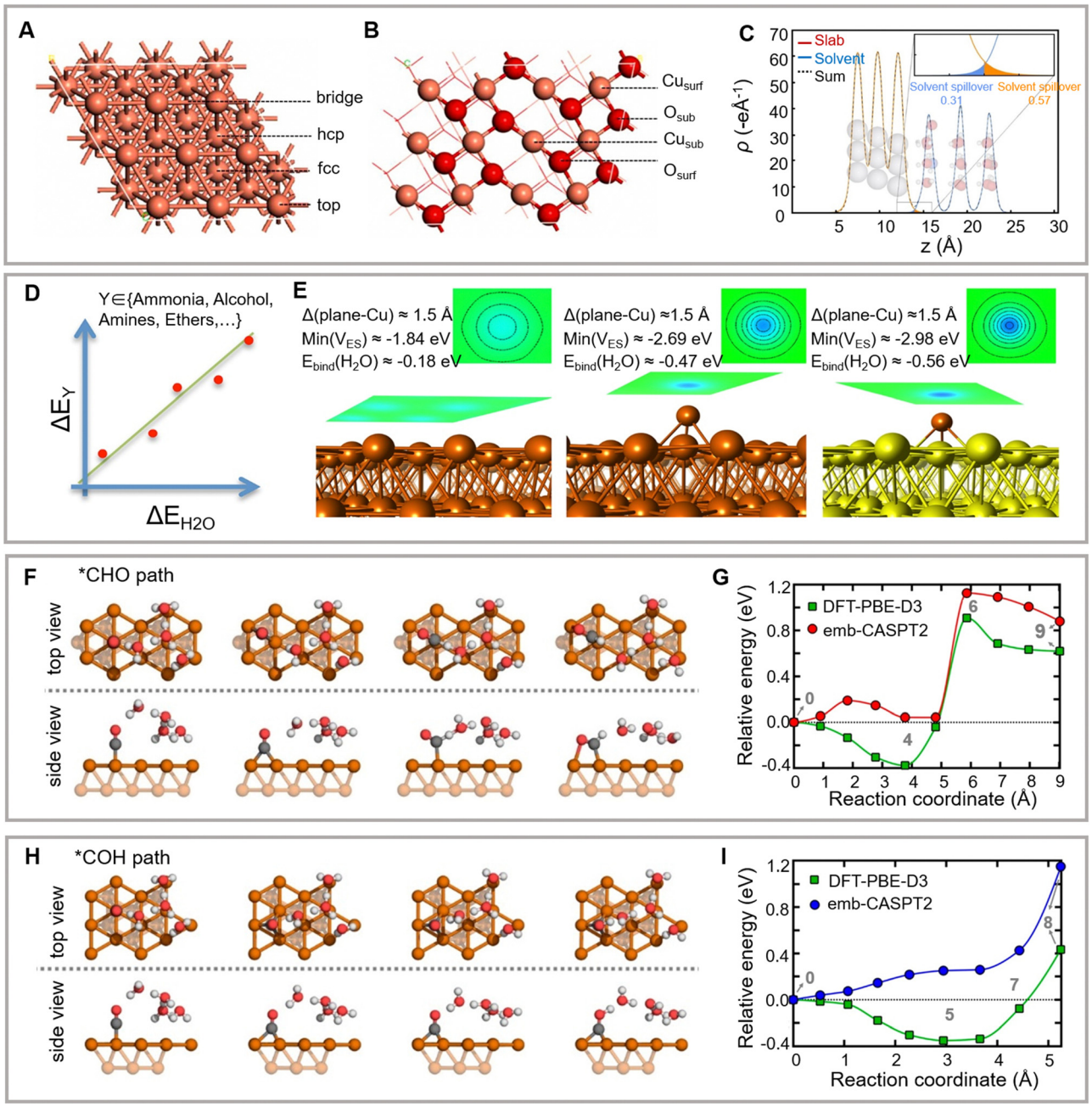

Fig. 8 (A and B) Surface structures of Cu(111) and CuO (111) facets with labeled adsorption sites. Reproduced with permission from Liu *et al.*[153] Copyright 2021 Elsevier. (C) Effective fractional charge of a proton in the outer Helmholtz plane. Reproduced with permission from Nørskov *et al.*[160] Copyright 2018 Spring Nature. (D–E) Electron density redistribution on copper surfaces. Reproduced with permission from Nørskov *et al.*[167] Copyright 2018 American Chemical Society. Critical structures optimized in vacuum from the *CHO path (F) and *COH path (H) on the Cu(111) facet. Energy curves for forming *CHO (G) and *COH (I). Reproduced with permission from Carter *et al.*[168] Copyright 2021 American Chemical Society.

considering the solvent model may differ significantly from the actual structure in the solvent environment. Herein, it is recommended to add implicit solvent models in the CO_2RR system to avoid the risk of obtaining qualitatively incorrect results for specific systems. Considering the possible differences in the potential energy surface of the reaction path under the solvent and gas phase at the three-phase interface of the CO_2RR reaction, all calculations should add an implicit solvent model, and explicit solvent models should be considered when necessary.

3.1.2. Mechanism prediction. The model based on the concerted proton–electron transfer step of the computational hydrogen electrode is not directly applicable to the proton–electron transfer step involving decoupling. Sequential proton–electron transfer steps have been observed in metal and oxide electrocatalysts. The effect of pH on the RHE scale has also

been experimentally demonstrated. Generally, the computational hydrogen electrode model of eCO_2RR on the Cu(211) facet has been initially calculated using the modified Perdew–Burke–Ernzerhof XC functional.[165,166] The proton-coupled electron transfer steps on Cu(211) have been predicted to occur in the following sequence: $CO_2 \rightarrow *COOH \rightarrow *CO \rightarrow *CHO \rightarrow *CH_2O \rightarrow *CH_3O \rightarrow CH_4 + O*$.

The linear correlation between the adsorption energies of similar intermediates enables the reduction of the complexity of theoretical models. Moreover, Sabatier-type activity diagrams are utilized for simultaneously analysis of multiple materials. According to the linear relationship of the binding energies between eCO_2RR intermediate groups and surface atoms, the U_L (ΔG) of proton–electron transfer is a linear function of the single intermediate binding energy. The breakage or circumvention of the linear relationship between eCO_2RR and the intermediates of electrocatalytic oxygen evolution and reduction reactions has recently attracted significant attention. For example, Nørskov and colleagues have demonstrated that the electrostatic well on a metal electrode surface may polarize the overhanging solitary pair in the case of a lone pair surface bonding to induce strong electrostatically driven bonding (Fig. 8D).[167] These strong electrostatic interactions can break the linear proportionality between the binding energies of unsaturated intermediates and molecular species. The robust polymerization of the CO dimer enables the formation of $*C_2O_2$, which further explains the preference of the Cu(100) facet for the synthesis of ethylene and ethanol over methane (Fig. 8E). This study opens a novel avenue for designing a new approach for breaking the linear relationships of the adsorbed intermediates on the catalyst surface.

Compared to the methods mentioned above, the water-solvation H-shuttling model considers the proton-coupled electron transfer step and the kinetic barrier of explicit water molecules. This model has been used to simulate eCO_2RR on the Cu(111) facet (Fig. 8F–I).[78,168,169] Owing to the low barrier, the H_2O-assisted $*CO \rightarrow *COH$ H-shuttling favors *CO reduction over *CHO formation compared to the computational hydrogen electrode model. However, this difference may also be attributed to the reactivity of the simulated copper facets in the above two studies. The computational hydrogen electrode model uses the Cu(211) facet, whereas the water-solvation H-shuttling model uses the Cu(111) facet.

3.2. Kinetics and pathways of C_2 product formation

3.2.1. *CO dimerization. The *CO generation pathway can be analyzed using nudged elastic band, dimer, H-shuttling, and meta-dynamic methods. For the Cu(111) facet, the activation energy of the reduction of CO_2 to *CO can be obtained using the explicit solvent method through nudged elastic band transition state search and the H-shuttling method.[170] Moreover, this model construction requires a low overpotential to reach the kinetic threshold of 0.75 eV. The H-shuttling model based on meta-dynamics exhibits fewer surmountable obstacles than the explicit solvent model on the Cu(100) facet.[82,170] The net barrier (0.4 V *vs.* RHE) between CO_2 (g) and *COOH has been estimated at 0.8 eV. In contrast, formate is considered the secondary choice, as the free energy difference between $*OCH_2O$ and *OCHO is 1.6 eV. In conclusion, *CO is the critical eCO_2RR intermediate for synthesizing C_{2+} products.

The related theoretical research has been conducted based on different models and approaches due to the complex pathway. This increased complexity can be attributed to the cation-induced field at the interface significantly affecting the C_{2+} intermediates and the corresponding additional degrees of freedom. *OCCO possesses an insurmountable dimerization barrier of >1 eV on different active facets in a vacuum.[171,172] However, electrolyte effects render *OCCO stable concerning 2*CO, thus facilitating dimerization. The Cu(211) facet features exposed under-coordinated surface copper atoms and is, therefore, less stable than Cu(100) and (111).[173,174] Under standard electrochemical conditions, the corresponding stability order is Cu(100) facet $>$ Cu(111) facet $>$ Cu(211) facet. The eCO_2RR activity order is Cu(211) facet $>$ Cu(100) facet $>$ Cu(111) facet, indicating that the Cu(211) facet exhibits lower barriers for the formation of C_{2+} products.[175] The charge and field distributions of the implicit solvent model will not be localized. However, localization is still necessary owing to the explicit cations. Gordon and colleagues have reported that the dimerization barrier at 0 V on the Cu(100) facet is only 0.6 eV in the case of continuous charge distribution in the solvent.[154] Generally, the sensitivity of water solvation and the cation-induced field may induce significant changes in the barrier of CO dimerization on different copper facets, with values of 0.53–1.3 eV obtained for the Cu(100) facet and values of 0.89–1.7 eV obtained for the Cu(111) facet.

3.2.2. C_2 pathways. The theoretical prediction of methods for improving C_{2+} product selectivity is significantly essential. In theoretical calculations, several physicochemical factors of C_{2+} selectivity on metal electrodes must be considered.

The first factor is the local pH surrounding the active site, which directly affects the eCO_2RR pathways and product distributions in different theoretical calculation systems.[176–178] Under neutral conditions, *CO is coupled with *COH to form a new C–C bond, whereas *CO dimerization is dominant under alkaline conditions. It is worth noting that other factors, such as the ion buffer effect and mass transfer, also influence the local pH value. The buffer solutions ($CO_2/H_2CO_3/HCO_3^-/CO_3^{2-}$ equilibria or $KHPO_4$) are sensitive to pH, electrolyte components, and buffer capacity, which cast a vital impact on the generation of different concentrations of carbonaceous intermediate species.[179–182] Dunwell and colleagues have explored the primary carbon source using *in situ* Fourier transform infrared experiments with isotope labeling, which excludes the controversy about the natural source of CO_2RR products.[183] The buffer anions enhance CO_2RR performance by increasing the effective reducible CO_2 concentration in solution through rapid equilibrium exchange between CO_2 and bicarbonate. Meanwhile, the mass transfer of reactants is of great significance for improving C_{2+} synthesis.[184] Nanostructure optimization and active site engineering still cannot effectively improve mass transfer. It is crucial to supply CO_2

diffusion to the catalyst surface by gas-diffusion electrodes based on CO_2 electrolyzers.

The second factor is the overpotential, which determines the activation energy barrier and selectivity of the C_1 and C_{2+} pathways. Theoretical studies suggest that C_2H_4 is formed by *CO dimerization at low overpotential, whereas *CHO/*CO coupling reactions dominate at high overpotential.[185] Presently, the recognized mechanism involves the formation of C–C bonds *via* *CO coupling on the catalyst surface or CO molecules in solution with *CHO adsorbed on the electrode surface.[154] Although the form of CO is still controversial, the applied potential certainly affects C_{2+} product selectivity.

The third factor is the oxidation state of surface metal atoms. Numerous experiments have proven that the oxidation state of surface Cu atoms plays an important role in eCO_2RR.[102,186,187] For example, Goddard and colleagues have theoretically predicted that the coupling of Cu^+ and Cu^0 sites promotes CO_2 activation and *CO dimerization in oxide-matrix-embedded metals.[161] In addition, $*CO_2$ at Cu^0 sites can be stabilized by $*H_2O$ at adjacent Cu^+ sites further enhancing the activation of CO_2. Meanwhile, *CO species adsorbed at Cu^+ and Cu^0 sites possess opposite charges (positive in the former case and negative in the latter case), making them electrostatically attracted to each other.

The fourth factor is the exposed active facet. The energy distributions depend on the atomic structure of the catalyst surface.[188,189] Moreover, it is essential to consider surface reconstruction to achieve C–C coupling during theoretical analysis. The last factor is dissolved cations and anions. Section 3.3 focuses on the analysis of electrolyte-ion accelerators and buffering effects.

3.2.3. Kinetics and reaction barriers. The pathways of CO_2 conversion to C_{2+} products are complex and follow the activation energy trend of proton–electron transfer to different intermediates. Explicit solvent models and nudged elastic band barrier calculation of various metals have demonstrated that proton–electron transfer to the oxygen terminus of intermediates is generally easy. In contrast, transfer to the carbon terminus is more complicated.[18,190,191] Similarly, explicit solvent meta-dynamics and H-shuttling barrier calculations demonstrate the hydrogenation of oxygen atoms during direct *H transfer steps.

Electrochemical kinetics characterizes the rate, selectivity, and intermediate coverage, which are all critical functions of reaction conditions.[192,193] However, owing to the dependence of the rate index on energy, the prediction of the rate-determining steps is subject to significant uncertainty. Therefore, general trends are considered more reliable than absolute ratios. The C_2 dynamic model tends to the initial C–C coupling step. The coupling barrier for *CO dimerization increases with the increasing cathode potential, whereas the coupling barrier of *CO–*CHO dimerization decreases with increasing overpotential.[154] Kinetic analysis has revealed that an appropriate overpotential can optimize the C_{2+} product yield, consistent with the experimental results obtained for the Cu(100) facet. Owing to the pH modification of the models, all hydrogen transfers have been observed to be less favorable than C–C coupling under alkaline conditions, which may explain the higher C_2 selectivity at high pH.

Meanwhile, rate-limiting electron transfer in the eCO_2RR process has been a recurring and controversial topic in various theoretical studies.[154,194] Experiments have revealed that C_{2+} products with increased pH exhibit a lower initial potential; thus, *CO dimerization was assumed to exhibit rate-limited electron–proton transfer decoupling. Theoretical simulation has revealed that the limited electron transfer uncoupled from electron transfer exhibits absolute potential dependence, and the reaction process is independent of the pH.[154] The dependence on the absolute potential (*vs.* SHE) may result from (i) proton–electron transfer from the proton source (H_2O) during the increase in pH or (ii) field stabilization through chemical dipole steps. Particularly, the initial potential decreases with an increase in the pH towards alkalinity. The current density of HER on the metal surface depends only on the potential.[176]

The effect of pH on C_{2+} selectivity has been investigated using kinetic models.[136] C_{2+} activity increases at a high pH value and depends on the absolute potential.[195] Jaramillo and colleagues have explored the complete dependence of C_{2+} product activity, which is ascribed to the earlier determination of the proton–electron transfer rate. Generally, the main qualitative characteristics of the experiment are consistent with those obtained theoretically. At high overpotentials, the decrease in C_{2+} product yield is due to the decrease in CO coverage at the beginning of the formation of C_1 products. As C_{2+} productivity is synchronized with CO coverage, the effect of the reduced coverage on C_{2+} production activity is more significant than that on C_1 production activity.

3.3. Electrolyte effects

The influence of electrolytes cannot be neglected in theoretical simulations as the electrolyte participates in the reaction by interacting with reactants, catalyst surfaces, intermediates, and products.

3.3.1. Cation effects. The near-surface double-layer ions affect the eCO_2RR pathway and thus cast an influence on the product distribution. Early experiments have revealed that eCO_2RR selectivity is affected by alkaline cations in the electrolyte, with larger cations favoring C_{2+} products.[196] Notably, larger cations are more easily adsorbed on the cathode and increase the outer Helmholtz surface potential and the pH around the active site, to promote C_{2+} product selectivity. Similarly, the local pH decreases with the introduction of larger cations owing to the buffering effects.[197] Moreover, larger cations exhibit lower pK_a values. As limited mass transport increases in the local pH, this pH change may be offset by large cation buffering.[198] The resulting reduction in pH enables the maintenance of a higher CO_2 concentration on the cathode surface, thus facilitating the reduction of CO_2.

A consistent theoretical explanation of the effects of cation size requires the exclusion of mass transport constraints (Fig. 9A). For example, Bell and colleagues have explored the effects of cation size on catalyst activity and selectivity at low

overpotentials (Fig. 9B and C).[199] In addition, another study has evaluated the effects of cation size on the energetics of eCO_2RR intermediates using the Bayesian error estimation functional (vdW).[200] They have further found that the cation-induced electric fields on the outer Helmholtz surface significantly stabilized $*CO_2$ intermediates. Moreover, an increase in the size of the cations in the outer Helmholtz plane is the crucial factor for enhancing the C_{2+} product, whereas larger cations prefer to be located on the catalyst surface (Fig. 9D).[201] Another study has revealed that the mechanism of a similar cationic accelerator effect changes with the variation of overpotential and active facets.[202] At low overpotential, the cation size strongly affects the onset potential of C_2H_4 synthesis. CH_4 production is favored at higher potential with a cation size-independent onset potential. Moreover, DFT Perdew–Burke–Ernzerhof calculations have revealed that cations firmly stabilize OCCO* and OCCOH* adsorbents, thus promoting the preparation of C_{2+} products.[199]

3.3.2. Anion effects. The type of anion present in the electrolyte mainly affects the buffering, intermediate stability, surface roughness, and other aspects, thus influencing eCO_2RR activity and selectivity (Fig. 9E).[203,204] Recent Raman spectroscopy results are consistent with earlier theoretical predictions that the co-adsorbed halide ions increase the amount of adsorbed *CO on copper (*i.e.*, slightly promote *CO binding).[205,206] The resulting increase in the *CO coverage contributes to C–C coupling. Furthermore, the co-adsorbed anions increase the positive charge on the carbon atom of *CO, thus changing the local charge state of this intermediate. Due to the π-back-donation from copper, carbon atoms adsorbed on the adjacent anionic-free surface sites become more negatively charged. The two *CO molecules with opposite

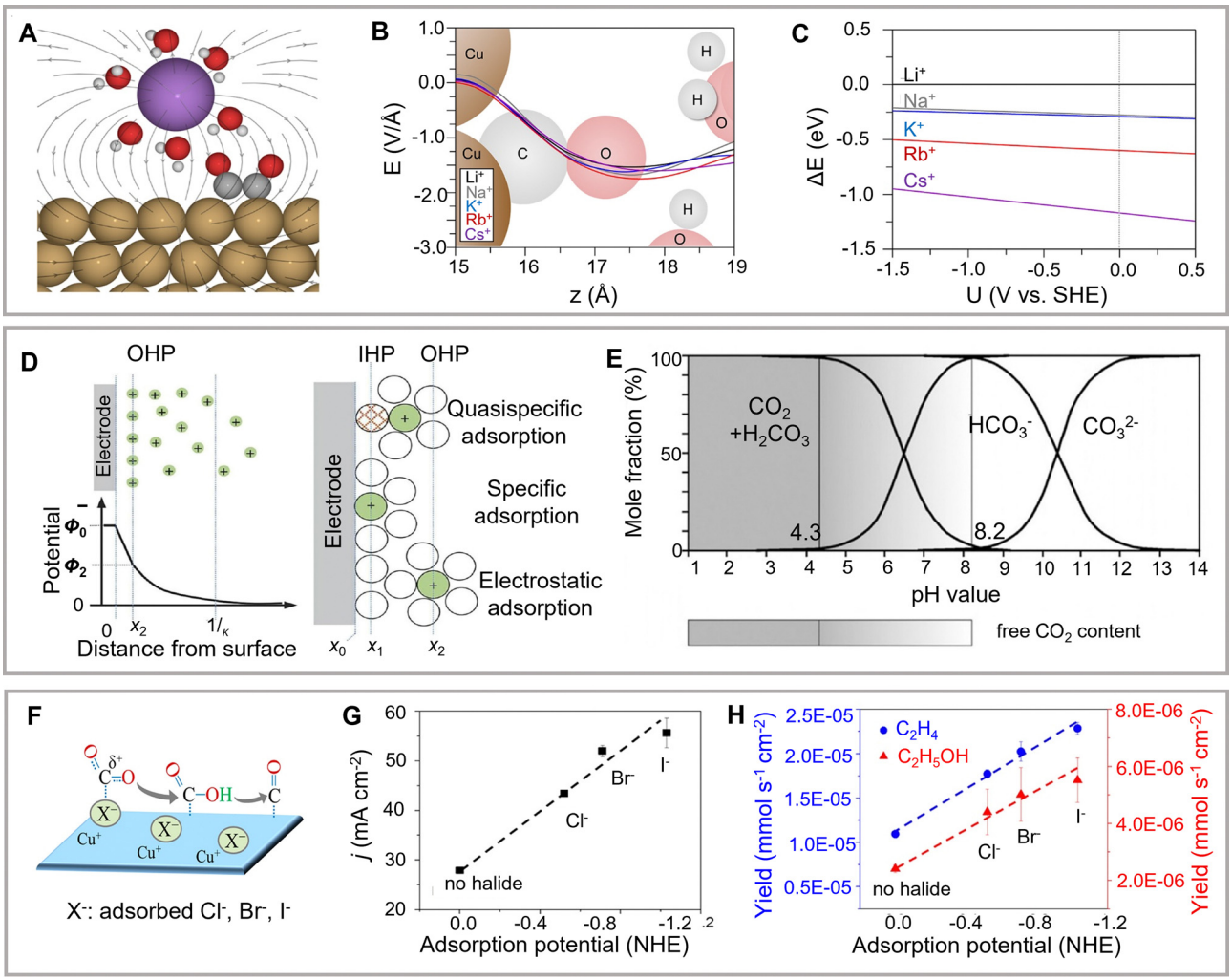

Fig. 9 (A) Scheme of cation effects. (B) Electric field distributions near the center. (C) The energy change for bringing solvated cations at the Cu(111) facet. Reproduced with permission from Bell *et al.*[199] Copyright 2017 American Chemical Society. (D) Model showing accumulated cations and depleted anions in the vicinity of the electrode. (E) The modified model involves specific adsorption at the inner Helmholtz plane. Reproduced with permission from Dong *et al.*[201] Copyright 2021 American Chemical Society. (F) Scheme showing the effect of anions. (G) Current density and (H) production rates of ethylene and ethanol in different electrolytes. Reproduced with permission from Cuenya *et al.*[207] Copyright 2017 American Chemical Society.

charges effortlessly combine to form a dimer (*OCCO), which is subsequently converted into C_{2+} products.[121] However, Carter and colleagues have suggested that anionic co-adsorption should induce more robust π-back donation. The carbon atom of the adsorbed *CO intermediate becomes more negatively charged, and the C–O bond is weakened (Fig. 9F).[207] When the adsorbed anions on the metal surface contribute to the negative charge, the electron-rich metal favors π-back donation.[208] The corresponding *in situ* Raman spectra have revealed the ability of halogen anions (Cl^-, Br^-, I^-, ClO_4^-) to bind to copper. Thus, this evidence suggests that an increase in the amount of co-adsorbed anions promotes a stronger π-back donation. The weakening of the C–O bond results in a more excellent eCO_2RR activity (Fig. 9G and H).[207] Although the effect of anion adsorption on the exact change of *CO charge remains controversial, anions undeniably play a significant role in C_{2+} product synthesis by regulating the coordination environment of *CO.

3.3.3. Solvent effect. The concentration, type, buffer capacity, and pH of the electrolytes affect the local reaction conditions and the product distribution, significantly influencing the final catalytic performance.[179,209,210] The complexity of electrochemical systems hinders the investigation of direct correlations between individual parameters and indicators of electrocatalytic performance. Therefore, the role of different electrolytes still needs to be further explored.

Electrolyte concentration is the primary consideration. To further evaluate the impact of different electrolytes on CO_2RR, it is necessary to deeply understand the interaction among the electrolyte, matrix, and intermediate species. Single properties of the relative dielectric constant or pK_a are insufficient to describe the effect of the solvent on CO_2RR activity and selectivity. The potential, solvent, and ion models should be clarified to investigate the electrochemical activation energy, which may influence the reaction kinetics and selectivity. Numerous corresponding theoretical methods have been developed.[185] However, the same processes measured using various methods have comparatively different amounts of energy. CO_2RR energetics have been theoretically investigated by implicit solvent models, which include explicit solvent models with atomized water and ions and H-shuttling models with protons shuttling back and forth from the surface. Goddard and colleagues have applied quantum mechanics methods to develop a mechanistic understanding of the processes of copper.[176] The energetics of reaction pathways on Cu(111) with variable pH have been further investigated using a hybrid of H-shuttling and implicit solvent models. C_{2+} production is kinetically suppressed under acidic conditions (pH = 1). The selectivity for C_{2+} products arises by kinetically blocking C_1 pathways under alkaline conditions (pH = 12). However, the theoretical model shows higher C_{2+} selectivity under alkaline conditions, which is similar to the experimental results. The application of solvent models needs to be further optimized and explored in the future theoretical simulations.

3.3.4. Kinetic simulations. For the comprehensive evaluation of selectivity and activity in electrocatalytic CO_2RR, kinetic barriers between different intermediates should be considered.[211–214] Currently, the kinetic simulations of CO_2RR primarily focus on electrocatalysis in pure water. However, in the electrochemical interface, solvated ions can serve as mobile countercharges attracted by the electrode, which has a non-negligible impact on the electrocatalytic processes occurring at the interface. Ionic effects can be explored at a static level using the nudged elastic band (NEB) method.[215] Chen and colleagues have investigated the influence of cations on the electrocatalytic pathway of CO_2RR on Ag(111) using an explicit model combined with the NEB method.[216] The calculation shows that the local cation-induced field can significantly stabilize the key intermediates, including *CO_2 and *COOH, while reducing the overpotential for product formation.

Traditional simulations often employ the NEB method to describe reaction processes at a static level, which cannot accurately capture systems with dynamic solvent behavior. To solve the above issues, full dynamic simulations can be applied to sample free energy surfaces. However, if the intermediate state is separated by a high kinetic energy barrier, standard unbiased *ab initio* molecular dynamics (AIMD) simulations will be impractical. Various algorithms (including constrained molecular dynamics, umbrella sampling, and metadynamics) have been introduced to promote sampling potential energy surfaces during CO_2RR processes.[217–219] Explicit solvent models incorporating the above algorithms can provide a relatively straightforward solution to evaluate ionic effects. Liu and colleagues have investigated the influence of different alkali metal cations on C_{2+} product synthesis on the Cu(100) facet using a combination of explicit solvent models, AIMD simulations, and free energy sampling techniques.[220] As the radius of alkali metal cations increases, the reaction free energy and kinetic barriers of key steps involved in the production of C_{2+} species (such as CO dimerization to OC–CO) gradually decrease.

Another challenge in current kinetic simulations is the limitation of the electron reservoir in the simulations. Most simulations are conducted under constant charge conditions, resulting in the lack of potential variation throughout the reaction process. Nørskov and colleagues have proposed a straightforward method based on the ideal capacitor model, which only needs to calculate the barriers and the corresponding surface charges at the initial, transition, and final states under constant charge simulations.[221] The energy at different potentials can be corrected using the following equation:

$$\Delta E = 1/2(Q_2 - Q_1)(\Phi_2 - \Phi_1)$$

where Q is the surface charge (Hirschfeld or Bader charge) and Φ represents the work function. This correction can be used for kinetic simulations to explore the kinetic barriers under constant potential conditions. To consider the electrocatalytic system beyond the static level, constant potential hybrid-solvent dynamic model with the implicit solvent and the ''slow-growth'' approach is a potential strategy to evaluate the kinetic potential barrier of electrocatalytic processes more accurately.

3.4. High-throughput calculations

Artificial intelligence and big data analysis play an increasingly important role in modern technology, presenting new development opportunities in several fields due to the rapid development of computer hardware and software.[222,223] Recently, machine learning models have been applied to atomic simulations and electronic property predictions.[224,225] Machine learning enables the solving of the traditional Schrödinger equation to obtain the formation enthalpy, density function, basis group effect, recombination energy, chemical reactivity, atomization energy, dynamic density function, electronic ground state properties, transition state partition surface, polymer properties, electron transfer coefficient, crystal properties, atomic charge, dipole moment, electronic excitation energy, and electronic density function.[226] Developing density functional techniques has led to an unprecedented atomic-level understanding of catalyst surface reactions to develop suitable catalysts. A large number of prospective materials and a system composed of dozens of atoms may require several hours of calculations. It is impossible to achieve high-throughput catalyst screening through quantitative calculations. The rapid development of machine learning enables the performance of such screening using reasonable chemical models of specific reactions.[227,228] The atomic-level quantum chemical mechanisms enable the search for a suitable single or small descriptor to evaluate catalyst reactivity.

Zhou and colleagues have predicted the eCO_2RR performance of single-atom catalysts using a machine-learning model.[229] Based on two simulated materials (M-C_2S_2 and M-CNO_2), ΔG_{CO} heat maps have been predicted using machine learning, considering various bonding environments between metal and non-metal atoms. Taking the ΔG_{CO} of materials experimentally confirmed to be good electrocatalysts as a reference, the authors have preliminarily screened the most promising doping atoms and the most suitable non-metallic coordination environments for CO_2 reduction. Furthermore, considering the HER competition, catalytic systems with improved eCO_2RR selectivity (such as Sc-CN_3, Ti-C_2S_2, V-NP_3, Fe-C_2S_2, Co-CS_3, Ni-C_2NP, and Zr-CN_2S) have been screened by overlapping ΔG_{CO} and ΔG_H heat maps. This machine-learning research provides an effective method for optimizing the composition of single-atom catalysts and guiding the experimental exploration of eCO_2RR electrocatalysts.

4. *In situ*/*operando* spectroscopic investigation of the eCO_2RR

Reaction rates and selectivity determined by computational studies are well correlated with the corresponding experimental data. However, theoretical models focus on well-ordered electrocatalytic systems, whereas actual reaction systems are complex. Therefore, there is an urgent need to apply advanced *in situ*/*operando* techniques to explore eCO_2RR mechanisms under various operating conditions. Many vital issues of eCO_2RR (such as catalyst stability, critical intermediate identification and configuration, determination of catalytically active sites, and the influence of the reaction environment) can be clarified using the *in situ*/*operando* approach.[230–233] These techniques can capture the subtle physicochemical details of materials. The real challenge is in coupling eCO_2RR occurrence and meeting the requirements of operating conditions.

4.1. Optical characterization techniques

Optical spectroscopy employs non-ionizing radiations ranging from far infrared to deep ultraviolet. *In situ* catalytic processes, such as electron transfer and bonding, have been explored with excellent sensitivity and rates using inelastic light scattering. In the eCO_2RR process, the structural evolution of catalysts and the vibration frequency of the adsorbed intermediates can be monitored by various characterization methods. For example, optical Raman and infrared spectroscopy are fingerprint techniques used to identify the vibration patterns of key intermediates.[234]

4.1.1. Raman spectroscopy. Raman spectroscopy can detect signals in the low-wavenumber region of metallic bonds and monitor catalyst surfaces with higher oxidation states. This method is suitable for recognizing catalytically active sites and key intermediates and analyzing the pathways of solid–liquid interface electrochemical reactions. Moreover, water present in the eCO_2RR system exhibits a low Raman scattering cross-section. Considering that the inelastic Raman scattering signals are acquired from the illuminated point, *operando* Raman reactors typically have an observation window above the catalyst surface and share incident illumination in a confocal configuration (Fig. 10A).[233] The beam energy and flux are compromised to optimize irradiation intensity and prevent sample damage. A water immersion objective with a long working distance is generally used to enable the entry of a sufficient amount of electrolyte. A cover glass is placed on the target catalyst. Thus, the possible optimized detection sensitivity can be achieved without electrochemical distortion and lens pollution.

In situ Raman spectroscopy has been utilized to explore the surface structure catalysts. Xiong and colleagues have resorted to *in situ* Raman for proving a large number of grain boundaries on Cu_2O superparticles.[102] The peaks of *in situ* Raman spectra observed at 2060–2080 cm^{-1} are assigned to the C–O stretching mode of the *CO intermediate (Fig. 10B). The *CO peak is enhanced with decreased potential, and the intensity of this peak becomes lost with a further decrease in the overpotential (−0.95 V *vs.* RHE). This behavior has indicated the conversion of *CO into C_2H_4 and other products. The *CO peak of the control Cu_2O cube is weak, which is consistent with the eCO_2RR results. $HCOOH/H_2$ has been observed as the main product, and the *CO intermediate cannot be formed at low overpotentials. Considering the direct impact of local pH changes near the electrode surface on electrochemical CO_2RR, Francisco and colleagues have integrated *in situ* Raman technology with a continuous flow cell to achieve real-time detection of local pH near the GDE under reaction conditions.[235] The CO_2–OH^- neutralization formed CO_3^{2-} and HCO_3^- have been

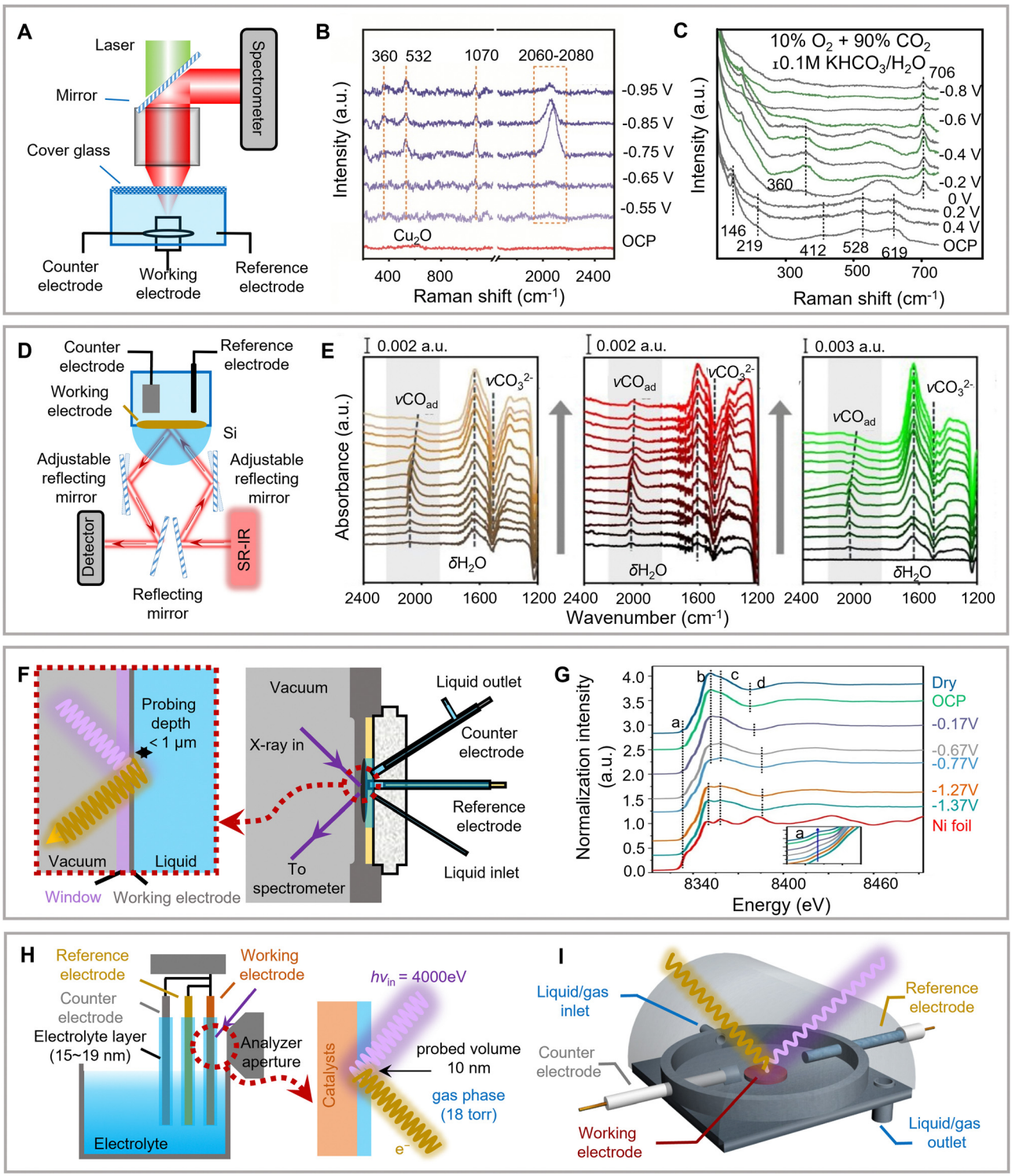

Fig. 10 (A) Schematic illustration of the *operando* Raman spectroscopy setup. (B) *In situ* Raman spectra of Cu_2O superparticle-CP3 during eCO_2RR. Reproduced with permission from Xiong *et al.*[102] Copyright 2022 WileyVCH Verlag GmbH & Co. KGaA, Weinheim. (C) *In situ* surface-enhanced Raman spectroscopy of the copper catalyst in 10% O_2/90% CO_2 feed solvent. Reproduced with permission from Lu *et al.*239 Copyright 2020 Spring Nature. (D) Schematic illustration of the *operando* infrared spectroscopy setup. (E) *In situ* ATR-SEIRAS spectra on different copper oxides as a function of the applied potential. Reproduced with permission from Gao *et al.*[82] Copyright 2022 American Chemical Society. (F) Schematic illustration of the *operando* XAS setup. (G) XANES spectra of metal–N–C at various applied potentials in a CO_2-saturated solvent. Reproduced with permission from Jiang *et al.*[251] Copyright 2022 American Chemical Society. Schematic illustrations of the *operando* XPS (H) and XRD (I) setup.

selected as the pH probes for *in situ* Raman characterization. The above pH probes have distinguishable Raman features and can be independently quantified. Meanwhile, the acid–base equilibrium between CO_3^{2-} and HCO_3^- can be utilized to derive the pH. As the *in situ* Raman tested, the HCO_3^- distribution extends 120 μm into the electrolyte, and the local pH on the cathode surface is 7.2. This demonstrates that the nominal overpotential reduction originates from the Nernst potential energy of the pH gradient layer at the cathode/electrolyte interface. Therefore, *in situ* microarea Raman spectroscopy has great potential for investigation of the local pH value near the GDE under working conditions. Although the spatial resolution and Raman sensitivity of *in situ* microarea region Raman are still limited, the above issues can be overcome by techniques such as surface-enhanced Raman.

Meanwhile, the extensive application of Raman spectroscopy begins with observing the surface-enhanced Raman scattering (SERS) effects.[236–238] To date, *operando* SERS has been used to monitor the metastable status of the catalyst and identify intermediates during the eCO_2RR process. *In situ* SERS has proved that surface hydroxyl species can significantly improve the eCO_2RR activity of Cu microparticle systems during co-electrolysis at a low O_2 concentration (Fig. 10C).[239] Cu microparticle catalysts can easily exhibit a surface-enhanced Raman signal, reducing the introduction of SERS-induced particles. Multiple peaks attributable to surface Cu_2O (Cu_2O_{surf}) have been observed at the open circuit potential. An additional peak appeared at 360 cm^{-1} after Cu_2O_{surf} has been removed at 0 V *vs.* RHE in the CO_2 atmosphere and disappeared at −0.4 V *vs.* RHE. Therefore, the intermediate species are unlikely to affect eCO_2RR significantly. In the O_2 atmosphere, a prominent surface hydroxyl peak appeared below 0 V *vs.* RHE. The SER spectra have demonstrated the characteristics of O_2 and CO_2 atmospheres. The critical difference in the SER spectra of CO_2 and O_2 + CO_2 atmospheres has been identified as the presence of surface hydroxyl species, which are responsible for the different eCO_2RR pathways observed with or without O_2 in the reaction atmosphere. Furthermore, Weckhuysen and colleagues have integrated *operando* SERS with sub-second time resolution and atomic force microscopy (AFM) to successfully monitor the dynamics of CO_2RR intermediates and Cu surfaces.[240] AFM results have demonstrated the SERS-active nanoparticles formed on the Cu surface after anodic treatment. Besides, a characteristic vibration band below 2060 cm^{-1} in *operando* SERS spectra has been observed, which should be ascribed to the dynamic *CO intermediate related to C–C coupling and ethylene production. Further investigations have concluded that anodic treatment and subsequent surface oxide reduction induced greatly enhanced roughness of the Cu electrode surface, resulting in fourfold improved CO_2RR efficiency toward ethylene. The detailed examples above demonstrate that *in situ* Raman/SERS can easily provide the microstructure information of the molecules on the electrode surface (interface). This technology has incomparable advantages in tracking phase structure transition and reaction intermediate transformation, which contribute to exploring the eCO_2RR reaction mechanisms.

4.1.2. Infrared spectroscopy. Infrared spectroscopy is a suitable technique for monitoring organic species adsorbed on the surface of metal electrodes based on specific absorption. The complexity of metal-catalyst surface characterization makes this method unsuitable for observing catalyst states. Nevertheless, infrared spectroscopy can provide the fingerprint identification of polarizable radical groups for the critical oxygen-related intermediates involved in eCO_2RR, which mainly exhibit absorption in the range of 800–1600 cm^{-1}. Owing to the short lifetime and a limited number of electrochemical intermediates on the surface, *in situ* Fourier transform infrared spectroscopic (*in situ* FTIR) methods are urgently required (Fig. 10D).[241–243] Surface-enhanced infrared absorption spectroscopy (SEIRAS) is sensitive to adsorbed intermediates with C–O bonds on the surface of the metallic catalysts. As eCO_2RR typically involves immersed and immobilized surfaces, the attenuated total reflection (ATR) infrared operating mode is commonly utilized to minimize interference from the electrolyte layer. Li and colleagues have investigated the active groups on the surface of Ir_1-Cu_3N/Cu_2O using ATR-SEIRAS to explore the primary eCO_2RR mechanism.[244] A peak has been observed at 1657.5 cm^{-1}, ascribed to water adsorption at −1.1 to −1.5 V. In contrast, the opposite characteristic peak of adsorbed H_2O has also been detected. The H_2O molecule only combines with the *COO intermediate on pure Cu_3N without forming a proton. H_2O molecules have been activated at the Ir_1 site of the Ir_1-Cu_3N/Cu_2O multisite catalyst, after which they are continuously consumed to produce protons. The newly generated *COO species have been rapidly protonated to form *COOH intermediates, which correspond to the more notable and stronger peak at 1218.3 cm^{-1}. In addition to the detection of the surface coverage of the above-mentioned *CO intermediate, the vital progress of *in situ* FTIR in CO_2RR includes the detection of new species on the electrode surface and the pH analysis on the electrode surface.

Furthermore, ATR-SEIRAS has been employed to investigate the eCO_2RR mechanism of oxide-derived Cu nanocrystals.[69,170,245] Three notable characteristic peaks have been observed in the open circuit voltage range of −1.2 V (*vs.* RHE). Characteristic peaks observed at −1520 and −1620 cm^{-1} are assigned to the desorption of HCO_3^- and the bending vibration of water molecules, respectively. The peak at 2040–2049 cm^{-1} corresponds to the stretching vibration of *CO linearly adsorbed on the interface (Fig. 10E).[82] It is worth noting that this characteristic peak experiences a slight red shift at negative potentials, which is caused by the Stark tuning effect under the action of a more negative electric field. Electron transfer from the catalyst to the 2π* orbital of *CO exhibits a negative correlation with the wavenumber of the ATR-SEIRAS peak. Further, the stretching band frequency of *CO adsorbed on OD-Cu-III has always been lower than those of OD-Cu-I and OD-Cu-V at different potentials. The interaction between the adsorbed *CO species and the OD-Cu-III catalyst is concluded to be stronger, promoting *CO dimerization. The study of

eCO_2RR kinetics requires *in situ*/*operando* experimental investigations of the quantitative correlation between the surface-mediated electrochemical reaction rate and interfacial intermediate concentration. Electrochemical *in situ* FTIR technology monitors the adsorption and desorption behavior of the intermediates, the electrode structure evolution, and the microenvironment of the electrode surface at the molecular level. This is of great significance to the rational design of catalyst structure and the exploration of new reaction mechanisms. Although *in situ* FTIR techniques have numerous advantages in studying the catalytic reaction at the electrode surface/interface, a series of problems will occur in the actual test process, such as the absence of any intermediate absorption peak, the strong infrared absorption peak of H_2O, and the red or blue shift of the absorption peak position. Therefore, it is necessary to improve specific test methods according to the existing system to obtain objective and accurate *in situ* FTIR results.

4.2. X-Ray characterization techniques

X-Ray characterization techniques complement optical characterization and help to overcome the limitations of catalyst surface analysis. *Operando* X-ray techniques have demonstrated outstanding potential for exploring the active sites and mechanisms of catalysts.[246,247] However, no direct applications of these techniques to eCO_2RR systems have been reported owing to installation complexity or limited central facilities.

4.2.1. X-Ray absorption spectroscopy. XAS is an excellent method for analyzing gaseous, liquid, and solid samples. It enables the indirect detection of adsorbed species by monitoring subtle changes in the coordination environment and state of target catalysts (Fig. 10F).[248,249] X-Ray absorption near-edge structure (XANES) spectroscopy provides element-specific information on the electronic structure, geometric bonding of absorbing atoms, and electron transitions from occupied to unoccupied states.[250] Premarginal peaks occur with the orbital hybridization induced by assortative species. Extended X-ray absorption fine structure (EXAFS) spectroscopy provides local structural information on the bond distances and coordination numbers around absorbing atoms. The observed coordination number is consistent with the theoretical particle size estimated from processed EXAFS data.

Jiang and colleagues have integrated *operando* XAS analysis and used an atom-dispersed nickel catalyst as a model, in which the isolated Ni sites are stabilized by pyrrole nitrogen in the form of $Ni–N_4$. A complete view of potential-induced structural changes at the atomic level during eCO_2RR has been achieved by the *in situ* investigation (Fig. 10G).[251] The XAS test during the CO_2RR electrolysis shows no obvious changes in Ni XANES under different potentials applied, suggesting the high stability of those isolated Ni active sites over graphene and thus ensuring a practical use in long-term electrolysis. Furthermore, Sargent and colleagues have systematically altered the organic linkers and metal nodes of a face-centered cubic MOF to regulate its CO_2 adsorption ability, porosity, and Lewis acidity.[127] *Operando* XAS has revealed the stability of MOFs under *in situ* operating conditions. With an increase in the CO_2 concentration, the above regulation plays an essential role in optimizing the binding mode of the *CO intermediate on the surface. Hwang and colleagues have conducted the XANES analyses of Cu-based nanoparticles during the eCO_2RR process.[252] *Operando* XANES spectra measured at −1.1 V *vs.* RHE have clearly shown that the oxidation state of the catalyst (Cu_2O) reduces toward metallic Cu. This observation is consistent with the other previously reported structural evolutions of oxide-derived Cu catalysts.[253] The reduced metallic Cu^0 has been fragmented, while producing the highest FE (73%) for C_2 + C_3 chemicals. The authors have also concluded that the fragmented Cu-based nanoparticles for CO_2RR deriving from the initially generated metallic Cu cast significant influence on the final catalytic performance. To sum up, *operando* XAS is able to capture and analyze the coordination environment of atoms and valence configuration of the catalysts during the eCO_2RR. The change of interface electrons, atomic structures, and oxidation state of active species can be tracked. However, *operando* XAS is a bulk detection technique by measuring the ensemble catalyst film and hence cannot precisely reflect the structural information of the catalytic reaction occurring at the solid–liquid interface. The new XAS technique, combined with other *in situ*/*operando* approaches and theoretical calculations, opens a novel approach to clarify the mechanism of eCO_2RR.

4.2.2. X-Ray photoelectron spectroscopy (XPS). XPS simultaneously measures the kinetic energy from a sample surface at a depth of several nanometers and provides a fingerprint of chemical and electronic state structures.[254] Considering the short inelastic mean free path (IMFP) of photoelectrons, XPS analysis is typically operated under an ultrahigh vacuum. Harsh test conditions make the *operando* electrochemical studies of solid–liquid interfaces very difficult.

Fundamental analysis of the chemical structures can be achieved by transferring materials from the electrocatalytic reaction reactor to the XPS chamber under vacuum. Such *ex situ* experiments have been widely performed for oxide-derived eCO_2RR catalysts. However, during sample transfer under environmental conditions devoid of electrochemistry, the rapid interaction between the reactants and solvent may affect the outcome of measurements. These *ex situ* XPS tests are conducted during the inevitable exposure of the sample to air, which induces changes in the oxidation state of the catalyst surface. Therefore, the natural catalyst surface structure cannot be captured.

A feasible strategy to solve this problem is constructing a reactor with an optoelectronic transparent graphene film as a pressure barrier. Using a technique similar to *operando* photoemission electron microscopy, a membrane-sealed flow cell electrochemical reactor can be employed for *operando* XPS characterization in an ultrahigh vacuum.[255,256] Another strategy is to separate the sample chamber from the electronic analyzer using a differential pumping and electrostatic lens system. This method enables the placement of an unsealed reactor in a sample chamber at near-atmospheric pressure (Fig. 10H). Ambient-pressure X-ray photoelectron spectroscopy (APXPS) recommends the application of synchrotron radiation

sources owing to their balance of incident photon energy, photoelectron IMFP, and photoionization cross-sections.[112] However, the electrolyte layer must be sufficiently thin (<20 nm) for adequate characterization under these conditions. Hence, future works must focus on the effective combination of vacuum XPS and *in situ* eCO_2RR tests or the development of *in situ*/*operando* APXPS. Further development of X-ray based *in situ* XRD characterization tests is required to detect the reaction stability of metal materials (Fig. 10I).[257,258]

4.3. Electron microscopy characterization

Electron microscopy characterization, including transmission/scanning electron microscopy (TEM/SEM), has provided atomic-level information on the morphological evolution and compositional changes of catalysts during a reaction. An in-depth study of the target reaction mechanism can be achieved by tracking subtle changes in the catalysts and electron transfer processes on the surface.

4.3.1. Liquid-phase transmission electron microscopy (LPTEM). *In situ* LPTEM is an instrumental approach for the real-time tracking of physical migration, morphological evolution, and compositional changes during catalytic processes.[259,260] The structure of the electrolytic cell used for LPTEM is shown in Fig. 11A. A flowing electrolyte is introduced around the microcell in the main observation window. This structure enables the detection of diffusion-limited reactions, such as eCO_2RR. However, there is a large gap between the test conditions of *in situ* electrochemical TEM and actual electrocatalytic conditions. The limited space of the internal electrode may result in uneven electric field distributions and the generation of hotspots, which promote activity near the electrode tip.[261] Moreover, high-energy electron beams can cause radiation-induced decomposition and sample damage, thus affecting the analysis of the variation in the material structure during the *in situ* tests.

Morphological changes under high-resolution operating conditions can be instantly recorded by *in situ* LPTEM, thus providing valuable information on the surface transformation mechanisms during the catalytic eCO_2RR. Liao and colleagues have observed the etching of MOFs during eCO_2RR using *in situ* LPTEM and identified the mechanism of the stability-controlled transformations from ZIF-67 to transition metal cobalt hydroxide (Fig. 11B and C).[262] Under slow diffusion conditions, the nanobubbles in the materials gradually move out. Transition metal cobalt hydroxide clusters are formed on the interface, which favors the formation of the porous structures (Fig. 11C). Furthermore, diffusion results in the rapid formation, aggregation, and remodeling of nanobubbles, thus inducing the formation of layered structures. Although LPTEM is not currently available for fully *operando* tests, this technique holds great promise for further applications. The demand of the ultra-high vacuum condition, the difficulty in the design of *in situ* TEM cells, and the possible damage from the electron beam to the catalysts are the existing challenges for developing *operando* TEM techniques.

4.3.2. Scanning electrochemical microscopy (SECM). SECM is used to realize single-entity electrochemical measurements to unlock the complexity of heterogeneity in nanocrystalline catalysts.[263,264] Unraveling the true structure–property correlations may promote the identification of nanocrystals with anomalous properties.[265] Baker and colleagues have separated single gold nanocrystals with well-defined surfaces and investigated their eCO_2RR responses using environmentally controlled SECM (Fig. 11D).[214] Considering the drop-casting of nanocrystal solutions on solid substrates, electrospray deposition methods have been employed to provide isolated nanocrystals with moderate area densities. Ye and colleagues have developed a nano-electrochemical cell on each attached nanocrystalline layer to accurately control the humidity, temperature, and gas atmosphere.[214] The hyperspectral data are obtained using local voltammetry experiments. The gas–electrolyte–catalyst triphasic boundary of the nano-electrochemical cell simulates the eCO_2RR gas diffusion electrode configuration. Comparing SECM and SEM images has revealed correlations between high current measurement and the catalyst location. SEM imaging after SECM exhibits droplet footprints, indicating the incomplete wrapping of the clustered nanocrystals (blue dots) or deformed particles by the electrolyte. The SECM image is obtained under favorable conditions for HER in an argon atmosphere of −0.9 V (*vs.* RHE) (Fig. 11E). In a CO_2 atmosphere, the cathode current of nanocrystals is continuously enhanced with an increase in the potential above −0.5 V (*vs.* RHE) (Fig. 11F). Lastly, the results reveal that {110}-tip rhomboid gold exhibits superior eCO_2RR selectivity and activity compared to the {111}-tip octahedron and the high exponential {310}-tip-truncated binormal prism. Notably, at low overpotentials, the electrode dynamics are expected to dominate the current response.

5. Optimization of the triphasic interfacial reaction system

The efficiency of eCO_2RR typically depends on the multistep proton–electron transfer process and the interfacial diffusion mass transfer kinetics. The former process is mainly affected by the crystal structure and active sites of the electrocatalyst, whereas the latter is affected by the wettability and physicochemical properties of the interface structure. The promising achievements in regulating the composition and structure of electrocatalysts are summarized in the previous sections. In traditional solid–liquid two-phase reaction systems, high selectivity for CO_2 reduction products can be achieved at a low current density. However, the low solubility of CO_2 in common electrolytes and the low liquid diffusion coefficient of the gas therein limit further improvements in the current density. In recent years, gas–solid–liquid triphasic interface models have been increasingly applied to study eCO_2RR.[266–269] The design and regulation of the micro-/nanostructure and interface properties of catalysts enable the adequate enrichment of the catalyst surface with CO_2 molecules in the form of adsorption

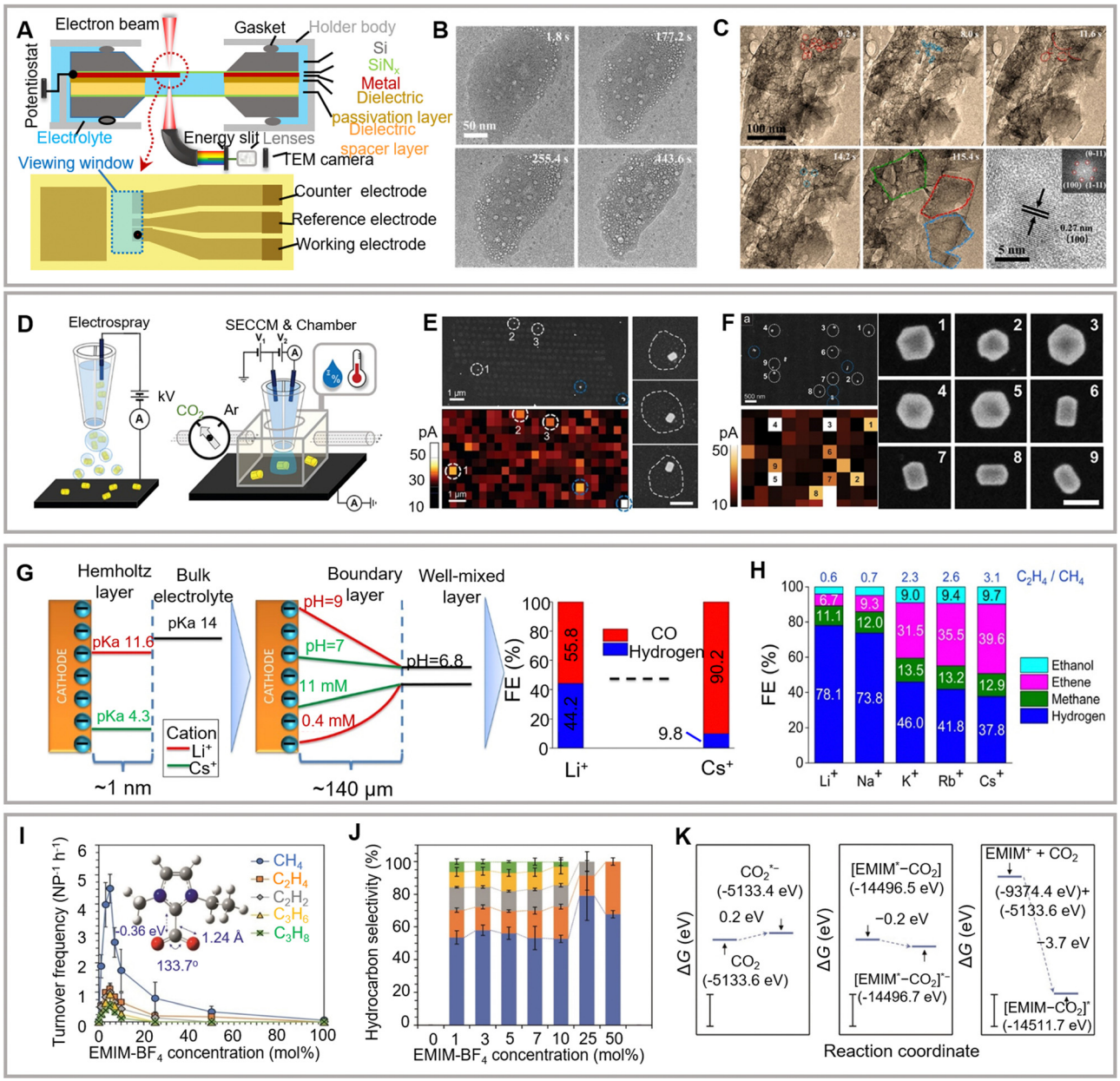

Fig. 11 (A) Schematic illustration of the *operando* TEM setup. Sequential TEM images tracking the transformation process of materials during the catalyst synthesis (B) and eCO_2RR (C). Reproduced with permission from Liao *et al.*[262] Copyright 2022 Elsevier. (D) Schematic illustration of the *operando* scanning electrochemical microscopy (SECCM) setup. SEM image and the corresponding SECCM map of metal nanoparticles under an Ar atmosphere (E) and CO_2 atmosphere (F). Reproduced with permission from Ye *et al.*[214] Copyright 2022 American Chemical Society. (G) pK_a of hydrolysis of hydrated Li^+ and Cs^+ inside the Helmholtz layer and in the bulk electrolyte and distribution of pH and CO_2 concentration in the boundary layer. (H) FE of eCO_2RR products with different electrolytes. Reproduced with permission from Bell *et al.*[197] Copyright 2016 American Chemical Society. (I) Turnover frequencies and (J) selectivity of hydrocarbon products formed plotted as a function of the EMIM-BF_4 concentration. (K) DFT-computed free energy cost, ΔG, of formation of different intermediates. Reproduced with permission from Jain *et al.*[282] Copyright 2019 Spring Nature.

bubbles or a continuous flowing gas phase. The optimization of the above reaction system enables overcoming the diffusion and mass transfer limitations of traditional two-phase systems, thus improving eCO_2RR efficiency at high current densities.

5.1. Optimization of electrolytes

Electrolytes participate in eCO_2RR by interacting with catalysts, reactants, intermediates, and products. Common aqueous electrolytes mainly contain inorganic salts, alkali metal cations, carbonate/bicarbonate ions, and halogen ions. A deep mechanistic understanding of the electrolyte effect helps to improve eCO_2RR activity and selectivity through efficient electrolyte design. The theoretical calculations summarized in previous sections indicate that different anions and cations exhibit different eCO_2RR activities.[270] Therefore, the influence of the electrolyte on the catalyst structure and the catalytic reaction

should be further explored to improve eCO_2RR activity and C_{2+} selectivity through practical electrolyte design.

5.1.1. Optimization of cations. The size of alkali cations strongly affects the product distribution of copper-based catalysts. The previously summarized theoretical studies have demonstrated that introducing alkali-metal cations can shift the outer Helmholtz layer potential and increase the local pH value on the surface to favor C_{2+} product formation (Fig. 11G and H).[196,197] Koper and colleagues have elucidated the mechanism of selected cations affecting eCO_2RR and competitive HER.[271] At high concentrations, cations significantly inhibit the HER and activate CO_2 in acidic environments. Non-acidic cations exhibit low repulsion at the interface and accumulate in the outer Helmholtz layer, thus exerting local promotional effects. On the other hand, acidic cations in alkaline electrolytes are hydrolyzed to enable a second proton reduction mechanism. Although the use of alkaline electrolytes inhibits HER, it results in the conversion of CO_2 into CO_3^{2-}, which cannot further participate in electrochemical reduction. This conversion results in one-way CO_2 conversion efficiencies of $<50\%$.[197] Although acidic environments increase the one-way conversion efficiency of CO_2, they also facilitate HER. To solve these problems, Sargent and colleagues have attempted to achieve a highly selective electrochemical CO_2 reduction by adding alkali metal salts under strongly acidic conditions (pH < 1).[272] The alkali metal ions adsorbed on the electrode surface can change the interfacial electric field distribution, restrict the migration of hydronium ions, and inhibit the HER. Meanwhile, the interaction between the electric field and the dipole moment of intermediates promotes the electrocatalytic reduction of CO_2.

The interpretation of cations effects has been further investigated. Bell and colleagues have proposed a theory for this buffering effect.[273] The pK_a of the cations decreases with increasing ion size. Suppose the pK_a is lower than the pH of the adjacent solution, the solvated alkali cations release H^+ as a buffer to adjust the pH on the surface, reduce the CO_2 conversion into CO_3^{2-} and HCO_3^-, and improve the CO_2 solubility at the interface. Meanwhile, Xu and colleagues have explored the effect of cation size on interfacial CO_2 concentration using *in situ* transmission infrared spectroscopy.[183] The interfacial CO_2 concentration decreases and depends on the rate of OH^- generation by electrolysis rather than on the buffering effect of alkali metal cations.

It is difficult to determine the degree of interaction between cations and electrode surfaces from an experimental perspective. Only some macroscopic physical parameters, such as electrode surface pH and interfacial CO_2 concentration, can be experimentally determined. The experimental determination of mechanisms is extraordinarily challenging and prone to conflicting theories. This pending problem requires applying *in situ* characterization techniques and computational simulation methods to gain a deeper understanding.

5.1.2. Selection of anions. In addition to cations, anions also play a significant role. Commonly used anions include CO_3^{2-}/HCO_3^- and halogen ions. The anion action mechanism depends on the anion type.[274] As the CO_2–carbonate–water balance helps to maintain a neutral overall pH value, the earliest electrolyte used for eCO_2RR is $Na_2CO_3/NaHCO_3$ and solutions of other salts (mainly those with CO_3^{2-} and HCO_3^- anions). The results of constant-current electrolytic eCO_2RR in various electrolyte solutions (KCl, $KClO_4$, and K_2SO_4) have revealed that alcohols and hydrocarbons are the preferred products in the above electrolyte.[201] The non-equilibrium high local pH region can explain this phenomenon near the surface of catalysts. As mentioned, OH^- is released during electrical reduction and is neutralized by HCO_3^-. Therefore, the pH may rise in the unbuffered electrolyte due to the inadequate neutralization used to favor the C_{2+} pathway over the C_1 pathway. Other works on the influence of solvent concentration also reflect the above trends. The rates of hydrogen precipitation and C_1 product formation increase with an increase in the concentration of the anion, which further suggests the influence of local pH effects.[275]

In addition to being a pH buffer and a proton source, bicarbonate can function as a CO_2 source. Dunwell and colleagues investigated the eCO_2RR mechanism in a bicarbonate electrolyte on a gold electrode using isotope labeling.[183] Owing to the dynamic chemical equilibrium between CO_2 and HCO_3^-, bicarbonate acts as a carbon source for converting CO_2 to *CO. OH^- is another commonly found anion in electrolytes, with alkaline environments favoring the formation of C_{2+} products. Both theoretical calculations and experimental explorations by Sargent and colleagues have revealed that OH^- not only reduces the binding energy of *CO dimerization for the formation of *OCCO but also promotes the charge imbalance between carbon atoms in *OCCO. The stronger dipole attraction in this intermediate and the reduction of the activation energy of *CO dimerization are finally realized.[111,272]

In recent years, the excellent performance of halogen ions in eCO_2RR has been demonstrated.[276,277] During the deposition process, these ions change the surface structure and morphology, generate unique crystal facets, and improve the roughness of the electrode material. The doping of halogen ions enables the activation of H_2O *via* the regulation of the electronic structure, which promotes the formation of critical active intermediates. Halogen ions can also be used as electrolyte additives to affect the adsorption of intermediates and active species. After adsorption on the inner Helmholtz layer, halogen ions engage in strong van der Waals interactions with active intermediates. Anions mainly affect the morphology of electrode materials during deposition, regulating the transfer of electrons from the electrode to CO_2. Zhai and colleagues optimized the different steps of C_{2+} product synthesis by leaching out halogen ions on the AgI–CuO tandem catalyst under CO_2RR conditions.[278] The leaching of iodine ions inhibits the reduction of CuO nanosheets to obtain stable active Cu^0/Cu^+ species, promoting *CO overflow. After the *in situ* leaching of iodine ions, the I-modified Ag structure tandem catalyst promotes the production of CO, and the Cu–Cu_2O heterojunction structure facilitates the formation of the key intermediate *OCCO for C–C coupling. Presently, progress has

been made to elucidate the interaction mechanisms of both cations and anions. However, deeper microscopic interaction mechanisms should be further investigated with the development of *in situ* characterization technologies and computational simulation methods.

5.1.3. Exploration of ionic liquids. As a new type of electrolyte, ionic liquids have been used in eCO_2RR systems. They exhibit several advantages, including a wide electrochemical window, low volatility, and high CO_2 dissolution and activation efficiency. Ionic liquids promote CO_2 adsorption, stabilize the reaction intermediates and effectively reduce the eCO_2RR overpotential.[279,280] Moreover, ionic liquids regulate product selectivity and current density by changing the structure of the double electric layer on the electrode surface.[281] In the case of imidazole-based ionic liquids, strong hydrogen bonding exists between the C_2 hydrogen and CO_2 in the imidazole ring. The longer alkyl side chain can provide a larger steric hindrance cavity to increase the solubility of CO_2. Based on the Lewis acid–base pair theory, strong Lewis acid–base interactions between anions and CO_2 molecules also favor efficient CO_2 dissolution and activation.

A comparison of the structural characteristics of CO_2 activated by water and 1-ethyl-3-methylimidazolium tetrafluoroborate has revealed that the interaction energy between carbon atoms in the imidazole ring and carbon atoms in CO_2 was −0.36 eV. On the other hand, the interaction energy between water molecules and CO_2 was only −0.11 eV (Fig. 11I).[282] CO_2 molecules undergo significant bending under the action of ionic liquids, and the resulting elongation of C–O bonds favors CO_2 activation (Fig. 11J). The influence of ionic liquids on the stability of intermediates and reaction pathways has also been explored (Fig. 11K). Sha and colleagues have found that the FE of C_2H_4 formation significantly increased with the modification of the copper electrode surface by using 1-ethyl-3-methylimidazolium nitrate.[283] For the decisive step of C–C coupling to produce C_2H_4, the presence of an ionic liquid reduces the energy barrier of *CO dimerization into *OCCO by 0.35 eV, thus favoring the formation of C_2H_4.

The interface between a metal electrode and an ionic liquid is very different from that between a metal electrode and an aqueous solution. At the applied potential, the dynamic transformation of the ionic liquid structure at the interface is slow. The reconstruction of the multilayer structure enables the formation of a significant double-layer structure. Characterization by vibrational sum-frequency generation spectroscopy has revealed that their structural transformation controls the reduction of CO_2 in ionic liquids.[284] However, it is difficult to directly detect the interfacial reaction mechanism in the structure of interfacial double electric layers with thicknesses of only several nanometers. At this stage, the formation and action mechanism of the interface structure have been discussed extensively using simulation calculations. In conclusion, although introducing ionic liquids into eCO_2RR systems may be a promising approach to explore, the insufficient stability of ionic liquids during eCO_2RR may complicate product detection and limit the practicality of large-scale reuse.

5.2. Optimization of the triphasic interface

The formation rate of eCO_2RR products is mainly limited by the following two factors. (a) Generally, a large overpotential is required to provide a high current density for eCO_2RR. However, HER dominates the reaction with increasing current density. (b) The solubility of CO_2 in water is relatively low. Beyond a certain threshold, the current density is no longer controlled by the chemical reaction kinetics but is determined by the proton diffusion process of CO_2. Therefore, the mass transfer of CO_2 molecules at the interface of catalytic materials greatly influences the reaction efficiency. Reduction in traditional solid–liquid two-phase systems is limited by slow diffusion and mass transfer, which results in low catalytic activity and product selectivity. These problems cannot be effectively solved by optimally regulating catalysts alone. Therefore, triphasic systems are introduced to solve the problem of the speed limit in the mass transfer process and ensure the effective progress of highly selective eCO_2RR at high current densities.

5.2.1. Optimization of the gas diffusion layer (GDL). Typically, GDL systems are used to improve electrocatalytic performance. In these systems, one side of a hydrophobic porous membrane is immersed in water. The opposite side directly contacts the gas phase to achieve a triphasic gas–solid–liquid interface.[285,286] Hydrophobic membranes are typically prepared using macroporous carbon paper as the substrate. The paper is covered with a microporous polytetrafluoroethylene (PTFE) layer and carbon particles, which enhance the hydrophobicity of this layer and provide a barrier for the liquid. The catalyst layer, typically composed of a metal film or a catalyst/carbon/polymer mixture, provides a triphasic interface for further reaction. Typically, polymer binders are ionic and water-conducting ionomers or hydrophobic polytetrafluoroethylenes (Fig. 12A).[287] During catalytic reactions, ions in the liquid phase can effectively contact the wetted catalyst surface, whereas the electrolyte does not penetrate the hydrophobic porous substrate. Gas-phase reactants can directly contact the catalyst and electrolyte through this substrate and participate in the reaction.

GDL-based cells have achieved higher current density than traditional H-type cells. Sargent and colleagues have reported a copper-based electrocatalyst at the mutagenesis interface with a high FE (70%) of ethylene and a maximum current density of $\sim$750 mA cm^{-2}.[111] Catalysts deposited on the GDL significantly increase the local concentration of CO_2 in the electrolytic cell. Hydroxyl ions on the copper surface reduce the energy barriers for CO_2 activation and *CO–CO coupling. In this study, a polymer-based GDL has been introduced to enhance operational stability. PTFE and carbon nanoparticles are divided into two layers, and the copper catalyst layer is sandwiched between them to form a graphite/carbon nanoparticle/copper/PTFE electrode. This adjustment effectively prevents liquid leakage from the GDL. Moreover, the as-designed GDL is sandwiched at the interface between separate hydrophobic and conductive carriers. This optimized structure can ensure constant and efficient ethylene selectivity during long-term electrolysis.

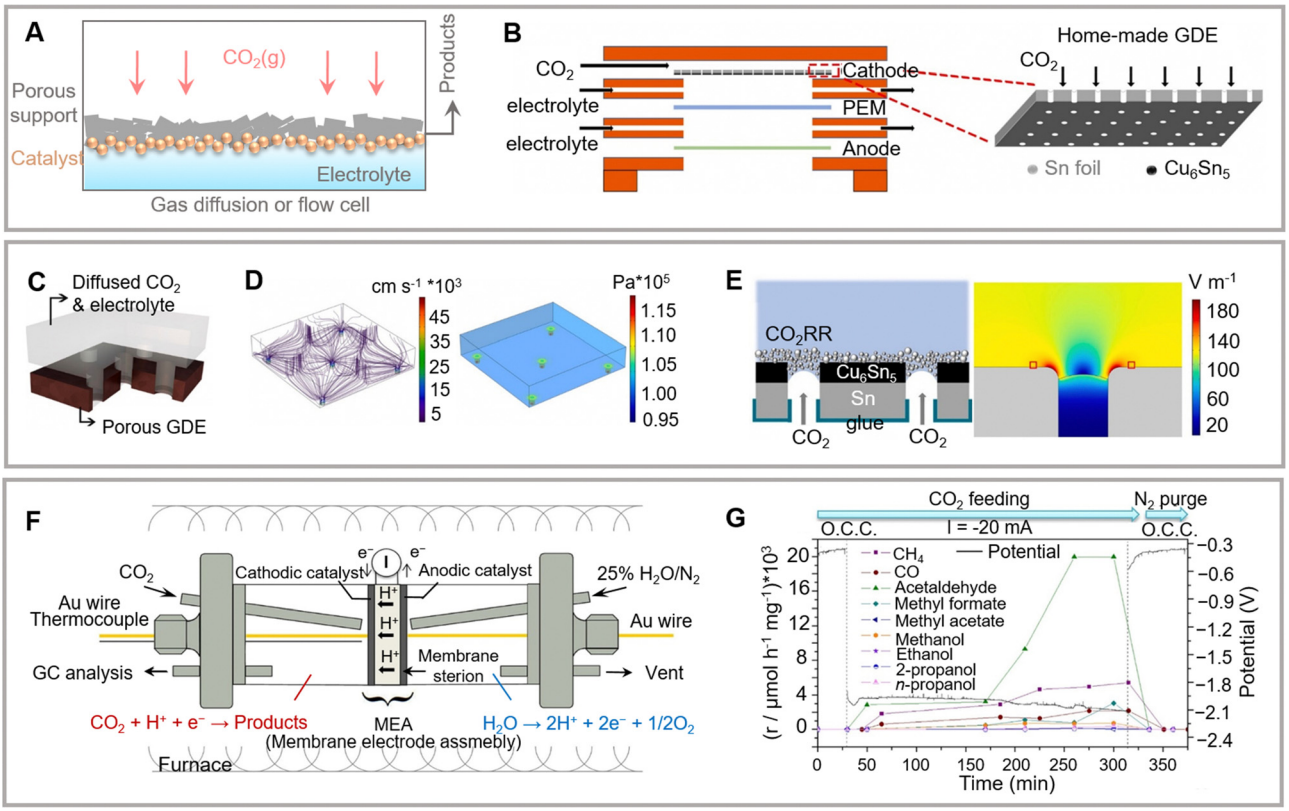

Fig. 12 (A) Schematic illustration of the triphasic electrocatalysis system. (B) Schematic diagram of the flow cell and gas diffusion layer-based electrolyzer (GDE). (C) 3D schematic of porous GDE diffused CO_2 and the electrolyte. (D) Simulation results of the velocity and pressure field of diffused CO_2 in the 3D model. (E) 2D schematic of the liquid–gas interface and the corresponding electric field distributions. Reproduced with permission from Zhou *et al.*[310] Copyright 2022 Elsevier. (F) Schematic illustration of the eCO_2RR reactor. (G) Time-on-stream variation of different products and applied potential. Reproduced with permission from Lucas-Consuegra *et al.*[312] Copyright 2016 Elsevier.

Based on this study, Sargent and colleagues have further optimized a novel ionomer heterojunction structure.[288] The decoupling of gas, ion, and electron transmission enables the effective electrolysis of CO_2 in the gas phase to produce C_{2+} products at a high current density (>1 A cm^{-2}). The ionomer heterojunction comprises a copper nanoparticle catalyst layer and a perfluorosulfonic acid ionomer layer. A 3D morphology has been formed with metal and ionomer permeation pathways. This structure is both hydrophilic and hydrophobic. The separate transmission of gas, ions, and electrons increased gas diffusion and transmission paths. Herein, the elevated current density and significantly improved reaction efficiency enable a maximum ethylene yield of 65–75%. Although the catalyst is the core of electrocatalysis, a GDL-based catalytic reaction system featuring a gas–solid–liquid triphasic interface can also play an influential role by improving the GDL and increasing the concentration of reactants around the catalyst.[32,289–291]

Various liquid electrolytes (such as salt solutions, ionic liquids, *etc.*) have been utilized in different CO_2RR electrolyzers for C_{2+} synthesis. The drawback of these catalytic systems is that the resulting liquid products are mixed with the electrolyte liquid phase, leading to significant energy consumption during the subsequent separation process. The introduction of solid polymer electrolytes or porous solid ion conductors can theoretically solve the above issues. The water gas hydrophobic layer formed at the gas–solid interface can not only kinetically limit the dissociation of H_2O to suppress HER but also stabilize the formation of CO_2 reaction intermediates to facilitate the formation of C_{2+} products through a relay catalysis model. The successful construction of solid-state electrolytes has the following advantages: optimization of the three-phase interface reaction environment, reduction of the ohmic loss of the entire device, avoidance of corrosion and electrolyte consumption issues, and solution of the product separation problems.

5.2.2. Ion exchange membrane. The emerging eCO_2RR membrane electrode assembly (MEA) electrolyzers (or zero-gap reactors) contain a cathode and anode pressed tightly on both sides of the ion-exchange membrane, which effectively facilitates the mass transfer and promotes the activation of continuously delivered gaseous CO_2 at the membrane/cathode interface.[292,293] The eCO_2RR electrolyzers involving anion exchange membranes (AEMs) have attracted extensive research attention. Positively charged functional groups on the polymer chain of the AEM facilitate anion transport from the cathode to the anode, enabling the CO_2RR to occur in a basic environment.[294–296] The basic environment decreases the thermodynamic driving force for the competing hydrogen evolution reaction by decreasing the concentration of H^+ at the

membrane/cathode interface. However, significant operational challenges still have been encountered during the design and optimization of AEMs.

First, the crossover of products and reactants is a prominent issue. However, AEMs can alleviate cathode flooding and improve CO_2RR performance.[297] Negatively charged CO_2RR products are easily transported through the positively charged AEM, while neutral products (such as ethanol) can crossover the membrane. Another operational issue is the mechanical and chemical stability of commercial AEMs. The discovery of novel AEMs has been realized with the recent developments of polymers. Polystyrene tetramethyl imidazolium chloride (PSTMIM), commercialized as Sustainion, is an AEM designed for gas-fed CO_2RR electrolyzers in neutral solutions. This thin hydrophilic membrane features elevated OH^- conductivity and ion exchange capacity. Such outstanding properties of Sustainion ensure 93% faradaic efficiency of the CO_2RR electrolyzer at the practical current of 350 mA cm^{-2} for 40 h.[298] However, Sustainion is prone to CO_2RR products' crossover, particularly at the high current densities relevant to commercial operation. Furthermore, quaternary ammonium poly(*N*-methyl-piperidine-*co*-pterphenyl) (QAPPT) has been introduced as another candidate material for AEM construction.[299–301] QAPPT exhibits better chemical stability than Sustainion in high pH solutions or at elevated temperatures (>80 °C). The high conductivity of QAPPT eliminates the need to humidify the CO_2 feed or use ionic anode electrolytes. With an operating temperature of 60 °C, the CO_2RR electrolyzer involving QAPPT demonstrated a high current density with an FE of 90% and a cell voltage of 3 V. These results motivate further research on incorporating Sustainion, QAPPT or other novel AEMs for utilization in C_{2+} producing systems.

The chemical stability, ionic conductivity, size and mechanical stability of the AEM directly determine the performance and lifetime of CO_2RR electrolyzers. The main issues with the AEM are chemical stability and low ion conductivity. For example, in an anion exchange membrane, the ion conductivity of OH^- in water is much lower than that of H^+. Some strategies have been developed accordingly to boost the chemical stability and ion conductivity. Polystyrene and its perfluorinated polymer, as well as polybenzimidazole polymers with excellent mechanical properties, can be introduced to construct semi-interpenetrating network membranes to improve chemical stability. Meanwhile, the membrane with one-chain multiple functional groups can be designed to promote the conductivity of the membrane with C–H-based main chain of poly(styrene-ethylene-butene). Another issue that should not be ignored in the membrane structure optimization process is the thickness of the AEM, which should be specially adjusted to achieve synchronous enhancement of stability and conductivity.

5.2.3. Importance of interfacial mass transfer. A study of H-type cells has observed that the catalytic activity (intrinsic and extrinsic activity related to mass transfer) is significantly boosted with the increase of catalyst porosity. Similar to that of H-type cells, the reaction interface of the gas diffusion layer-based electrolyzer (GDE) determines the activity and selectivity of eCO_2RR.[302] The study aims to understand and optimize the effect of CO_2 mass transfer on the efficiency and selectivity at the triphasic interface. Compared with the two-phase catalysis, CO_2 can directly reach the catalyst surface in the triphasic interface by passing through the GDL layer without the liquid phase diffusion. In addition, much research has also been focused on rapid product desorption after the completion of the reduction reaction, which is quite essential for the whole catalytic process.

The mass transfer of *CO is still crucial for tuning eCO_2RR activity and selectivity. The operating current density and target product selectivity are highly dependent on the CO_2 flow rate, CO_2 partial pressure, or even the thickness of the catalyst layer. When using the GDL, the thickness of the mass transfer boundary layer decreases from 60–160 μm in the H-type cell to 0.01–10 μm in the GDE, and the current density is significantly improved.[303,304] The local pH value is enhanced at high current densities to inhibit methane formation and promote C_{2+} product selectivity. Furthermore, high CO_2 conversion rates can be realized using low CO_2 flow rates. The optimal flow rate should exceed ten sccm for optimal C_{2+} product formation at current densities of 100–150 mA cm^{-2}.[305] The partial pressure of CO_2 favors the selective formation of C_2H_4 rather than CO. Moreover, the 250 nm-thick layer is more selective than the 50 nm-thick layer, suggesting that the optimized thickness enhances C–C coupling.[306] Owing to the increase of OH^- concentration, the dipole interaction becomes stronger, and the binding of *CO has been improved. In addition, the increased *CO mass transfer and *CO dimer stability promote the C_{2+} selectivity.[307,308]

Sargent and colleagues have calculated the GDL thickness using parameters such as bubble separation diameter, pressure, fluid velocity, and current density. The bubble separation diameter depends on the catalyst surface morphology and wettability.[309] By comparing the influence of nanowires, nanorods, and nanoparticle catalysts on the bubble separation diameter, the authors have found that tiny bubbles generated by nanowires produce a smaller diffusion layer thickness and promote the interfacial mass transfer of CO_2. Thus, the electrode morphology is concluded to influence the long-distance transportation of CO_2 profoundly. Zhou and colleagues employed a laser to prepare channels on a Cu_6Sn_5 alloy electrode as a GDE and applied it in a flow cell to obtain a high eCO_2RR FE and catalytic stability (Fig. 12B).[310] The distributions of CO_2 concentration and an electric field near the electrode are simulated using COMSOL Multiphysics. A high CO_2 concentration and a strong electric field around the electrode surface favor the occurrence of eCO_2RR (Fig. 12C and D). In addition, Kelvin probe force microscopy has been utilized to measure the actual electric field distribution around the channel, and the results are consistent with simulation data (Fig. 12E). Zhang and colleagues have explored the conditions and influencing factors of CO_2 mass transfer by changing the wetting characteristics of a typical GDE surface.[311] Interfacial structure plays a crucial role in stabilizing CO_2 concentration during eCO_2RR. The Cassie–Wenzel coexistence state is an

ideal triphasic structure with continuous CO_2 supply on active sites at a high current density. This study provides the mechanism of the triphasic electrocatalytic reactions of other gaseous substances. However, more understanding of the actual mass transfer at the micro-interface is required. Therefore, more in-depth mechanistic research and accurate and intuitive *in situ*/*operando* characterization methods are essential to overcome the limitations of CO_2 interfacial mass transfer.

Kenis and colleagues have successfully designed a microfluidic CO_2 cell system using a GDE with a thin (1 mm) channel. Compared to MEA systems, the supplied CO_2 diffused through the porous GDL to naturally form an electrolyte–catalyst–gas triphasic interface even in the absence of water vapor (Fig. 12F).[312] The eCO_2RR can occur at the boundary between the catalyst and the cathode liquid. The reactor is not sensitive to the ion transfer rate and can achieve a high current density (Fig. 12G).[306] It is essential to introduce a membrane between the electrolyte channels to achieve the separation and anti-reoxidation of liquid C_{2+} products on the anode side. Over the past few years, various electrolytic cells have been developed using shared high-performance catalysts.[313] Presently, the volatilization of gas products and the shuttling of liquid products across multiple flow cells remain challenging.[314] In addition, research on catalyst–electrolyte interface tuning (*e.g.*, the development of different ion-exchange membranes, optimization of electrode surface/interface structures, and innovation in electrolytic cell design) requires further exploration.

5.2.4. Reaction system design. The critical components of the CO_2RR cell are the structure of the GDL, catalyst layer, and membrane. In addition to the great progress that has been achieved in catalyst designing, the innovation in electrolyzer designing also provides practical approaches to manipulate the reaction rate and selectivity. The traditional H-type electrolytic cell immerses the cathode in the electrolyte and realizes the catalytic CO_2 conversion by applying the reduction potential. The CO_2 molecules dissolved in the electrolyte are adsorbed on the catalyst surface and undergo the three-phase CO_2RR reaction. Due to the limited solubility of CO_2 in an aqueous solution (0.033 mol L^{-1}) under normal temperature and pressure, the CO_2RR activity is primarily limited by mass transfer. The current density in the H-type electrolytic cell is limited to 20 mA cm^{-2}, which is not commercially feasible (250 mA cm^{-2}).[315] Furthermore, H-type cell has a large volume and elevated cell pressure, which is not favorable for large-scale application. Applying a GDE in continuous flow cells shortens the gas diffusion distance and promotes mass transfer. The compact structure promotes the industrial CO_2RR application of the flow cell. Herein, this section summarizes and analyzes the structure of the flow cell and the degradation mechanism of various components and electrolyzers to provide novel ideas for optimizing and improving the CO_2RR flow cell.

In the traditional flow cell, the gas–liquid cathode chambers of the hydrophobic GDE are relatively well separated.[286,316,317] The cathode is exposed to the feed gas to realize the coexistence of the liquid and gas phases in the catalyst layer, while CO_2RR occurs at this triphasic boundary of the GDE (Fig. 13A). This structure can promote mass transfer and significantly improve the stability of CO_2RR in alkaline electrolytes at industrial-grade current density. For the catalyst layer, the optimized catalyst material powder is generally loaded onto the GDE by brush coating, air spraying, or ion sputtering technology.[318,319] The composition and proportion of solvent, the selection of binders, and the coating method of the catalyst may all affect the performance of electrolyzers. For the microporous layer, the appropriate microporous layer can achieve gas–liquid two-phase separation (especially in the microfluidic device) and prevent electrode flooding.[286,320] The smooth and tight microporous layer decreases the contact resistance between the catalyst layer and the carbon substrate and prevents the catalyst from entering the microporous or substrate layer. The PTFE in the microporous layer affects the porosity, conductivity, and water distribution of the electrode.[321] Kim and colleagues have introduced a thin liquid pH buffer layer between the cathode GDE and the ion exchange membrane to further improve the CO_2RR selectivity.[322] The microfluidic flow cell with a PTFE content of 20% achieves low charge transfer resistance and enhanced performance (Fig. 13B). Moreover, the hydrophobicity of the carbon substrate also influences the performance of the electrolyzer. Park and colleagues have constructed a microfluidic flow cell with different hydrophobic carbon substrates. The current and selectivity are finally optimized by tuning the hydrophobicity.[323] This microfluidic structure is shown in Fig. 12C. By coordinating gas and liquid flow rates to prevent gas diffusion or electrode flooding, the pressure balance can be well tuned. The gas at the anode side can be directly diffused into the air without sealing treatment. The electrolyte solution flows through an extremely tiny channel. The narrow electrode spacing reduces the ohmic polarization loss of the microfluidic cell. Based on the above examples, suitable GDE structures can promote CO_2 electroreduction for their fast mass transfer or high stability. Despite the tremendous progress made with GDEs and liquid flow-cell electrolyzers, numerous problems still need to be well addressed for scalable applications, such as gas diffusion electrode flooding, salt precipitation, reduction product purification, and single-path conversion of CO_2.

Compared with liquid flow-cell electrolyzers, the gas phase MEA electrolyzer laminates the gas diffusion layer, ion exchange membrane, and catalysts into one unit (Fig. 12D). In a continuous flow MEA cell, the anodic catalyst and the cathodic GDE are directly assembled on both sides of the ion-exchange membrane with lower ohmic resistance, further leading to excellent CO_2RR efficiency.[111,306,324] The direct contact between the catalyst layer and the ion exchange membrane can significantly reduce the resistance and improve the stability of the catalytic system. During the operation, there is no flowing electrolyte in the gas phase MEA, and the CO_2 sampling methods are as follows: humidified carbon dioxide with anode electrolyte, humidified anode gas or anode open without any gas or electrolyte; dry carbon dioxide with humidified anode gas or pure water.[325–327] This cathode electrolyte-free property efficiently alleviates the problem of carbonate deposition.[328,329] Meanwhile, accurate flow cell design with the circular or

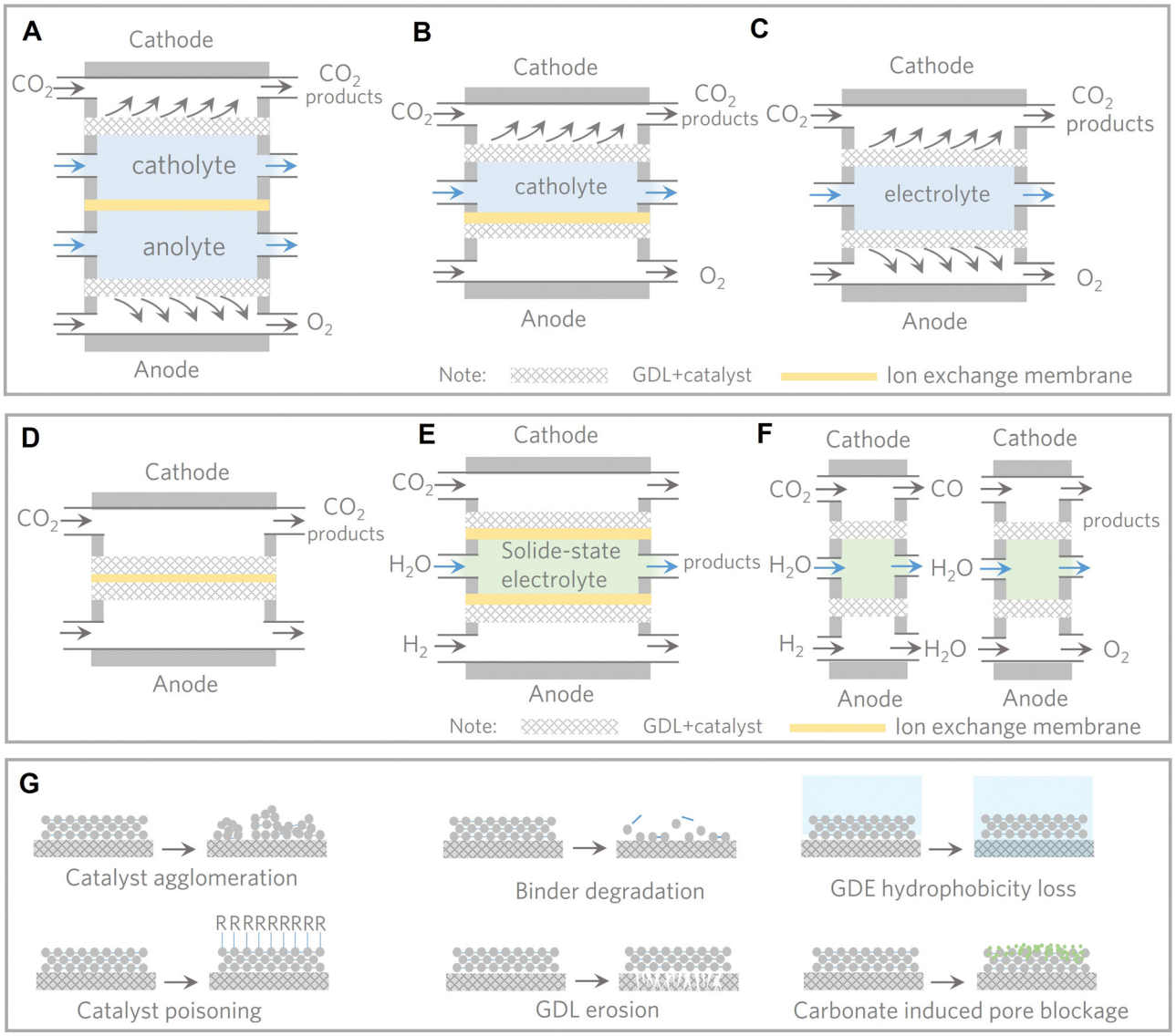

Fig. 13 Schematic of the typical electrochemical flow cells for CO_2 reduction. (A) Traditional flow cell; (B) flow cell with a thin liquid layer; (C) microfluidic cell; (D) gas phase membrane electrode assembly cell; (E) all-solid-state cell; (F) two-step tandem cell. (G) Schematic of degradation mechanisms.

serpentine channel has proven significant in developing MEA cells with efficient reactant delivery. Berlinguette and colleagues have assembled a commercial molecular CoPc electrocatalyst in MEA with the serpentine channel, where the cathode side is fed with wet CO_2 gas flow while the anode is immersed in the KOH solution.[330] A current density of 150 mA cm^{-2} can be well maintained during a long-term operation time of more than 100 h, which adequately illustrates the advantages of the MEA cell in terms of high current density and stability.

The all-solid-state electrolyzer has been developed to collect pure liquid C_{2+} products.[331,332] The solid electrolyte cell employs a central solid electrolyte between anion-exchange and cation-exchange membranes (Fig. 13E). Membrane optimization is one of the crucial ways to improve mass transfer in the solid-state electrolyzer. Asadi and colleagues have employed a Dioxide Materials Sustainion™ anion exchange membrane in a solid electrolyte cell.[333] The CO_2RR performance is improved for more than 700 h at a current of 420 mA cm^{-2}. Furthermore, the porous solid electrolyte of solid-state electrolyzers has also been investigated. Unlike conventional liquid electrolytes, the porous solid electrolyte layer facilitates ion conduction without introducing impurity ions. Wang and colleagues have designed a novel CO_2 reduction cell with a solid electrolyte, which is capable of collecting pure C_{2+} liquid solution.[334] Different forms of solid electrolytes, such as ceramics, polymer/ceramic hybrids, or solidified gel, can also be employed for C_{2+} synthesis in the future.

The single-pass conversion of CO_2 to carbon-based products is a crucial indicator for practical applications. This index remains low (~50%) for an alkaline electrolyte environment,

where locally generated hydroxide anions accelerate carbonate formation at the electrode–electrolyte interface. Tandem processes (including tandem electrocatalysts and electrolyzers) are potential options for efficient CO_2 utilization, which will significantly increase the yield and FE of C_{2+} products. The current works mainly focus on the cathode for different tandem electrode and electrolyzer designs.[335,336] Tandem and resistive sandwich structures have been designed for the electrodes. Several attractive tandem devices have been developed for electrolyzers to increase CO_2 solubility and achieve high CO_2/CO conversion for further C_{2+} product synthesis (Fig. 13F). Despite the exciting progress of tandem electrolyzers, it is vital to note that studies on the anodic reactions still need to be completed, which are necessary for a complete system.

For flow cells, CO_2 crossover has gradually become a significant challenge to improving CO_2RR performance. In neutral or alkaline solutions, the carbonate crossover and precipitation induce low single-pass conversion efficiency and limited device lifetimes. Recent research has shifted towards acidic electrolytes to avoid carbonate, although circumventing the HER becomes a severe challenge. Sargent and colleagues have reported one representative example of interfacial engineering in proton exchange membrane MEA. The concentrated potassium ions at the catalyst–membrane interface primarily improve CO_2RR performance and mitigate the CO_2 crossover.[211] Furthermore, Hu and colleagues have achieved efficient CO_2RR in an acidic medium by suppressing the predominant HER using alkali cations and uncovered the essential role of the balance between carbonate formation rates and H^+ diffusion.[337,338] Hydrated alkali cations physiosorbed on the cathode modify the electric field distribution in the double layer. It impedes HER by suppressing hydronium ion migration, thus promoting CO_2RR by stabilization of critical intermediates. Considering the restriction of CO_2 crossover to the anode side, Kim and colleagues have reported a porous solid electrolyte reactor to recover the carbon losses efficiently. A permeable and ion-conducting sulfonated polymer electrolyte has been constructed as a buffer layer between the cathode and the anode. The crossed over carbonate can combine with protons to reform CO_2 gas for reuse. Future studies can focus on optimizing the porous solid electrolyte reactor for practical CO_2 recovery, including optimizing the thickness of the solid electrolyte layer and improving ion conduction by designing different solid ion conductors.

Furthermore, the investigation of different degradation mechanisms is vital to improving the stability of flow cells. A continuous supply of electrolytes and CO_2 is required to ensure the cell operation in the kinetically limited state rather than the mass-transfer-limited state.[339,340] The most common GDE degradation mechanism is shown in Fig. 13G, mainly including electrode degradation and electrolyte-related degradation. Physical changes in the catalyst structure, such as agglomeration or pulverization of catalyst particles, induce the coverage or loss of available active sites in the catalyst layer. This physical change is irreversible. However, chemical changes are reversible through specific mitigation strategies. The catalytic active site on the surface is covered by adsorbed metal impurities, thus inducing catalyst poisoning. Purifying electrolytes can eliminate the above problems.[341] Einaga and colleagues have applied a positive potential to re-oxidize the material and desorb the adsorbed species.[342,343] Meanwhile, the binders holding the catalyst layers may also suffer various forms of chemical degradation during prolonged exposure to electrolytes and CO_2. The following are the main degradation mechanisms of GDL components: compression-force effects, dissolution, gas flow erosion, and carbon corrosion.[344] The GDE flooding may be caused by macroscopic pressure imbalances in microfluidic devices, electrode hydrophobicity disruption, carbonate deposition, *etc.* After the GDE is flooded, the HER side reaction is more likely to occur with the decrease of the FE of C_{2+} product synthesis. Furthermore, some components of the electrolyzer may also be oxidized. The carbon material of the anode flow channel may be oxidized and decomposed. It is worth noting that no evident corrosion phenomenon is observed using titanium as the flow channel.[345] To sum up, the design and optimization of electrolytic cell components to suppress the above degradation is an essential prerequisite for improving stability for industrial applications in the future.

Currently the most commonly used microflow cell is a three-chamber configuration, which can effectively prevent cathodic liquid products from being oxidized in the anode. Since the liquid electrolyte layer allows the use of a reference electrode, the microflow electrolytic cell can accurately control the cathode potential. However, the main factor limiting the performance of this configuration is the stability of the gas–liquid–solid three-phase interface on the GDE surface. Once the balanced three-phase interface is disrupted, excessive electrolytes penetrate the GDE channel and water flooding occurs. Mass transfer will be severely inhibited, and the reaction rate will significantly decrease. MEA cells, especially for the anion exchange membrane-based MEA cells, have been developed in which the direct contact between the GDE and the ion exchange membrane is realized, which may largely resolve the above-mentioned issues. However, carboxylic acid anionic products can also migrate to the anode through the anion exchange membrane, causing product loss and separation difficulties. In addition, the poor stability of the anion exchange membrane leads to a shorter operating life of this configuration, which limits its further application. The bipolar membrane-based MEA cells can significantly improve the conversion rate of CO_2 and suppress the carbonate concentration on the electrode surface. The challenge lies in the fact that high concentrations of hydrogen ions on the electrode surface may promote the occurrence of the side HER reaction. Moreover, bipolar membrane configurations often require higher voltage and lower energy efficiency compared to other configurations. Research can be conducted in the following areas based on the advantages, disadvantages, and challenges of the above-mentioned electrolytic cells. The selection and amount of binder and embedded ionomers directly affect the stability of the catalyst layer and the operational life of the reactor. The

most direct approach for GDE structural optimization is tuning feeding parameters, including the selection of the feeding method, gas humidification, degree of humidification, and flow rate optimization. In addition, the preparation of the carbon fiber substrate (hydrophobicity, thickness, *etc.*), adjusting the PTFE loading or adding a porous membrane layer can improve the hydrophobicity of the diffusion electrode. For practical application, exploring the failure and repair mechanism of electrolytic cells is conducive to realizing long-term stability tests under high currents, scaling up CO_2 flow cells (including individual electrolyzers and stacks of multiple electrolyzer units). A reasonable flow channel design of the electrode plate should ensure uniform fluid distribution and maintain a low voltage drop.

5.2.5. eCO$_2$RR with industry-compatible current. eCO$_2$RR is an effective approach for CO_2 resource utilization to realize the worldwide ''carbon neutralization'' strategy. Economic and technical analyses have revealed that commercial profit can be achieved with a total current density of >300 mA cm^{-2}, an FE of $>90\%$, and an energy conversion efficiency of $>70\%$. In addition, the long-term stability of electrocatalytic reaction is required to be at least hundreds of hours to realize industrial eCO$_2$RR.[346,347] High selectivity and high yield should be achieved at commercial current densities.[348,349] However, the agglomeration, phase transition, and element dissolution result in a rapid decrease in the C_{2+} product selectivity during high-rate electrocatalysis. Therefore, to achieve industrial eCO$_2$RR to obtain C_{2+} products, it is urgent to design eCO$_2$RR catalysts with ultra-high activity, selectivity, and stability, and effective eCO$_2$RR reactors.

Several studies have revealed that alkaline conditions are conducive to the formation of C_{2+} products. CO_2 tends to form carbonate under strongly alkaline conditions. Sargent and colleagues have achieved the electrocatalytic production of ethylene from CO_2 *via* a composite electrode under 10 M KOH (strong base conditions), with a stable FE of 70% (at 750 mA cm^{-2}).[111] First a 25 nm-thick copper nanocatalyst has been sputtered on a porous polytetrafluoroethylene film with an aperture of approximately 220 nm. Subsequently, a carbon nanoparticle layer has been sprayed on the catalyst layer as a conductive layer. Lastly, a graphite nanoparticle layer has been added as the base of the collector and the entire structure. This electrode structure exhibits the following advantages: (1) the PTFE porous diffusion protective layer reduces the diffusion rate of CO_2 to ensure the reduction of CO_2 before the side reaction with the strong alkaline electrolyte occurs. In alkaline electrolytes, the competitive HER reaction rate also decreases, which further improves the selectivity of the electrocatalytic reduction to olefin. (2) As a large amount of CO_2 has been reduced before contacting OH^-, the surface of the copper catalyst can absorb a large amount of OH^-, which reduces the activation energy barrier of CO–CO coupling and further enhances ethylene selectivity. (3) The PTFE porous diffusion protective layer significantly improves the stability of copper nanocatalysts and can operate stably for 150 h under test conditions.

Subsequently, Sargent and colleagues have also proposed a method for designing a hybrid catalyst. By decoupling the gas, ion, and electron transmission, CO_2 can be effectively electrolyzed to generate C_2 products in the gas phase electrolysis at current densities of >1 A cm^{-2}.[288] An ionomer layer with hydrophobic and hydrophilic functions facilitates the transport of gases and ions across metal surfaces. Thus, the reaction interface of these three components (gaseous reactants, ions, and electrons) has been located at the catalytic active site, thus increasing in length from the submicron range to several microns. Perfluorinated sulfonic acid (PFSA) ions with hydrophobic and hydrophilic functions have attracted significant attention. PFSA ions exhibit a high dependency on their structure/function. Based on the excellent advantages of the triphasic reaction, a novel catalyst has been designed to utilize gas–electrolyte separation beyond that of 2D catalysts. Typically, this catalyst with a maximized triphasic interface enables the system to operate efficiently at a higher current. The 3D catalyst has been prepared on a PTFE/Cu/ionomer (CIPH) gas diffusion layer support. With an increase in the loading and the corresponding thickness, the total eCO$_2$RR current increases monotonously, exceeding 1 A cm^{-2} at a low load of 3.33 mg cm^{-2}. When the load is higher, saturation is reached, and the current density significantly increases, after which the energy efficiency decreases. Under the top current operating condition, the maximum ethylene yield of the optimized catalyst is 65–75%, and the peak off-current density reaches up to 1.34 A cm^{-2} with a high cathode energy efficiency (46.3%). At 1.1 A cm^{-2} without iR compensation, the energy efficiency of C_{2+} products in the full electrolytic cell has been estimated to be 20%. However, current research still needs to be improved, such as the separation of C_{2+} products, the economic feasibility of the process, stability, and selectivity under industry-compatible current.

To summarize, the prominent challenges facing the commercialization of electrochemical CO_2RR technology are energy efficiency, selectivity, low current density, and stability. For industrial applications, the current density should be higher than 300 mA cm^{-2} with FE above 80%, cell voltage below 1.8 V and stability over 80 000 hours (Fig. 14). The biggest challenge currently faced is low energy efficiency and CO_2 utilization efficiency. As a heterogeneous catalysis electrochemical process, it is anticipated that increasing the total catalyst surface area in the reactor or increasing the intrinsic reaction rate should be conducive to boosting the chemical productivity, which is undoubtedly necessary for scaling up and long-term reactor design. To break through the above challenges, the FE of the C_{2+} product synthesis system should be further enhanced, while the overvoltage of the electrolytic cell should be kept at a low level. Meanwhile, another influencing factor for CO_2RR commercialization is the duration of stable operation. The minimum stable operation time required for profit scale expansion should exceed 10 000 hours at least. The lifetime of cells mainly depends on the key components of the electrodes (or MEAs), including the form of the electrocatalyst, the regulation of functional groups in the polymer membrane, the selection of

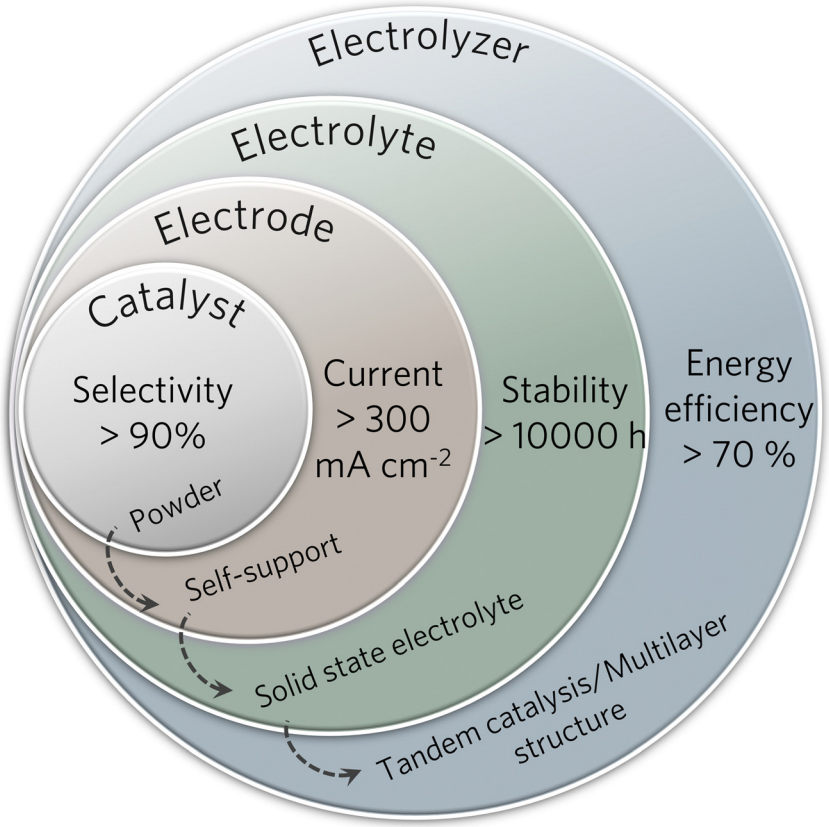

Fig. 14 Scheme of the challenges involved in a CO_2RR system toward high-performance commercialization.

polymer binders, optimization of GDLs, and configuration type (tandem catalytic system or multilayer system).

6. Summary and outlook

Significant progress has been made during the past few decades regarding the design of highly active or selective electrocatalysts and their eCO_2RR mechanism. In this review, we have summarized the fundamental principles for catalyst design and provided a comprehensive overview of the catalytic mechanism, which covers almost all aspects of this emerging field with a perspective on C_{2+} synthesis. There is no doubt that eCO_2RR is a promising approach for realizing the carbon cycle balance and addressing the current clean energy crisis simultaneously soon. On the other hand, we should be aware that there are still many challenges in the exploration and practical application of the electrochemical conversion of CO_2 into C_{2+} products. We summarize the following perspectives and possible resolutions to address the current challenges in the electrochemical CO_2 conversion into C_{2+} products.

6.1. Novel catalyst discovery

Designing and regulating the intrinsic catalytic activity of advanced nanocatalysts are essential. The electronic structure of the catalyst surface can be adjusted by controlling the crystal facets, defects, and surface stress. Thus, the adsorption energy of *CO, *CHO, and other primary intermediates can be changed to break the scaling relationship and achieve high C_{2+} product selectivity. Meanwhile, the C_{2+} product synthesis is closely related to the coverage and concentration of *CO intermediates. Several catalysts with high CO selectivity have been reported (such as Au, Ag, and Zn). Therefore, $CO_2 \rightarrow CO \rightarrow C_{2+}$ tandem catalysis *via* multi-metal cooperation is another practical approach. In this approach, the CO_2 feed gas is first reduced to CO on the surface of the second component metal, after which it overflows to the adjacent metal interface for C–C coupling and further reduction. In this strategy, the high CO coverage on the catalyst surface is conducive to inhibiting side reactions and promoting C_{2+} product preparation.

Single-atom catalysis is a hot topic in the field of energy conversion. However, the large distance between the active centers of single atoms complicates the effective promotion of C–C coupling. C_{2+} product formation may be enhanced by increasing the surface density of homogeneously dispersed active sites. Moreover, catalysts for C–C coupling are not limited to metal-based catalysts. Several metal-free carbon-based materials have also been demonstrated to exhibit potential eCO_2RR activity for C_{2+} products (such as graphene quantum dots and metal-doped nanodiamonds).

Furthermore, new opportunities have emerged in traditional molecular catalysts in recent years. Heterogeneous immobilization

is an effective solution for addressing the problems of low solubility, low utilization, and difficult recovery of molecular catalysts. In this approach, the catalyst molecules are fixed to specific carriers as electrode materials through specific interactions (such as covalent bonds, electrostatic forces, and π–π interactions).

6.2. Profound computational approaches exploration

The complex C_{2+} reaction pathway in theoretical research illustrates the inherent complexity of pathways, the sensitivity of intermediates, and the controversy related to the pH effect. Presently, experimental evidence cannot obtain reaction information from catalyst–intermediate interactions at the atomic or even electronic level. Theoretical calculations can effectively remedy the above deficiencies. The theoretical calculations can be utilized to investigate the transformation of critical intermediates, the structural evolution of reaction centers, and the ion and electrolyte effects. However, at present the application of theoretical simulations in exploring C_{2+} synthesis mechanisms still faces several challenges. The electrolyte–electrode interface treatment is the critical issue. It is time-consuming to construct the explicit solvent model with numerous water molecules, whereas the implicit model may lose hydrogen bonds or other interactions of intermediates. Moreover, the constant charge model with a changeable Fermi level needs to be improved with the charge transfer between electrode and catalysts. It is necessary to take the solvent effect into consideration to better simulate the electrostatic interactions of the electric double layer in the working environment.

Furthermore, based on theoretical calculations, the combination of machine learning can accelerate the prediction and screening of better eCO_2RR electrocatalysts. By optimizing a machine learning model, a high-throughput calculation can be performed on the critical data of the electronic structure of catalytic materials. Future research on machine learning may focus on the following aspects to address some of the most important constraints of eCO_2RR. (a) Current machine learning methods are rather limited in mechanism research and the prediction of C_{2+} products. The key characteristics should be investigated, and appropriate models for exploring the optimal reaction pathway for C_{2+} products should be explored. (b) The combination of machine learning calculations and advanced *in situ*/*operando* characterization exhibits significant potential for designing novel catalysts and elucidating the eCO_2RR mechanism. (c) Combined with the solvent effect mechanism, screening suitable solvents through machine learning has broad prospects for developing high-performance eCO_2RR systems.

6.3. Original *in situ*/*operando* technique development

eCO_2RR possesses abundant products and complex reaction pathways, and the catalyst structure may change during the reaction process. The application of *in situ*/*operando* characterization techniques in eCO_2RR is highly desirable to establish a more precise ''structure–performance'' relationship by exploring the interactions between substrate molecules, intermediates, and catalytic active sites. Despite impressive progress in *in situ*/*operando* characterization, there are still many problems to be solved in this field. Given the limited catalytic information provided by an individual *in situ*/*operando* technique, different *in situ*/*operando* tests need to be performed on the same *in situ*/*operando* reactor to simultaneously detect the catalyst structure change and the evolution of intermediates. In addition, the signal intensities of several *in situ*/*operando* techniques still require improvement owing to the low coverage of the key reaction intermediates. Such experimental results obtained at the same time and space scales by tightly coupling multiple *in situ*/*operando* representations are more convincing for exploring eCO_2RR mechanisms. Another major challenge of *in situ*/*operando* experiments is the optimal design of *in situ*/*operando* electrolytic cells. To conform to the harsh conditions of *in situ*/*operando* testing, the electrolytic cell undergoes targeted structural changes, which results in a mismatch between the *in situ*/*operando* testing conditions and the actual working conditions. Therefore, it is urgent to develop optimized electrolytic cells to truly bridge the gap between *in situ*/*operando* testing and actual working conditions and to obtain effective information that fully reflects the real catalytic eCO_2RR. Moreover, the close integration of machine learning, *in situ*/*operando* experiments, and theoretical calculations is a practical approach to exploring reaction thermodynamics/kinetics and pathways.

6.4. Electrolyte and electrode optimization

Although materials are the key to eCO_2RR, the catalytic performance is also affected by other factors, such as the chemical composition of electrolytes and structural design of the electrodes. The optimization of selectivity and corresponding mechanism analysis can be achieved by tuning the cation size and concentration. Meanwhile, ionic liquids have also been proven to be suitable media for CO_2 dissolution, activation, and stabilization of free radicals and electrochemically active ionic substances from aqueous solutions. Unlike conventional electrolytes, most anisotropic ionic liquids display properties of an extended cooperative network of supramolecular species. The future challenges mainly include (1) the influence mechanism of cations/anions on surface groups and material stability; (2) the relationship between the structure and organization of ionic liquids and the eCO_2RR.

Focusing on the electrolyte system and addressing the above challenges, the following research will be focused on in the future. (1) The influence mechanism of the ionic liquid electrolyte structure on eCO_2RR needs to be clarified. The reduction law between the ionic liquid structure and eCO_2RR activity can be thoroughly understood by the cooperation of theoretical simulations and *in situ*/*operando* characterization techniques. Furthermore, it is necessary to clarify the synergistic mechanism between the proton/electron transfer process in an ionic liquid system and the interface structure of catalytic materials. (2) An ionic liquid electrolyte system for synthesizing C_{2+} products needs to be developed to activate CO_2 molecules and facilitate the functionalization of C–C coupling in the intermediate states of the reaction. (3) It is urgent to study

the flow mass transfer and stability of CO_2 reduction in ionic liquid systems. The internal structure, electrode structure, and electrolyte flow type of eCO_2RR devices with different structures must be optimized to promote the C_{2+} activity and selectivity. (4) The CO_2 crossover issue should be resolved. Future studies can focus on designing porous solid electrolyte reactors for practical CO_2 recovery, including optimizing the thickness of the solid electrolyte layer for minimized ohmic drop and improving ion conduction between the cathode and the anode by designing different solid ion conductors.

As mentioned above, the selectivity and the yield of C_{2+} products can be further improved by the rational design of catalytic electrodes and devices. The utilization of the GDE has helped to bridge the gap between laboratory experimental findings and industrial needs. However, achieving long-term stability with such high selectivity and activity remains a significant challenge. At the macro level, eCO_2RR activity can be enhanced by simple process-strengthening techniques, such as increasing the partial pressure of CO_2 and forced electrolyte flow. At the micro level, it is urgent to develop the technology to realize process enhancement with the help of the GDE microporous structure and hydrophilic and hydrophobic adjustment. The main research direction of the cathode microstructure is to expand and form a stable three-phase interface. Furthermore, the selectivity for specific C_{2+} products should also be optimized to reduce the cost of product separation and purification. Thus, further research is needed to investigate and explore effective methods for improving reactant concentrations around active sites and the turnover and selectivity of adsorbed intermediates at high current densities. It is urgent to design high-throughput reactors with economic reactant capture technologies to increase industrial production potential.

Conflicts of interest

There are no conflicts to declare.

Acknowledgements

This work is supported by the King Abdullah University of Science and Technology (KAUST).

References

1 Z. H. Xue, D. Y. Luan, H. B. Zhang and X. W. Lou, *Joule*, 2022, **6**, 92–133.
2 X. Wu, H. B. Zhang, J. Zhang and X. W. Lou, *Adv. Mater.*, 2021, **33**, 2008376.
3 C. Feng, Z. P. Wu, K. W. Huang, J. H. Ye and H. B. Zhang, *Adv. Mater.*, 2022, **34**, 2200180.
4 M. G. Lee, X.-Y. Li, A. Ozden, J. Wicks, P. Ou, Y. Li, R. Dorakhan, J. Lee, H. K. Park, J. W. Yang, B. Chen, J. Abed, R. dos Reis, G. Lee, J. E. Huang, T. Peng, Y.-H. Chin, D. Sinton and E. H. Sargent, *Natl. Catal.*, 2023, **6**, 310–318.
5 W. H. Huang, C. Y. Su, C. Zhu, T. T. Bo, S. W. Zuo, W. Zhou, Y. F. Ren, Y. N. Zhang, J. Zhang, M. Rueping and H. B. Zhang, *Angew. Chem., Int. Ed.*, 2023, **135**, e202304634.
6 J. Du, B. Cheng, H. Yuan, Y. Tao, Y. Chen, M. Ming, Z. Han and R. Eisenberg, *Angew. Chem., Int. Ed.*, 2023, **62**, e202211804.
7 W. Ahmad, P. Koley, S. Dwivedi, R. Lakshman, Y. K. Shin, A. C. T. van Duin, A. Shrotri and A. Tanksale, *Nat. Commun.*, 2023, **14**, 2821.
8 H. W. Lin, S. Q. Luo, H. B. Zhang and J. H. Ye, *Joule*, 2022, **6**, 294–314.
9 H. B. Zhang, W. R. Cheng, D. Y. Luan and X. W. Lou, *Angew. Chem., Int. Ed.*, 2021, **60**, 13177–13196.
10 Y. Xie, P. Ou, X. Wang, Z. Xu, Y. C. Li, Z. Wang, J. E. Huang, J. Wicks, C. McCallum, N. Wang, Y. Wang, T. Chen, B. T. W. Lo, D. Sinton, J. C. Yu, Y. Wang and E. H. Sargent, *Natl. Catal.*, 2022, **5**, 564–570.
11 S. D. Rihm, M. K. Kovalev, A. A. Lapkin, J. W. Ager and M. Kraft, *Energy Environ. Sci.*, 2023, **16**, 1697–1710.
12 X. F. Zhang, W. H. Huang, L. Yu, M. García-Melchor, D. S. Wang, L. J. Zhi and H. B. Zhang, *Carbon Energy*, 2023, e362.
13 Y. J. Shi, Y. J. Wang, J. Y. Yu, Y. K. Chen, C. Q. Fang, D. Jiang, Q. H. Zhang, L. Gu, X. W. Yu, X. Li, H. Liu and W. J. Zhou, *Adv. Energy Mater.*, 2023, **13**, 2203506.
14 W. Lai, Y. Qiao, J. Zhang, Z. Lin and H. Huang, *Energy Environ. Sci.*, 2022, **15**, 3603–3629.
15 Y. Zhu, P. Li, X. Yang, M. Wang, Y. Zhang, P. Gao, Q. Huang, Y. Wei, X. Yang, D. Wang, Y. Shen and M. Wang, *Adv. Energy Mater.*, 2023, **13**, 2204243.
16 J. Li, K. Xu, F. Liu, Y. Li, Y. Hu, X. Chen, H. Wang, W. Xu, Y. Ni, G. Ding, T. Zhao, M. Yu, W. Xie and F. Cheng, *Adv. Mater.*, 2023, e2301127.
17 J. Qin, T. Wang, M. Zhai, C. Wu, Y. A. Liu, B. Yang, H. Yang, K. Wen and W. Hu, *Adv. Funct. Mater.*, 2023, 2300697.
18 L. Fan, C.-Y. Liu, P. Zhu, C. Xia, X. Zhang, Z.-Y. Wu, Y. Lu, T. P. Senftle and H. Wang, *Joule*, 2022, **6**, 205–220.
19 E. Fujita, D. C. Grills, G. F. Manbeck and D. E. Polyansky, *Acc. Chem. Res.*, 2022, **55**, 616–628.
20 Z. Zhang, J. Zhu, S. Chen, W. Sun and D. Wang, *Angew. Chem., Int. Ed.*, 2023, **62**, e202215136.
21 Z. Li, Y. Gao, X. Meng, B. Sun, K. Song, Z. Wang, Y. Liu, Z. Zheng, P. Wang, Y. Dai, H. Cheng and B. Huang, *Cell Rep. Phys. Sci.*, 2022, **3**, 100972.
22 M. Esmaeilirad, A. Kondori, N. Shan, M. T. Saray, S. Sarkar, A. M. Harzandi, C. M. Megaridis, R. Shahbazian-Yassar, L. A. Curtiss, C. U. Segre and M. Asadi, *Appl. Catal., B*, 2022, **317**, 121681.
23 F. Dattila, R. R. Seemakurthi, Y. Zhou and N. Lopez, *Chem. Rev.*, 2022, **122**, 11085–11130.
24 C. Han, V. Kundi, Z. Ma, C. Y. Toe, P. Kumar, C. Tsounis, J. Jiang, S. Xi, Z. Han, X. Lu, R. Amal and J. Pan, *Adv. Funct. Mater.*, 2023, **33**, 2210938.
25 S. H. Li, S. Hu, H. Liu, J. Liu, X. Kang, S. Ge, Z. Zhang, Q. Yu and B. Liu, *ACS Nano*, 2023, **17**, 9338–9346.
26 Z. Ma, T. Wan, D. Zhang, J. A. Yuwono, C. Tsounis, J. Jiang, Y. H. Chou, X. Lu, P. V. Kumar, Y. H. Ng, D. Chu, C. Y. Toe, Z. Han and R. Amal, *ACS Nano*, 2023, **17**, 2387–2398.

27 D. Giusi, M. Miceli, C. Genovese, G. Centi, S. Perathoner and C. Ampelli, *Appl. Catal., B*, 2022, **318**, 121845.
28 Y. Zou and S. Wang, *Adv. Sci.*, 2021, **8**, 2003579.
29 Q. S. Wang, Y. C. Yuan, C. F. Li, Z. R. Zhang, C. Xia, W. G. Pan and R. T. Guo, *Small*, 2023, e2301892.
30 K. Xiang, F. Shen, Y. Fu, L. Wu, Z. Wang, H. Yi, X. Liu, P. Wang, M. Liu, Z. Lin and H. Liu, *Environ. Sci.: Nano*, 2022, **9**, 911–953.
31 W. Liu, P. Zhai, A. Li, B. Wei, K. Si, Y. Wei, X. Wang, G. Zhu, Q. Chen, X. Gu, R. Zhang, W. Zhou and Y. Gong, *Nat. Commun.*, 2022, **13**, 1877.
32 W. X. Nie, G. P. Heim, N. B. Watkins, T. Agapie and J. C. Peters, *Angew. Chem., Int. Ed.*, 2023, **135**, e202216102.
33 Z. Lin, Z. Jiang, Y. Yuan, H. Li, H. Wang, Y. Tang, C. Liu and Y. Liang, *Chin. J. Catal.*, 2022, **43**, 104–109.
34 W. Ma, X. He, W. Wang, S. Xie, Q. Zhang and Y. Wang, *Chem. Soc. Rev.*, 2021, **50**, 12897–12914.
35 T. H. M. Pham, J. Zhang, M. Li, T. H. Shen, Y. Ko, V. Tileli, W. Luo and A. Züttel, *Adv. Energy Mater.*, 2022, **12**, 2103663.
36 L. L. Zhuo, P. Chen, K. Zheng, X. W. Zhang, J. X. Wu, D. Y. Lin, S. Y. Liu, Z. S. Wang, J. Y. Liu, D. D. Zhou and J. P. Zhang, *Angew. Chem., Int. Ed.*, 2022, **61**, e202204967.
37 Z. Gu, H. Shen, Z. Chen, Y. Yang, C. Yang, Y. Ji, Y. Wang, C. Zhu, J. Liu, J. Li, T.-K. Sham, X. Xu and G. Zheng, *Joule*, 2021, **5**, 429–440.
38 S. Nitopi, E. Bertheussen, S. B. Scott, X. Liu, A. K. Engstfeld, S. Horch, B. Seger, I. E. L. Stephens, K. Chan, C. Hahn, J. K. Norskov, T. F. Jaramillo and I. Chorkendorff, *Chem. Rev.*, 2019, **119**, 7610–7672.
39 G. Wang, J. Chen, Y. Ding, P. Cai, L. Yi, Y. Li, C. Tu, Y. Hou, Z. Wen and L. Dai, *Chem. Soc. Rev.*, 2021, **50**, 4993–5061.
40 J. Schneider, H. Jia, J. T. Muckerman and E. Fujita, *Chem. Soc. Rev.*, 2012, **41**, 2036–2051.
41 Z. Han, D. Han, Z. Chen, J. Gao, G. Jiang, X. Wang, S. Lyu, Y. Guo, C. Geng, L. Yin, Z. Weng and Q. H. Yang, *Nat. Commun.*, 2022, **13**, 3158.
42 X. Lv, Q. Liu, J. Wang, X. Wu, X. Li, Y. Yang, J. Yan, A. Wu and H. B. Wu, *Appl. Catal., B*, 2023, **324**, 122272.
43 Z. Wei, J. Ding, X. Duan, G.-L. Chen, F.-Y. Wu, L. Zhang, X. Yang, Q. Zhang, Q. He, Z. Chen, J. Huang, S.-F. Hung, X. Yang and Y. Zhai, *ACS Catal.*, 2023, **13**, 4711–4718.
44 R. B. Sandberg, J. H. Montoya, K. Chan and J. K. Nørskov, *Surf. Sci.*, 2016, **654**, 56–62.
45 Y. Liang, J. Zhao, Y. Yang, S. F. Hung, J. Li, S. Zhang, Y. Zhao, A. Zhang, C. Wang, D. Appadoo, L. Zhang, Z. Geng, F. Li and J. Zeng, *Nat. Commun.*, 2023, **14**, 474.
46 J. Zhang, C. Guo, S. Fang, X. Zhao, L. Li, H. Jiang, Z. Liu, Z. Fan, W. Xu, J. Xiao and M. Zhong, *Nat. Commun.*, 2023, **14**, 1298.
47 T. Zhang, B. Yuan, W. Wang, J. He and X. Xiang, *Angew. Chem., Int. Ed.*, 2023, **135**, e202302096.
48 C. Kim, L.-C. Weng and A. T. Bell, *ACS Catal.*, 2020, **10**, 12403–12413.
49 P. Wang, H. Yang, C. Tang, Y. Wu, Y. Zheng, T. Cheng, K. Davey, X. Huang and S. Z. Qiao, *Nat. Commun.*, 2022, **13**, 3754.
50 J. Yin, Z. Yin, J. Jin, M. Sun, B. Huang, H. Lin, Z. Ma, M. Muzzio, M. Shen, C. Yu, H. Zhang, Y. Peng, P. Xi, C. H. Yan and S. Sun, *J. Am. Chem. Soc.*, 2021, **143**, 15335–15343.
51 K. U. D. Calvinho, A. W. Alherz, K. M. K. Yap, A. B. Laursen, S. Hwang, Z. J. L. Bare, Z. Clifford, C. B. Musgrave and G. C. Dismukes, *J. Am. Chem. Soc.*, 2021, **143**, 21275–21285.
52 P. Chen, Y. Wu, T. E. Rufford, L. Wang, G. Wang and Z. Wang, *Mater. Today Chem.*, 2023, **27**, 101328.
53 C. Li, Y. Ji, Y. Wang, C. Liu, Z. Chen, J. Tang, Y. Hong, X. Li, T. Zheng, Q. Jiang and C. Xia, *Nano-Micro Lett.*, 2023, **15**, 113.
54 P. Wei, D. Gao, T. Liu, H. Li, J. Sang, C. Wang, R. Cai, G. Wang and X. Bao, *Nat. Nanotechnol.*, 2023, **18**, 299–306.
55 F. Chang, Y. Liu, J. Wei, L. Yang and Z. Bai, *Inorg. Chem. Front.*, 2023, **10**, 240–249.
56 M. Wang, V. Nikolaou, A. Loiudice, I. D. Sharp, A. Llobet and R. Buonsanti, *Chem. Sci.*, 2022, **13**, 12673–12680.
57 Y. R. Lin, D. U. Lee, S. Tan, D. M. Koshy, T. Y. Lin, L. Wang, D. Corral, J. E. Avilés Acosta, J. A. Zamora Zeledon, V. A. Beck, S. E. Baker, E. B. Duoss, C. Hahn and T. F. Jaramillo, *Adv. Funct. Mater.*, 2022, **32**, 2113252.
58 R. De, S. Gonglach, S. Paul, M. Haas, S. S. Sreejith, P. Gerschel, U. P. Apfel, T. H. Vuong, J. Rabeah, S. Roy and W. Schofberger, *Angew. Chem., Int. Ed.*, 2020, **59**, 10527–10534.
59 X. F. Qiu, J. R. Huang, C. Yu, Z. H. Zhao, H. L. Zhu, Z. Ke, P. Q. Liao and X. M. Chen, *Angew. Chem., Int. Ed.*, 2022, **61**, e202206470.
60 J. B. Pang, B. Chang, H. Liu and W. J. Zhou, *ACS Energy Lett.*, 2022, **7**, 78–96.
61 C. E. Creissen and M. Fontecave, *Nat. Commun.*, 2022, **13**, 2280.
62 Z. Zhang, S. Chen, J. Zhu, C. Ye, Y. Mao, B. Wang, G. Zhou, L. Mai, Z. Wang, X. Liu and D. Wang, *Nano Lett.*, 2023, **23**, 2312–2320.
63 K. Rossi and R. Buonsanti, *Acc. Chem. Res.*, 2022, **55**, 629–637.
64 H. Zhang, W. Zhou, X. F. Lu, T. Chen and X. W. Lou, *Adv. Energy Mater.*, 2020, **10**, 2000882.
65 X. Wu, H. Zhang, S. Zuo, J. Dong, Y. Li, J. Zhang and Y. Han, *Nano-Micro Lett.*, 2021, **13**, 136.
66 K. Lakshmanan, W. H. Huang, S. A. Chala, B. W. Taklu, E. A. Moges, J. F. Lee, P. Y. Huang, Y. C. Lee, M. C. Tsai, W. N. Su and B. J. Hwang, *Adv. Funct. Mater.*, 2022, **32**, 2109310.
67 X. Li, J. Wang, X. Lv, Y. Yang, Y. Xu, Q. Liu and H. B. Wu, *Nano-Micro Lett.*, 2022, **14**, 134.
68 A. R. Woldu, Z. Huang, P. Zhao, L. Hu and D. Astruc, *Coord. Chem. Rev.*, 2022, **454**, 214340.
69 Y. Kim, S. Park, S.-J. Shin, W. Choi, B. K. Min, H. Kim, W. Kim and Y. J. Hwang, *Energy Environ. Sci.*, 2020, **13**, 4301–4311.
70 K. Zhao, X. Nie, H. Wang, S. Chen, X. Quan, H. Yu, W. Choi, G. Zhang, B. Kim and J. G. Chen, *Nat. Commun.*, 2020, **11**, 2455.

71 D. Ren, J. Gao, L. Pan, Z. Wang, J. Luo, S. M. Zakeeruddin, A. Hagfeldt and M. Gratzel, *Angew. Chem., Int. Ed.*, 2019, **58**, 15036–15040.
72 X. Wang, J. F. de Araujo, W. Ju, A. Bagger, H. Schmies, S. Kuhl, J. Rossmeisl and P. Strasser, *Nat. Nanotechnol.*, 2019, **14**, 1063–1070.
73 X. Wu, H. Zhang, J. Zhang and X. W. D. Lou, *Adv. Mater.*, 2021, **33**, e2008376.
74 A. J. Garza, A. T. Bell and M. Head-Gordon, *ACS Catal.*, 2018, **8**, 1490–1499.
75 S. Kim, D. Shin, J. Park, J. Y. Jung and H. Song, *Adv. Sci.*, 2023, **10**, e2207187.
76 W. Ma, S. Xie, T. Liu, Q. Fan, J. Ye, F. Sun, Z. Jiang, Q. Zhang, J. Cheng and Y. Wang, *Natl. Catal.*, 2020, **3**, 478–487.
77 M. Zhong, K. Tran, Y. Min, C. Wang, Z. Wang, C. T. Dinh, P. De Luna, Z. Yu, A. S. Rasouli, P. Brodersen, S. Sun, O. Voznyy, C. S. Tan, M. Askerka, F. Che, M. Liu, A. Seifitokaldani, Y. Pang, S. C. Lo, A. Ip, Z. Ulissi and E. H. Sargent, *Nature*, 2020, **581**, 178–183.
78 X. Nie, M. R. Esopi, M. J. Janik and A. Asthagiri, *Angew. Chem., Int. Ed.*, 2013, **125**, 2519–2522.
79 Y. T. Guntern, V. Okatenko, J. Pankhurst, S. B. Varandili, P. Iyengar, C. Koolen, D. Stoian, J. Vavra and R. Buonsanti, *ACS Catal.*, 2021, **11**, 1248–1295.
80 H. Lin, K. Wei, Z. Yin and S. Sun, *iScience*, 2021, **24**, 102172.
81 J. J. Lv, R. Yin, L. Zhou, J. Li, R. Kikas, T. Xu, Z. J. Wang, H. Jin, X. Wang and S. Wang, *Angew. Chem., Int. Ed.*, 2022, **134**, e202207252.
82 Z. Z. Wu, X. L. Zhang, Z. Z. Niu, F. Y. Gao, P. P. Yang, L. P. Chi, L. Shi, W. S. Wei, R. Liu, Z. Chen, S. Hu, X. Zheng and M. R. Gao, *J. Am. Chem. Soc.*, 2022, **144**, 259–269.
83 C. Obasanjo, A. Shayesteh Zeraati, H. S. Shiran, T. N. Nguyen, M. G. Kibria, S. M. Sadaf and C. T. Dinh, *J. Mater. Chem. A*, 2022, **10**, 20059–20070.
84 G. O. Larrazabal, V. Okatenko, I. Chorkendorff, R. Buonsanti and B. Seger, *ACS Appl. Mater. Interfaces*, 2022, **14**, 7779–7787.
85 W. Zhang, C. Huang, Q. Xiao, L. Yu, L. Shuai, P. An, J. Zhang, M. Qiu, Z. Ren and Y. Yu, *J. Am. Chem. Soc.*, 2020, **142**, 11417–11427.
86 D. Tan, B. Wulan, X. Cao and J. Zhang, *Nano Energy*, 2021, **89**, 106460.
87 Y. Pan, H. Li, J. Xiong, Y. Yu, H. Du, S. Li, Z. Wu, S. Li, J. Lai and L. Wang, *Appl. Catal., B*, 2022, **306**, 121111.
88 C. E. Creissen and M. Fontecave, *Nat. Commun.*, 2022, **13**, 2280.
89 Q. Sun, C. Jia, Y. Zhao and C. Zhao, *Chin. J. Catal.*, 2022, **43**, 1547–1597.
90 H. Xu, D. Rebollar, H. He, L. Chong, Y. Liu, C. Liu, C.-J. Sun, T. Li, J. V. Muntean, R. E. Winans, D.-J. Liu and T. Xu, *Nat. Energy*, 2020, **5**, 623–632.
91 Z. Gu, N. Yang, P. Han, M. Kuang, B. Mei, Z. Jiang, J. Zhong, L. Li and G. Zheng, *Small Methods*, 2019, **3**, 1800449.
92 C. Peng, G. Luo, J. Zhang, M. Chen, Z. Wang, T. K. Sham, L. Zhang, Y. Li and G. Zheng, *Nat. Commun.*, 2021, **12**, 1580.
93 Q. Li, Y.-C. Wang, J. Zeng, X. Zhao, C. Chen, Q.-M. Wu, L.-M. Chen, Z.-Y. Chen and Y.-P. Lei, *Rare Met.*, 2021, **40**, 3442–3453.
94 F.-Y. Gao, Z.-Z. Wu and M.-R. Gao, *Energy Fuels*, 2021, **35**, 12869–12883.
95 Y. Sun, G. Li, W. Sun and X. Zhou, *J. CO2 Util.*, 2023, **67**, 102344.
96 Y. Wang, P. Han, X. Lv, L. Zhang and G. Zheng, *Joule*, 2018, **2**, 2551–2582.
97 J. Wang, C. Cheng, B. Huang, J. Cao, L. Li, Q. Shao, L. Zhang and X. Huang, *Nano Lett.*, 2021, **21**, 980–987.
98 Z. Ma, C. Tsounis, C. Y. Toe, P. V. Kumar, B. Subhash, S. Xi, H. Y. Yang, S. Zhou, Z. Lin, K.-H. Wu, R. J. Wong, L. Thomsen, N. M. Bedford, X. Lu, Y. H. Ng, Z. Han and R. Amal, *ACS Catal.*, 2022, **12**, 4792–4805.
99 D. Tan, B. Wulan, J. Ma, X. Cao and J. Zhang, *Chem. Catal.*, 2023, **3**, 100512.
100 H. Shen, Y. Zhao, L. Zhang, Y. He, S. Yang, T. Wang, Y. Cao, Y. Guo, Q. Zhang and H. Zhang, *Adv. Energy Mater.*, 2022, **13**, 2202818.
101 Q. Ren, N. Zhang, Z. Dong, L. Zhang, X. Chen and L. Luo, *Nano Energy*, 2023, **106**, 108080.
102 Y. Jiang, X. Wang, D. Duan, C. He, J. Ma, W. Zhang, H. Liu, R. Long, Z. Li, T. Kong, X. J. Loh, L. Song, E. Ye and Y. Xiong, *Adv. Sci.*, 2022, **9**, e2105292.
103 Y. Du and W. An, *J. Phys. Chem. C*, 2021, **125**, 9138–9149.
104 J. Wang, H. Y. Tan, Y. Zhu, H. Chu and H. M. Chen, *Angew. Chem., Int. Ed.*, 2021, **133**, 17394–17407.
105 D. Song, Y. B. Lian, M. Wang, Y. H. Su, F. L. Lyu, Z. Deng and Y. Peng, *eScience*, 2023, **3**, 100097.
106 Q. Zhu, C. J. Murphy and L. R. Baker, *J. Am. Chem. Soc.*, 2022, **144**, 2829–2840.
107 S. Yu, D. Kim, Z. Qi, S. Louisia, Y. Li, G. A. Somorjai and P. Yang, *J. Am. Chem. Soc.*, 2021, **143**, 19919–19927.
108 A. Thevenon, A. Rosas-Hernandez, J. C. Peters and T. Agapie, *Angew. Chem., Int. Ed.*, 2019, **58**, 16952–16958.
109 Y. Li, F. Cui, M. B. Ross, D. Kim, Y. Sun and P. Yang, *Nano Lett.*, 2017, **17**, 1312–1317.
110 J. Yuan, M.-P. Yang, W.-Y. Zhi, H. Wang, H. Wang and J.-X. Lu, *J. CO2 Util.*, 2019, **33**, 452–460.
111 C. T. Dinh, T. Burdyny, M. G. Kibria, A. Seifitokaldani, C. M. Gabardo, F. P. Garcia de Arquer, A. Kiani, J. P. Edwards, P. De Luna, O. S. Bushuyev, C. Zou, R. Quintero-Bermudez, Y. Pang, D. Sinton and E. H. Sargent, *Science*, 2018, **360**, 783–787.
112 L. Li, X. Li, Y. Sun and Y. Xie, *Chem. Soc. Rev.*, 2022, **51**, 1234–1252.
113 T. Tang, Z. Wang and J. Guan, *Adv. Funct. Mater.*, 2022, **32**, 2111504.
114 H. Li, Y. Pan, Z. Wang, Y. Yu, J. Xiong, H. Du, J. Lai, L. Wang and S. Feng, *Nano Res.*, 2021, **15**, 3056–3064.
115 H. Dong, M. Lu, Y. Wang, H.-L. Tang, D. Wu, X. Sun and F.-M. Zhang, *Appl. Catal., B*, 2022, **303**, 120897.

116 K. A. Adegoke and N. W. Maxakato, *Mater. Today Chem.*, 2022, **24**, 100838.
117 Q. Lu, C. Chen, Q. Di, W. Liu, X. Sun, Y. Tuo, Y. Zhou, Y. Pan, X. Feng, L. Li, D. Chen and J. Zhang, *ACS Catal.*, 2022, **12**, 1364–1374.
118 J. Zhou, B. An, Z. Zhu, L. Wang and J. Zhang, *Inorg. Chem.*, 2022, **61**, 6073–6082.
119 W. Pei, S. Zhou, J. Zhao, X. Xu, Y. Du and S. X. Dou, *Nano Energy*, 2020, **76**, 105049.
120 M. K. Lee, M. Shokouhimehr, S. Y. Kim and H. W. Jang, *Adv. Energy Mater.*, 2021, **12**, 2003990.
121 H. Xiao, W. A. Goddard, 3rd, T. Cheng and Y. Liu, *Proc. Natl. Acad. Sci. U. S. A.*, 2017, **114**, 6685–6688.
122 M. Suominen and T. Kallio, *ChemElectroChem*, 2021, **8**, 2397–2406.
123 X. Li, Q. Liu, J. Wang, D. Meng, Y. Shu, X. Lv, B. Zhao, H. Yang, T. Cheng, Q. Gao, L. Li and H. B. Wu, *Chem*, 2022, **8**, 2148–2162.
124 F. Yu, Z. Zhou, Y. You, J. Zhan, T. Yao and L. H. Zhang, *ACS Appl. Mater. Interfaces*, 2023, **15**, 24346–24353.
125 N. Li, X. Chen, W. J. Ong, D. R. MacFarlane, X. Zhao, A. K. Cheetham and C. Sun, *ACS Nano*, 2017, **11**, 10825–10833.
126 M. Abdinejad, S. Subramanian, M. K. Motlagh, M. Noroozifar, S. Duangdangchote, I. Neporozhnii, D. Ripepi, D. Pinto, M. Li, K. Tang, J. Middelkoop, A. Urakawa, O. Voznyy, H. B. Kraatz and T. Burdyny, *Adv. Energy Mater.*, 2023, **13**, 2300402.
127 W. Xiong, D. Si, J. Yi, Y. Huang, H. Li and R. Cao, *Appl. Catal., B*, 2022, **314**, 121498.
128 D. H. Nam, O. Shekhah, G. Lee, A. Mallick, H. Jiang, F. Li, B. Chen, J. Wicks, M. Eddaoudi and E. H. Sargent, *J. Am. Chem. Soc.*, 2020, **142**, 21513–21521.
129 S. Lin, C. S. Diercks, Y. B. Zhang, N. Kornienko, E. M. Nichols, Y. Zhao, A. R. Paris, D. Kim, P. Yang, O. M. Yaghi and C. J. Chang, *Science*, 2015, **349**, 1208–1213.
130 C. Chen, X. Yan, Y. Wu, S. Liu, X. Zhang, X. Sun, Q. Zhu, H. Wu and B. Han, *Angew. Chem., Int. Ed.*, 2022, **61**, e202202607.
131 X. Xie, X. Zhang, M. Xie, L. Xiong, H. Sun, Y. Lu, Q. Mu, M. H. Rummeli, J. Xu, S. Li, J. Zhong, Z. Deng, B. Ma, T. Cheng, W. A. Goddard, 3rd and Y. Peng, *Nat. Commun.*, 2022, **13**, 63.
132 C. F. Wen, M. Zhou, P. F. Liu, Y. Liu, X. Wu, F. Mao, S. Dai, B. Xu, X. L. Wang, Z. Jiang, P. Hu, S. Yang, H. F. Wang and H. G. Yang, *Angew. Chem., Int. Ed.*, 2022, **61**, e202111700.
133 L. Cheng, P. Zhang, Q. Wen, J. Fan and Q. Xiang, *Chin. J. Catal.*, 2022, **43**, 451–460.
134 Y. Jia, F. Li, K. Fan and L. Sun, *Adv. Powder Mater.*, 2022, **1**, 100012.
135 L. Wan, X. Zhang, J. Cheng, R. Chen, L. Wu, J. Shi and J. Luo, *ACS Catal.*, 2022, **12**, 2741–2748.
136 W. Lai, Z. Ma, J. Zhang, Y. Yuan, Y. Qiao and H. Huang, *Adv. Funct. Mater.*, 2022, **32**, 2111193.
137 Y. Xie, P. Ou, X. Wang, Z. Xu, Y. C. Li, Z. Wang, J. E. Huang, J. Wicks, C. McCallum, N. Wang, Y. Wang, T. Chen, B. T. W. Lo, D. Sinton, J. C. Yu, Y. Wang and E. H. Sargent, *Natl. Catal.*, 2022, **5**, 564–570.
138 S. Ma, M. Sadakiyo, M. Heima, R. Luo, R. T. Haasch, J. I. Gold, M. Yamauchi and P. J. Kenis, *J. Am. Chem. Soc.*, 2017, **139**, 47–50.
139 P. Wang, H. Yang, C. Tang, Y. Wu, Y. Zheng, T. Cheng, K. Davey, X. Huang and S. Z. Qiao, *Nat. Commun.*, 2022, **13**, 3754.
140 C. G. Morales-Guio, E. R. Cave, S. A. Nitopi, J. T. Feaster, L. Wang, K. P. Kuhl, A. Jackson, N. C. Johnson, D. N. Abram, T. Hatsukade, C. Hahn and T. F. Jaramillo, *Natl. Catal.*, 2018, **1**, 764–771.
141 K. U. D. Calvinho, A. B. Laursen, K. M. K. Yap, T. A. Goetjen, S. Hwang, N. Murali, B. Mejia-Sosa, A. Lubarski, K. M. Teeluck, E. S. Hall, E. Garfunkel, M. Greenblatt and G. C. Dismukes, *Energy Environ. Sci.*, 2018, **11**, 2550–2559.
142 M. Qu, Z. Chen, Z. Sun, D. Zhou, W. Xu, H. Tang, H. Gu, T. Liang, P. Hu, G. Li, Y. Wang, Z. Chen, T. Wang and B. Jia, *Nano Res.*, 2022, **16**, 2170–2176.
143 J. Meng, Z. Miao, J. Zhang, Z. Wang, R. Zhang, L. Xu, L. Diao, J. Zhou and S. Zhuo, *J. Alloys Compd.*, 2023, **939**, 168798.
144 Y. Zhou, A. J. Martín, F. Dattila, S. Xi, N. López, J. Pérez-Ramírez and B. S. Yeo, *Natl. Catal.*, 2022, **5**, 545–554.
145 J. Du, B. Cheng, L. Jiang and Z. Han, *Chem. Commun.*, 2023, **59**, 4778–4781.
146 Y. Fang, X. Liu, Z. Liu, L. Han, J. Ai, G. Zhao, O. Terasaki, C. Cui, J. Yang, C. Liu, Z. Zhou, L. Chen and S. Che, *Chem*, 2023, **9**, 460–471.
147 N. C. Ramos, J. W. Medlin and A. Holewinski, *ACS Appl. Mater. Interfaces*, 2023, **15**, 14470.
148 F. Dattila, R. R. Seemakurthi, Y. Zhou and N. Lopez, *Chem. Rev.*, 2022, **122**, 11085–11130.
149 N. Karmodak, S. Vijay, G. Kastlunger and K. Chan, *ACS Catal.*, 2022, **12**, 4818–4824.
150 J. Santatiwongchai, K. Faungnawakij and P. Hirunsit, *ACS Catal.*, 2021, **11**, 9688–9701.
151 Y. A. Alsunni, A. W. Alherz and C. B. Musgrave, *J. Phys. Chem. C*, 2021, **125**, 23773–23783.
152 S. Xu and E. A. Carter, *Chem. Rev.*, 2019, **119**, 6631–6669.
153 Y. Guan, W. Suo, Z. Zhang, Y. Wang, S. Sun and G. Liu, *Mol. Catal.*, 2021, **511**, 111725.
154 M. G. Kibria, J. P. Edwards, C. M. Gabardo, C. T. Dinh, A. Seifitokaldani, D. Sinton and E. H. Sargent, *Adv. Mater.*, 2019, **31**, e1807166.
155 J. D. Goodpaster, A. T. Bell and M. Head-Gordon, *J. Phys. Chem. Lett.*, 2016, **7**, 1471–1477.
156 F. Grun, M. Jardat, P. Turq and C. Amatore, *J. Chem. Phys.*, 2004, **120**, 9648–9655.
157 M. F. Kling and M. J. Vrakking, *Annu. Rev. Phys. Chem.*, 2008, **59**, 463–492.
158 S. Ali, G. Yasin, R. Iqbal, X. Huang, J. Su, S. Ibraheem, Z. Zhang, X. Wu, F. Wahid, P. M. Ismail, L. Qiao and H. Xu, *Mol. Catal.*, 2022, **524**, 112285.
159 M. E. Björketun, Z. Zeng, R. Ahmed, V. Tripkovic, K. S. Thygesen and J. Rossmeisl, *Chem. Phys. Lett.*, 2013, **555**, 145–148.

160 L. D. Chen, M. Bajdich, J. M. P. Martirez, C. M. Krauter, J. A. Gauthier, E. A. Carter, A. C. Luntz, K. Chan and J. K. Norskov, *Nat. Commun.*, 2018, **9**, 3202.
161 X. Liu, J. Xiao, H. Peng, X. Hong, K. Chan and J. K. Norskov, *Nat. Commun.*, 2017, **8**, 15438.
162 T. Cheng, H. Xiao and W. A. Goddard, 3rd, *Proc. Natl. Acad. Sci. U. S. A.*, 2017, **114**, 1795–1800.
163 C. Shi, K. Chan, J. S. Yoo and J. K. Nørskov, *Org. Process Res. Dev.*, 2016, **20**, 1424–1430.
164 T. Cheng, H. Xiao and W. A. Goddard, 3rd, *J. Phys. Chem. Lett.*, 2015, **6**, 4767–4773.
165 C.-C. Chang and M.-S. Ku, *J. Phys. Chem. C*, 2021, **125**, 10919–10925.
166 Y. Feng, W. An, Z. Wang, Y. Wang, Y. Men and Y. Du, *ACS Sustainable Chem. Eng.*, 2019, **8**, 210–222.
167 A. Kakekhani, L. T. Roling, A. Kulkarni, A. A. Latimer, H. Abroshan, J. Schumann, H. AlJama, S. Siahrostami, S. Ismail-Beigi, F. Abild-Pedersen and J. K. Norskov, *Inorg. Chem.*, 2018, **57**, 7222–7238.
168 Q. Zhao, J. M. P. Martirez and E. A. Carter, *J. Am. Chem. Soc.*, 2021, **143**, 6152–6164.
169 X. Nie, W. Luo, M. J. Janik and A. Asthagiri, *J. Catal.*, 2014, **312**, 108–122.
170 Y. Tian, T. Zhao, C. Zhao and Y. Likai, *Appl. Surf. Sci.*, 2022, **597**, 153724.
171 M. Wan, Z. Gu and F. Che, *ChemCatChem*, 2021, **14**, e202101224.
172 H. Dong, Y. Li and D.-E. Jiang, *J. Phys. Chem. C*, 2018, **122**, 11392–11398.
173 C. Zhu, Z. Zhang, L. Zhong, C.-S. Hsu, X. Xu, Y. Li, S. Zhao, S. Chen, J. Yu, S. Chen, M. Wu, P. Gao, S. Li, H. M. Chen, K. Liu and L. Zhang, *Chem*, 2021, **7**, 406–420.
174 L. D. Chen, M. Urushihara, K. Chan and J. K. Nørskov, *ACS Catal.*, 2016, **6**, 7133–7139.
175 K. Jiang, R. B. Sandberg, A. J. Akey, X. Liu, D. C. Bell, J. K. Nørskov, K. Chan and H. Wang, *Natl. Catal.*, 2018, **1**, 111–119.
176 H. Xiao, T. Cheng, W. A. Goddard, 3rd and R. Sundararaman, *J. Am. Chem. Soc.*, 2016, **138**, 483–486.
177 F. Calle-Vallejo and M. T. M. Koper, *Angew. Chem., Int. Ed.*, 2013, **125**, 7423–7426.
178 D. Raciti, M. Mao, J. H. Park and C. Wang, *J. Electrochem. Soc.*, 2018, **165**, 799–804.
179 G. Marcandalli, M. C. O. Monteiro, A. Goyal and M. T. M. Koper, *Acc. Chem. Res.*, 2022, **55**, 1900–1911.
180 S. Jin, Z. Hao, K. Zhang, Z. Yan and J. Chen, *Angew. Chem., Int. Ed.*, 2021, **133**, 20795–20816.
181 E. L. Clark, J. Resasco, A. Landers, J. Lin, L.-T. Chung, A. Walton, C. Hahn, T. F. Jaramillo and A. T. Bell, *ACS Catal.*, 2018, **8**, 6560–6570.
182 H. Hashiba, L.-C. Weng, Y. Chen, H. K. Sato, S. Yotsuhashi, C. Xiang and A. Z. Weber, *J. Phys. Chem. C*, 2018, **122**, 3719–3726.
183 M. Dunwell, Q. Lu, J. M. Heyes, J. Rosen, J. G. Chen, Y. Yan, F. Jiao and B. Xu, *J. Am. Chem. Soc.*, 2017, **139**, 3774–3783.
184 K. Li, W. Wang, H. Zheng, X. Wang, Z. Xie, L. Ding, S. Yu, Y. Yao and F. Y. Zhang, *Mater. Today Phys.*, 2021, **19**, 1000427.
185 C. W. Li, J. Ciston and M. W. Kanan, *Nature*, 2014, **508**, 504–507.
186 P. Li, J. Bi, J. Liu, Q. Zhu, C. Chen, X. Sun, J. Zhang and B. Han, *Nat. Commun.*, 2022, **13**, 1965.
187 Y. Zhou, Y. Yao, R. Zhao, X. Wang, Z. Fu, D. Wang, H. Wang, L. Zhao, W. Ni, Z. Yang and Y. M. Yan, *Angew. Chem., Int. Ed.*, 2022, **134**, e202205832.
188 X. Liu, P. Schlexer, J. Xiao, Y. Ji, L. Wang, R. B. Sandberg, M. Tang, K. S. Brown, H. Peng, S. Ringe, C. Hahn, T. F. Jaramillo, J. K. Norskov and K. Chan, *Nat. Commun.*, 2019, **10**, 32.
189 E. Bertheussen, A. Verdaguer-Casadevall, D. Ravasio, J. H. Montoya, D. B. Trimarco, C. Roy, S. Meier, J. Wendland, J. K. Nørskov, I. E. L. Stephens and I. Chorkendorff, *Angew. Chem., Int. Ed.*, 2016, **128**, 1472–1476.
190 N. Abidi and S. N. Steinmann, *Curr. Opin. Electrochem.*, 2022, **33**, 100940.
191 X. Zhang and Z. Zhou, *J. Phys. Chem. C*, 2022, **126**, 3820–3829.
192 C. Xu, X. Zhi, A. Vasileff, D. Wang, B. Jin, Y. Jiao, Y. Zheng and S.-Z. Qiao, *Small Structures*, 2020, **2**, 2000058.
193 W. Lai, Z. Ma, J. Zhang, Y. Yuan, Y. Qiao and H. Huang, *Adv. Funct. Mater.*, 2022, **32**, 2111193.
194 W. Deng, P. Zhang, B. Seger and J. Gong, *Nat. Commun.*, 2022, **13**, 803.
195 L. Wang, S. A. Nitopi, E. Bertheussen, M. Orazov, C. G. Morales-Guio, X. Liu, D. C. Higgins, K. Chan, J. K. Nørskov, C. Hahn and T. F. Jaramillo, *ACS Catal.*, 2018, **8**, 7445–7454.
196 A. Murata and Y. Hori, *Bull. Chem. Soc. Jpn.*, 1991, **64**, 123–127.
197 M. R. Singh, Y. Kwon, Y. Lum, J. W. Ager, 3rd and A. T. Bell, *J. Am. Chem. Soc.*, 2016, **138**, 13006–13012.
198 X. Zhou, H. Liu, B. Y. Xia, K. Ostrikov, Y. Zheng and S. Z. Qiao, *Smart Mater.*, 2022, **3**, 111–129.
199 J. Resasco, L. D. Chen, E. Clark, C. Tsai, C. Hahn, T. F. Jaramillo, K. Chan and A. T. Bell, *J. Am. Chem. Soc.*, 2017, **139**, 11277–11287.
200 J. Wellendorff, K. T. Lundgaard, A. Møgelhøj, V. Petzold, D. D. Landis, J. K. Nørskov, T. Bligaard and K. W. Jacobsen, *Phys. Rev. B*, 2012, **85**, 235149.
201 B. Deng, M. Huang, X. Zhao, S. Mou and F. Dong, *ACS Catal.*, 2021, **12**, 331–362.
202 E. Perez-Gallent, G. Marcandalli, M. C. Figueiredo, F. Calle-Vallejo and M. T. M. Koper, *J. Am. Chem. Soc.*, 2017, **139**, 16412–16419.
203 K. Jiang, Y. Huang, G. Zeng, F. M. Toma, W. A. Goddard and A. T. Bell, *ACS Energy Lett.*, 2020, **5**, 1206–1214.
204 K. Ogura, *J. CO2 Util.*, 2013, **1**, 43–49.
205 S. K. Shaw, A. Berna, J. M. Feliu, R. J. Nichols, T. Jacob and D. J. Schiffrin, *Phys. Chem. Chem. Phys.*, 2011, **13**, 5242–5251.
206 S. Zhang, Q. Fan, R. Xia and T. J. Meyer, *Acc. Chem. Res.*, 2020, **53**, 255–264.

207 D. Gao, F. Scholten and B. Roldan Cuenya, *ACS Catal.*, 2017, **7**, 5112–5120.
208 Y. Huang, C. W. Ong and B. S. Yeo, *ChemSusChem*, 2018, **11**, 3299–3306.
209 M. K. Kim, H. Lee, J. H. Won, W. Sim, S. J. Kang, H. Choi, M. Sharma, H. S. Oh, S. Ringe, Y. Kwon and H. M. Jeong, *Adv. Funct. Mater.*, 2021, **32**, 2107349.
210 S. Banerjee, C. S. Gerke and V. S. Thoi, *Acc. Chem. Res.*, 2022, **55**, 504–515.
211 J. E. Huang, F. Li, A. Ozden, A. Sedighian Rasouli, F. P. Garcia de Arquer, S. Liu, S. Zhang, M. Luo, X. Wang, Y. Lum, Y. Xu, K. Bertens, R. K. Miao, C. T. Dinh, D. Sinton and E. H. Sargent, *Science*, 2021, **372**, 1074–1078.
212 B. Pan, J. Fan, J. Zhang, Y. Luo, C. Shen, C. Wang, Y. Wang and Y. Li, *ACS Energy Lett.*, 2022, **7**, 4224–4231.
213 M. Löffler, P. Khanipour, N. Kulyk, K. J. J. Mayrhofer and I. Katsounaros, *ACS Catal.*, 2020, **10**, 6735–6740.
214 S. Jeong, M. H. Choi, G. S. Jagdale, Y. Zhong, N. P. Siepser, Y. Wang, X. Zhan, L. A. Baker and X. Ye, *J. Am. Chem. Soc.*, 2022, **144**, 12673–12680.
215 Y. Shi, Y. Wang, C. L. Dong, T. T. T. Nga, D. Wei, J. Wang, X. Zhao, M. Wang, K. Zhang, M. Li, F. Dong and S. Shen, *Adv. Energy Mater.*, 2023, **13**, 2203896.
216 L. D. Chen, M. Urushihara, K. Chan and J. K. Nørskov, *ACS Catal.*, 2016, **6**, 7133–7139.
217 H. Cao, Z. Zhang, J.-W. Chen and Y.-G. Wang, *ACS Catal.*, 2022, **12**, 6606–6617.
218 X. Zhang and Z. Zhou, *J. Phys. Chem. C*, 2022, **126**, 3820–3829.
219 X. Qin, T. Vegge and H. A. Hansen, *J. Am. Chem. Soc.*, 2023, **145**, 1897–1905.
220 H. Liu, J. Liu and B. Yang, *ACS Catal.*, 2021, **11**, 12336–12343.
221 K. Chan and J. K. Norskov, *J. Phys. Chem. Lett.*, 2015, **6**, 2663–2668.
222 A. Chen, X. Zhang and Z. Zhou, *InfoMat*, 2020, **2**, 553–576.
223 J. L. Hitt, Y. C. Li, S. Tao, Z. Yan, Y. Gao, S. J. L. Billinge and T. E. Mallouk, *Nat. Commun.*, 2021, **12**, 1114.
224 Z. Yang, W. Gao and Q. Jiang, *J. Mater. Chem. A*, 2020, **8**, 17507–17515.
225 S. Gusarov, S. R. Stoyanov and S. Siahrostami, *J. Phys. Chem. C*, 2020, **124**, 10079–10084.
226 R. Qi, B. Zhu, Z. Han and Y. Gao, *ACS Catal.*, 2022, **12**, 8269–8278.
227 Z. W. Ulissi, A. J. Medford, T. Bligaard and J. K. Norskov, *Nat. Commun.*, 2017, **8**, 14621.
228 R. Juneja and A. K. Singh, *J. Mater. Chem. A*, 2020, **8**, 8716–8721.
229 A. Chen, X. Zhang, L. Chen, S. Yao and Z. Zhou, *J. Phys. Chem. C*, 2020, **124**, 22471–22478.
230 Y. Zhu, J. Wang, H. Chu, Y.-C. Chu and H. M. Chen, *ACS Energy Lett.*, 2020, **5**, 1281–1291.
231 J. Li and J. Gong, *Energy Environ. Sci.*, 2020, **13**, 3748–3779.
232 L. Liu, W. Li, X. He, J. Yang and N. Liu, *Small*, 2022, **18**, e2104205.
233 S. Zuo, Z. P. Wu, H. Zhang and X. W. Lou, *Adv. Energy Mater.*, 2022, **12**, 2103383.
234 H. An, L. Wu, L. D. B. Mandemaker, S. Yang, J. de Ruiter, J. H. J. Wijten, J. C. L. Janssens, T. Hartman, W. van der Stam and B. M. Weckhuysen, *Angew. Chem., Int. Ed.*, 2021, **60**, 16576–16584.
235 X. Lu, C. Zhu, Z. Wu, J. Xuan, J. S. Francisco and H. Wang, *J. Am. Chem. Soc.*, 2020, **142**, 15438–15444.
236 H. An, L. Wu, L. D. B. Mandemaker, S. Yang, J. de Ruiter, J. H. J. Wijten, J. C. L. Janssens, T. Hartman, W. van der Stam and B. M. Weckhuysen, *Angew. Chem., Int. Ed.*, 2021, **60**, 16576–16584.
237 P. B. Joshi, N. Karki and A. J. Wilson, *ACS Energy Lett.*, 2022, **7**, 602–609.
238 C. Zhan, F. Dattila, C. Rettenmaier, A. Bergmann, S. Kuhl, R. Garcia-Muelas, N. Lopez and B. R. Cuenya, *ACS Catal.*, 2021, **11**, 7694–7701.
239 M. He, C. Li, H. Zhang, X. Chang, J. G. Chen, W. A. Goddard, 3rd, M. J. Cheng, B. Xu and Q. Lu, *Nat. Commun.*, 2020, **11**, 3844.
240 H. An, L. Wu, L. D. B. Mandemaker, S. Yang, J. de Ruiter, J. H. J. Wijten, J. C. L. Janssens, T. Hartman, W. van der Stam and B. M. Weckhuysen, *Angew. Chem., Int. Ed.*, 2021, **60**, 16576–16584.
241 X. Cao, D. Tan, B. Wulan, K. S. Hui, K. N. Hui and J. Zhang, *Small Methods*, 2021, **5**, e2100700.
242 X. Yuan, S. Chen, D. Cheng, L. Li, W. Zhu, D. Zhong, Z. J. Zhao, J. Li, T. Wang and J. Gong, *Angew. Chem., Int. Ed.*, 2021, **133**, 15472–15475.
243 H. Liu, Z. Qi and L. Song, *J. Phys. Chem. C*, 2021, **125**, 24289–24300.
244 S. Chen, Z. Zhang, W. Jiang, S. Zhang, J. Zhu, L. Wang, H. Ou, S. Zaman, L. Tan, P. Zhu, E. Zhang, P. Jiang, Y. Su, D. Wang and Y. Li, *J. Am. Chem. Soc.*, 2022, **144**, 12807–12815.
245 C. Liu, Y. Wu, J. Fang, K. Yu, H. Li, W. He, W.-C. Cheong, S. Liu, Z. Chen, J. Dong and C. Chen, *Chin. J. Catal.*, 2022, **43**, 1697–1702.
246 B. Wang, S. Chu, L. Zheng, X. Li, J. Zhang and F. Zhang, *Small Sci.*, 2021, **1**, 2100023.
247 Y. Yang, I. Roh, S. Louisia, C. Chen, J. Jin, S. Yu, M. B. Salmeron, C. Wang and P. Yang, *J. Am. Chem. Soc.*, 2022, **144**, 8927–8931.
248 J. Timoshenko and B. Roldan Cuenya, *Chem. Rev.*, 2021, **121**, 882–961.
249 S. C. Lin, C. C. Chang, S. Y. Chiu, H. T. Pai, T. Y. Liao, C. S. Hsu, W. H. Chiang, M. K. Tsai and H. M. Chen, *Nat. Commun.*, 2020, **11**, 3525.
250 N. Kornienko, *Nanoscale*, 2021, **13**, 1507–1514.
251 B. Mei, C. Liu, F. Sun, S. Lu, X. Du, X. Li, F. Song, W. Xu and Z. Jiang, *ACS Catal.*, 2022, **12**, 8676–8686.
252 H. Jung, S. Y. Lee, C. W. Lee, M. K. Cho, D. H. Won, C. Kim, H. S. Oh, B. K. Min and Y. J. Hwang, *J. Am. Chem. Soc.*, 2019, **141**, 4624–4633.
253 H. Mistry, A. S. Varela, C. S. Bonifacio, I. Zegkinoglou, I. Sinev, Y. W. Choi, K. Kisslinger, E. A. Stach, J. C. Yang, P. Strasser and B. R. Cuenya, *Nat. Commun.*, 2016, **7**, 12123.

254 H. Y. Wang, M. Soldemo, D. Degerman, P. Lomker, C. Schlueter, A. Nilsson and P. Amann, *Angew. Chem., Int. Ed.*, 2022, **61**, e202111021.
255 C. Long, J. Han, J. Guo, C. Yang, S. Liu and Z. Tang, *Chem. Catal.*, 2021, **1**, 509–522.
256 R. Arrigo, R. Blume, A. I. Large, J. J. Velasco-Velez, M. Havecker, A. Knop-Gericke and G. Held, *Faraday Discuss.*, 2022, **236**, 126–140.
257 X. Feng, H. Zou, R. Zheng, W. Wei, R. Wang, W. Zou, G. Lim, J. Hong, L. Duan and H. Chen, *Nano Lett.*, 2022, **22**, 1656–1664.
258 Y. Zhu, T.-R. Kuo, Y.-H. Li, M.-Y. Qi, G. Chen, J. Wang, Y.-J. Xu and H. M. Chen, *Energy Environ. Sci.*, 2021, **14**, 1928–1958.
259 K. A. Fichthorn and T. Yan, *J. Phys. Chem. C*, 2021, **125**, 3668–3679.
260 A. F. Beker, H. Sun, M. Lemang, J. T. van Omme, R. G. Spruit, M. Bremmer, S. Basak and H. H. Perez Garza, *Nanoscale*, 2020, **12**, 22192–22201.
261 C. Zhu, S. Liang, E. Song, Y. Zhou, W. Wang, F. Shan, Y. Shi, C. Hao, K. Yin, T. Zhang, J. Liu, H. Zheng and L. Sun, *Nat. Commun.*, 2018, **9**, 421.
262 L. Xiao, G. Wang, X. Huang, S. Zhou, R. Zhou, Y. Jiang, S. Liu, G. Li, H. Zheng, S.-G. Sun and H.-G. Liao, *Appl. Catal., B*, 2022, **307**, 121164.
263 M. C. O. Monteiro, A. Mirabal, L. Jacobse, K. Doblhoff-Dier, S. C. Barton and M. T. M. Koper, *JACS Au*, 2021, **1**, 1915–1924.
264 A. Preet and T.-E. Lin, *Catalysts*, 2021, **11**, 594.
265 C. H. Ryu, Y. Nam and H. S. Ahn, *Chin. J. Catal.*, 2022, **43**, 59–70.
266 Y. Wang, Y. Zou, L. Tao, Y. Wang, G. Huang, S. Du and S. Wang, *Nano Res.*, 2019, **12**, 2055–2066.
267 J. Li, G. Chen, Y. Zhu, Z. Liang, A. Pei, C.-L. Wu, H. Wang, H. R. Lee, K. Liu, S. Chu and Y. Cui, *Natl. Catal.*, 2018, **1**, 592–600.
268 Y. Jiang, X. Zhang, D. Xu, W. Li, M. Liu and X. Qiu, *Chem. Commun.*, 2021, **57**, 6011–6014.
269 S. Li, W. Chen, X. Dong, C. Zhu, A. Chen, Y. Song, G. Li, W. Wei and Y. Sun, *Nat. Commun.*, 2022, **13**, 3080.
270 S. Ringe, E. L. Clark, J. Resasco, A. Walton, B. Seger, A. T. Bell and K. Chan, *Energy Environ. Sci.*, 2019, **12**, 3001–3014.
271 M. C. O. Monteiro, F. Dattila, N. Lopez and M. T. M. Koper, *J. Am. Chem. Soc.*, 2022, **144**, 1589–1602.
272 J. E. Huang, F. Li, A. Ozden, A. Sedighian Rasouli, F. P. Garcia de Arquer, S. Liu, S. Zhang, M. Luo, X. Wang, Y. Lum, Y. Xu, K. Bertens, R. K. Miao, C. T. Dinh, D. Sinton and E. H. Sargent, *Science*, 2021, **372**, 1074–1078.
273 J. Resasco, Y. Lum, E. Clark, J. Z. Zeledon and A. T. Bell, *ChemElectroChem*, 2018, **5**, 1064–1072.
274 S. Jin, Z. Hao, K. Zhang, Z. Yan and J. Chen, *Angew. Chem., Int. Ed.*, 2021, **60**, 20627–20648.
275 X. Wang, K. Klingan, M. Klingenhof, T. Moller, J. Ferreira de Araujo, I. Martens, A. Bagger, S. Jiang, J. Rossmeisl, H. Dau and P. Strasser, *Nat. Commun.*, 2021, **12**, 794.
276 R. Yang, J. Duan, P. Dong, Q. Wen, M. Wu, Y. Liu, Y. Liu, H. Li and T. Zhai, *Angew. Chem., Int. Ed.*, 2022, **61**, e202116706.
277 M. C. O. Monteiro, F. Dattila, B. Hagedoorn, R. García-Muelas, N. López and M. T. M. Koper, *Natl. Catal.*, 2021, **4**, 654–662.
278 R. Yang, J. Duan, P. Dong, Q. Wen, M. Wu, Y. Liu, Y. Liu, H. Li and T. Zhai, *Angew. Chem., Int. Ed.*, 2022, **61**, e202116706.
279 A. Mota-Lima, M. L. Alcantara, F. J. Pérez-Sanz, R. C. Bazito, P. Vidinha, R. M. B. Alves and C. A. Oller Nascimento, *J. Electrochem. Soc.*, 2021, **168**, 086502.
280 G. R. Zhang, S. D. Straub, L. L. Shen, Y. Hermans, P. Schmatz, A. M. Reichert, J. P. Hofmann, I. Katsounaros and B. J. M. Etzold, *Angew. Chem., Int. Ed.*, 2020, **59**, 18095–18102.
281 W. Ren, X. Tan, X. Chen, G. Zhang, K. Zhao, W. Yang, C. Jia, Y. Zhao, S. C. Smith and C. Zhao, *ACS Catal.*, 2020, **10**, 13171–13178.
282 S. Yu and P. K. Jain, *Nat. Commun.*, 2019, **10**, 2022.
283 Y. Sha, J. Zhang, X. Cheng, M. Xu, Z. Su, Y. Wang, J. Hu, B. Han and L. Zheng, *Angew. Chem., Int. Ed.*, 2022, **61**, e202200039.
284 G. Neri, J. J. Walsh, G. Teobaldi, P. M. Donaldson and A. J. Cowan, *Natl. Catal.*, 2018, **1**, 952–959.
285 P. Kamat and P. Christopher, *ACS Energy Lett.*, 2022, **7**, 1469–1472.
286 T. Möller, T. Ngo Thanh, X. Wang, W. Ju, Z. Jovanov and P. Strasser, *Energy Environ. Sci.*, 2021, **14**, 5995–6006.
287 T. Zhang, R. Shi and Y. Ma, *Acta Chim. Sin.*, 2021, **79**, 369.
288 F. P. Garcia de Arquer, C. T. Dinh, A. Ozden, J. Wicks, C. McCallum, A. R. Kirmani, D. H. Nam, C. Gabardo, A. Seifitokaldani, X. Wang, Y. C. Li, F. Li, J. Edwards, L. J. Richter, S. J. Thorpe, D. Sinton and E. H. Sargent, *Science*, 2020, **367**, 661–666.
289 D. Raciti, T. Braun, B. M. Tackett, H. Xu, M. Cruz, B. J. Wiley and T. P. Moffat, *ACS Catal.*, 2021, **11**, 11945–11959.
290 L. Xue, X. Wu, Y. Liu, B. Xu, X. Wang, S. Dai, P. Liu and H. Yang, *Nano Res.*, 2021, **15**, 1393–1398.
291 X. Chen, J. Chen, N. M. Alghoraibi, D. A. Henckel, R. Zhang, U. O. Nwabara, K. E. Madsen, P. J. A. Kenis, S. C. Zimmerman and A. A. Gewirth, *Natl. Catal.*, 2020, **4**, 20–27.
292 Z. Zhang, X. Huang, Z. Chen, J. Zhu, B. Endrődi, C. Janáky and D. Deng, *Angew. Chem., Int. Ed.*, 2023, **135**, e202302789.
293 D. A. Salvatore, C. M. Gabardo, A. Reyes, C. P. O'Brien, S. Holdcroft, P. Pintauro, B. Bahar, M. Hickner, C. Bae, D. Sinton, E. H. Sargent and C. P. Berlinguette, *Nat. Energy*, 2021, **6**, 339–348.
294 N. Sikdar, J. R. C. Junqueira, S. Dieckhofer, T. Quast, M. Braun, Y. Song, H. B. Aiyappa, S. Seisel, J. Weidner, D. Ohl, C. Andronescu and W. Schuhmann, *Angew. Chem., Int. Ed.*, 2021, **60**, 23427–23434.
295 Z. Qiu, Y. Yun, M. He and L. Wang, *Chem. Eng. J.*, 2023, **456**, 140942.
296 A. Prajapati, R. Sartape, M. T. Galante, J. Xie, S. L. Leung, I. Bessa, M. H. S. Andrade, R. T. Somich, M. V. Rebouças,

G. T. Hutras, N. Diniz and M. R. Singh, *Energy Environ. Sci.*, 2022, **15**, 5105–5117.
297 R. B. Kutz, Q. Chen, H. Yang, S. D. Sajjad, Z. Liu and I. R. Masel, *Energy Technol.*, 2017, **5**, 929–936.
298 Z.-Y. Wu, P. Zhu, D. A. Cullen, Y. Hu, Q.-Q. Yan, S.-C. Shen, F.-Y. Chen, H. Yu, M. Shakouri, J. D. Arregui-Mena, A. Ziabari, A. R. Paterson, H.-W. Liang and H. Wang, *Nat. Synth.*, 2022, **1**, 658–667.
299 S. Noh, J. Y. Jeon, S. Adhikari, Y. S. Kim and C. Bae, *Acc. Chem. Res.*, 2019, **52**, 2745–2755.
300 E. J. Park and Y. S. Kim, *J. Mater. Chem. A*, 2018, **6**, 15456–15477.
301 Z. Yin, H. Peng, X. Wei, H. Zhou, J. Gong, M. Huai, L. Xiao, G. Wang, J. Lu and L. Zhuang, *Energy Environ. Sci.*, 2019, **12**, 2455–2462.
302 E. W. Lees, B. A. W. Mowbray, F. G. L. Parlane and C. P. Berlinguette, *Nat. Rev. Mater.*, 2021, **7**, 55–64.
303 F. Li, A. Thevenon, A. Rosas-Hernandez, Z. Wang, Y. Li, C. M. Gabardo, A. Ozden, C. T. Dinh, J. Li, Y. Wang, J. P. Edwards, Y. Xu, C. McCallum, L. Tao, Z. Q. Liang, M. Luo, X. Wang, H. Li, C. P. O'Brien, C. S. Tan, D. H. Nam, R. Quintero-Bermudez, T. T. Zhuang, Y. C. Li, Z. Han, R. D. Britt, D. Sinton, T. Agapie, J. C. Peters and E. H. Sargent, *Nature*, 2020, **577**, 509–513.
304 L. C. Weng, A. T. Bell and A. Z. Weber, *Phys. Chem. Chem. Phys.*, 2018, **20**, 16973–16984.
305 C. M. Gabardo, C. P. O'Brien, J. P. Edwards, C. McCallum, Y. Xu, C.-T. Dinh, J. Li, E. H. Sargent and D. Sinton, *Joule*, 2019, **3**, 2777–2791.
306 M. G. Kibria, C. T. Dinh, A. Seifitokaldani, P. De Luna, T. Burdyny, R. Quintero-Bermudez, M. B. Ross, O. S. Bushuyev, F. P. Garcia de Arquer, P. Yang, D. Sinton and E. H. Sargent, *Adv. Mater.*, 2018, **30**, e1804867.
307 T. T. H. Hoang, S. Verma, S. Ma, T. T. Fister, J. Timoshenko, A. I. Frenkel, P. J. A. Kenis and A. A. Gewirth, *J. Am. Chem. Soc.*, 2018, **140**, 5791–5797.
308 P. De Luna, R. Quintero-Bermudez, C.-T. Dinh, M. B. Ross, O. S. Bushuyev, P. Todorović, T. Regier, S. O. Kelley, P. Yang and E. H. Sargent, *Natl. Catal.*, 2018, **1**, 103–110.
309 K. Jiang, P. Kharel, Y. Peng, M. K. Gangishetty, H.-Y. G. Lin, E. Stavitski, K. Attenkofer and H. Wang, *ACS Sustainable Chem. Eng.*, 2017, **5**, 8529–8534.
310 Y. Wang, Y. Chen, Y. Zhao, J. Yu, Z. Liu, Y. Shi, H. Liu, X. Li and W. Zhou, *Appl. Catal., B*, 2022, **307**, 120991.
311 R. Shi, J. Guo, X. Zhang, G. I. N. Waterhouse, Z. Han, Y. Zhao, L. Shang, C. Zhou, L. Jiang and T. Zhang, *Nat. Commun.*, 2020, **11**, 3028.
312 N. Gutiérrez-Guerra, L. Moreno-López, J. C. Serrano-Ruiz, J. L. Valverde and A. de Lucas-Consuegra, *Appl. Catal., B*, 2016, **188**, 272–282.
313 S. Verma, X. Lu, S. Ma, R. I. Masel and P. J. Kenis, *Phys. Chem.*, 2016, **18**, 7075–7084.
314 Z.-Z. Niu, L.-P. Chi, R. Liu, Z. Chen and M.-R. Gao, *Energy Environ. Sci.*, 2021, **14**, 4169–4176.
315 M. Jouny, W. Luc and F. Jiao, *Ind. Eng. Chem. Res.*, 2018, **57**, 2165–2177.
316 M. Li, M. N. Idros, Y. Wu, T. Burdyny, S. Garg, X. S. Zhao, G. Wang and T. E. Rufford, *J. Mater. Chem. A*, 2021, **9**, 19369–19409.
317 H. Rabiee, L. Ge, X. Zhang, S. Hu, M. Li, S. Smart, Z. Zhu, H. Wang and Z. Yuan, *Appl. Catal., B*, 2021, **298**, 121362.
318 S. Alinejad, J. Quinson, G. K. H. Wiberg, N. Schlegel, D. Zhang, Y. Li, S. Reichenberger, S. Barcikowski and M. Arenz, *ChemElectroChem*, 2022, **9**, e202200341.
319 M. C. O. Monteiro, S. Dieckhofer, T. Bobrowski, T. Quast, D. Pavesi, M. T. M. Koper and W. Schuhmann, *Chem. Sci.*, 2021, **12**, 15682–15690.
320 Y. Kong, H. Hu, M. Liu, Y. Hou, V. Kolivoška, S. Vesztergom and P. Broekmann, *J. Catal.*, 2022, **408**, 1–8.
321 J.-B. Vennekoetter, R. Sengpiel and M. Wessling, *Chem. Engin. J.*, 2019, **364**, 89–101.
322 B. Kim, F. Hillman, M. Ariyoshi, S. Fujikawa and P. J. A. Kenis, *J. Power Sources*, 2016, **312**, 192–198.
323 G. Park, S. Hong, M. Choi, S. Lee and J. Lee, *Catal. Today*, 2020, **355**, 340–346.
324 D. M. Weekes, D. A. Salvatore, A. Reyes, A. Huang and C. P. Berlinguette, *Acc. Chem. Res.*, 2018, **51**, 910–918.
325 D. H. Nam, O. Shekhah, A. Ozden, C. McCallum, F. Li, X. Wang, Y. Lum, T. Lee, J. Li, J. Wicks, A. Johnston, D. Sinton, M. Eddaoudi and E. H. Sargent, *Adv. Mater.*, 2022, **34**, e2207088.
326 W. Liu, P. Zhai, A. Li, B. Wei, K. Si, Y. Wei, X. Wang, G. Zhu, Q. Chen, X. Gu, R. Zhang, W. Zhou and Y. Gong, *Nat. Commun.*, 2022, **13**, 1877.
327 G. Wang, J. Pan, S. P. Jiang and H. Yang, *J. CO2 Util.*, 2018, **23**, 152–158.
328 B. Endrodi, E. Kecsenovity, A. Samu, F. Darvas, R. V. Jones, V. Torok, A. Danyi and C. Janaky, *ACS Energy Lett.*, 2019, **4**, 1770–1777.
329 K. Jiang, S. Siahrostami, T. Zheng, Y. Hu, S. Hwang, E. Stavitski, Y. Peng, J. Dynes, M. Gangisetty, D. Su, K. Attenkofer and H. Wang, *Energy Environ. Sci.*, 2018, **11**, 893–903.
330 S. Ren, D. Joulie, D. Salvatore, K. Torbensen, M. Wang, M. Robert and C. P. Berlinguette, *Science*, 2019, **365**, 367–369.
331 J. Zou, C.-Y. Lee and G. G. Wallace, *ACS Sustainable Chem. Eng.*, 2021, **9**, 16394–16402.
332 Y. Xu, R. K. Miao, J. P. Edwards, S. Liu, C. P. O'Brien, C. M. Gabardo, M. Fan, J. E. Huang, A. Robb, E. H. Sargent and D. Sinton, *Joule*, 2022, **6**, 1333–1343.
333 M. Esmaeilirad, A. Baskin, A. Kondori, A. Sanz-Matias, J. Qian, B. Song, M. Tamadoni Saray, K. Kucuk, A. R. Belmonte, P. N. M. Delgado, J. Park, R. Azari, C. U. Segre, R. Shahbazian-Yassar, D. Prendergast and M. Asadi, *Nat. Commun.*, 2021, **12**, 5067.
334 J. Y. T. Kim, P. Zhu, F.-Y. Chen, Z.-Y. Wu, D. A. Cullen and H. Wang, *Natl. Catal.*, 2022, **5**, 288–299.
335 A. N. Biswas, Z. Xie, R. Xia, S. Overa, F. Jiao and J. G. Chen, *ACS Energy Lett.*, 2022, **7**, 2904–2910.
336 U. Savino and A. Sacco, *J. CO2 Util.*, 2021, **52**, 101697.

337 J. Gu, S. Liu, W. Ni, W. Ren, S. Haussener and X. Hu, *Natl. Catal.*, 2022, **5**, 268–276.
338 B. Pan, J. Fan, J. Zhang, Y. Luo, C. Shen, C. Wang, Y. Wang and Y. Li, *ACS Energy Lett.*, 2022, **7**, 4224–4231.
339 C. Yang, Z. Gao, D. Wang, S. Li, J. Li, Y. Zhu, H. Wang, W. Yang, X. J. Gao, Z. Zhang and W. Hu, *Sci. China Mater.*, 2021, **65**, 155–162.
340 X. Pang, S. Verma, C. Liu and D. V. Esposito, *Joule*, 2022, **6**, 2745–2761.
341 S. Jin, Z. Hao, K. Zhang, Z. Yan and J. Chen, *Angew. Chem., Int. Ed.*, 2021, **60**, 20627–20648.
342 N. Ikemiya, K. Natsui, K. Nakata and Y. Einaga, *ACS Sustainable Chem. Eng.*, 2018, **6**, 8108–8112.
343 Irkham, S. Nagashima, M. Tomisaki and Y. Einaga, *ACS Sustainable Chem. Eng.*, 2021, **9**, 5298–5303.
344 S. Verma, Y. Hamasaki, C. Kim, W. Huang, S. Lu, H.-R. M. Jhong, A. A. Gewirth, T. Fujigaya, N. Nakashima and P. J. A. Kenis, *ACS Energy Lett.*, 2017, **3**, 193–198.
345 H. Yang, J. J. Kaczur, S. D. Sajjad and R. I. Masel, *J. CO2 Util.*, 2017, **20**, 208–217.
346 M. Zhang, W. Wei, S. Zhou, D.-D. Ma, A. Cao, X.-T. Wu and Q.-L. Zhu, *Energy Environ. Sci.*, 2021, **14**, 4998–5008.
347 S. G. Han, M. Zhang, Z. H. Fu, L. Zheng, D. D. Ma, X. T. Wu and Q. L. Zhu, *Adv. Mater.*, 2022, **33**, e2202830.
348 H. Yang, Q. Lin, C. Zhang, X. Yu, Z. Cheng, G. Li, Q. Hu, X. Ren, Q. Zhang, J. Liu and C. He, *Nat. Commun.*, 2020, **11**, 593.
349 W. Liu, S. Wei, P. Bai, C. Yang and L. Xu, *Appl. Catal., B*, 2021, **299**, 120661.

